DYNAMICS OF CIRCULATION-CONTROLLED FIREWHIRLS AND PERIODICALLY-FORCED JETS

YU DEHAI

Ph.D

The Hong Kong Polytechnic University

2018

The Hong Kong Polytechnic University

Department of Mechanical Engineering

DYNAMICS OF CIRCULATION-CONTROLLED FIREWHIRLS AND PERIODICALLY-FORCED JETS

YU DEHAI

A thesis submitted in partial fulfillment of the requirement for the degree of Doctor of Philosophy

August 2017

CERTIFICATE OF ORIGINALITY

I hereby declare that this thesis is my own work and that, to the best of my knowledge and belief, it reproduces no material previously published or written, nor material that has been accepted for the award of any other degree of diploma, except where due acknowledgement has been made in the text.

_____(Signed)

YU DEHAI (Name of student)

Abstract

This thesis consists of two parts, viz. the circulation-controlled firewhirls for the first part and periodically-forced jet for the second part. The first part of this thesis progressively presents our theoretical studies on circulation-controlled firewhirls. The circulation-controlled firewhirls was reproduced by Chuah et al. in laboratory (*Proc. Combust. Inst.* **33**, 2011). The theory proposed by Chuah et al. yielded an underestimation to the flame height due to the oversimplified assumptions, e.g., constant physical properties (density and mass diffusivity), Burgers vortex, and unity Lewis number. The revised theory by Klimenko and Williams (*Combust. Flame* **160**, 2013) in which the Burges vortex was replaced by strong vortex interpreted well with the Chuah et al.'s experimental observed flame heights. Through a series of theoretical studies, we proposed a generalized flame height theory in which the effect of variable physical properties was taken into account by introducing the Howarth-Dorodnitsyn-like coordinate transformations, converting the formulation into "density-implicit" form, the effect of differential diffusion was considered by constructing a mass-diffusivity-ratio-model correction, which is verified by the non-unity Lewis number asymptotic analysis, and moreover the strong vortex model proposed by Klimenko was appropriately implemented in our generalized flame height theory by generalizing its mathematical form. Our generalized flame height formula agrees well with the Chuah

et al.'s experiments, and in the meanwhile provides further understandings in non-premixed flames of fundamental combustion problems.

In second part of the thesis, the response of compressible axisymmetric jets to external periodic forcing at the jet exit was analyzed based on the energy integral method with emphasis on identifying the optimal forcing frequency that can maximize the spreading of the shear layer surrounding the jet potential core. The non-monotonic variation of optimal forcing frequency with respect to the jet Mach numbers is investigated systematically. The results show that the identified optimal Strouhal number, St_p, decreases first with increasing M_0 due to stronger suppression of the flow compressibility on the growth of high-frequency perturbations than that of low-frequency ones. As M_0 increases to above a critical value, the suppression is of approximately the same extent to all the frequencies, and thus St_p starts to increase because the jet development favors high-frequency perturbations, which have higher rates of energy transfer from the base jet flow and hence larger growth rates. With further increasing M_0, St_p decreases again mainly because the viscous dissipation suppresses the development of high-frequency forced perturbation more significantly than that of low-frequency ones.

Publications

Journals

1. Dehai Yu and Peng Zhang*, On the flame height of circulation-controlled firewhirls with variable density. *Proceedings of the Combustion Institute*, 36, (2017). 3097-3104.

2. Dehai Yu and Peng Zhang*, On flame height of circulation-controlled firewhirls with variable physical properties and in power-law vortices: A mass-diffusivity-ratio model correction. *Combustion and Flame*, (2017). 182, 36-47.

3. Dehai Yu and Peng Zhang*, Circulation-controlled firewhirls with differential diffusion, Combustion and Flame 189 (2018) 288-299

4. Dehai Yu, Hongbin Gu and Peng Zhang*, An energy integral analysis of compressible axisymmetric jets with external periodic forcing, *International Journal of Heat and Fluid Flow* (under revision)

5. Xi Xia, Chenming He, Dehai Yu, Jiaquan Zhao, and Peng Zhang*, Vortex-Ring-Induced Internal Mixing Upon the Coalescence of Initially Stationary Droplets, Physical Review Fluids 2, 113607 (2017)

6. Dawei Zhang, Dehai Yu, Yueming Yuan, Lianjie Yue, Peng Zhang*, Taichang Zhang and Xuejun Fan, Hypergolic ignition by bead-on collision of TMEDA and

WFNA droplets: size effects on multiple time scales, *Proceedings of the Combustion Institute*, 37, (under review).

Conferences

1. Dehai Yu, Hongbin Gu and Peng Zhang*, An energy integral method analysis of preferred modes and the spreading rates of supersonic circular jets. The 10th Asia-Pacific Conference on Combustion, 2015, Beijing.

2. Dehai Yu and Peng Zhang*, On the flame height of circulation-controlled firewhirls with variable density. The 36th International Symposium on Combustion, 2016, Seoul.

3. Dehai Yu and Peng Zhang*, A unified theory on flame height of circulation-controlled firewhirls in power-law vortices and with variable physical properties. The 8th European Combustion Meeting, Dubrovnik.

4. Dehai Yu and Peng Zhang*, Lewis number effect on the flame height of circulation-controlled firewhirls. The 11th Asia-Pacific Conference on Combustion, 2017, Sydney.

5. 于德海，张鹏*，刘易斯数对旋流主导火旋风高度的影响，中国工程热物理学会，2017，南京。

Acknowledgement

The author would like to express his deepest gratitude and highest respect to his chief supervisor, Prof. Peng Zhang, not only for the interesting and carefully selected research topics, but more importantly, for his rigorous attitude and strict requirements to academic research, which has encouraged the author's confidence and led him on the right track of research. His great mentorship and guidance will be profoundly influence the author in both academic career and life.

The author is grateful to Prof. Chih-Yung Wen and Prof. Chun-Wah Leung for their encouragements and constructive suggestions to the author's research.

The author also would like to express thanks to the external examiners in the Board of Examination, Prof. Zhigang Li and Prof. Zheng Chen for their insightful comments to this thesis, which have been carefully addressed in the revision.

A special acknowledgement to all the students and staff in Prof. Zhang's Fundamental Combustion Research Laboratory, who created a perfect environment for intellectual development and personal life.

Table of Contents

Overview

Dawn of civilization commenced when human acquired the ability to use fire. With the very source of energy from the Nature, the human can reshape the world, such as building cities, developing industries, and improving transportations. During the past a few decades, the population undergoes rapid increasing, resulting in an explosive trend in the energy consumption. Although in this age various alternative forms of energy supply become available, such as nuclear power, solar energy, and geothermal energy. The vast majority of the overall energy consumption of the whole world, stably around 85 percent, is supplied by the combustion of fossil fuel, such as coal, oil, and natural gas[40]. Therefore, in the foreseeable future, combustion will still be the most dominant approach that man can drive energy from the earth because of its convenience, high-energy density, and the economics.

Combustion is defined as a highly exothermic chemical reaction between a fuel, e.g. hydrocarbons, and an oxidant, e.g. oxygen in air. Besides releasing heat, the combustion also produces oxidized products. In complete combustion the fuel, e.g., hydrocarbon, is completely burnt, producing a limit number of products, such as carbon dioxide CO_2 and water H_2O. For incomplete combustion, the oxygen in the air is utterly consumed, giving however a very complex arranges of products, which could either be carbon monoxide CO or the hydrocarbons with longer chain and more

complex structure, or even the carbon particles, i.e., soot, formed through extremely complicated physical and chemical paths. In general, the energy from combustion is used to generate heat and power, such as, domestic heating, firing of industrial furnace, and the operation of automotive engines. Various theoretical, experimental and numerical researches have been conducted on combustion to optimize its performance in thermal engineering devices. For example, the transport vehicles, which is a major consumer of petroleum fuels and contributor of air pollution, two aspects should be considered in its design, the first is efficient energy utilization, i.e. providing more power by consuming unit mass of fuel in combustion, to acquire longer cursing distance, the second is clean combustion, i.e., preventing the hazardous products, such as carbon monoxide, NOx, and soot from releasing to the atmosphere, to meet the requirements for environmental protection.

The rapidly increasing energy consumption urges to high efficiency of fuel combustion, while the environment protection and public safety demands the combustion to be both clean and precisely controllable. Both factors facilitate the research of combustion as a branch of science. The richness of combustion roots in its very definition, which involves coupling of multi-physics, comprising thermodynamics that determines the heat release amount and its conversion to mechanical power, chemical kinetics that describes the combustion reaction rate considering fundamental chemical and physical processes within, fluid mechanics that specifies the environment

flow supporting combustion reaction within as well as the feedback of the latter to the former, and transport phenomena that deals with the transport of reactive species to feed the combustion reaction as well as the heat to be utilized.

In the study of the phenomena of combustion, the flame is the most important concept, which is defined as a visible, gaseous part of a fire, resulting from a highly exothermic reaction and occurring in a very thin zone. The activation energies of conventional fuels are very high, implying that the chemical reactions are very sensitive to temperature, i.e., the reaction is expected to be activated only when the temperature of reactants is close to its maximum value, and a tender decrease of temperature may cause the reaction to shut down. Therefore, the combustion can only be sustained within a very thin zone. According to theoretical combustion study, the thin flame also consists of two types of sub-zones, namely the diffusion zone and the reaction zone. In specific, the fuel and oxidizer are diffusively transported through the diffusion zone to feed the chemical reaction in the reaction zone, while being heated to higher temperature by the heat conducted from there, where in the chemical reaction generates heat and burnt products to be transported to both sides of the flame.

In phenomenology, flames can be classified in two categories, namely, premixed and non-premixed flames, depending on how the fuel and oxidizer are prepared in the combustion system. In a global view, a combustion system comprises two reactants, i.e., fuel and oxidizer, which must be brought together and mixed, precisely speaking

at the molecular level, before reaction can take place. It indicates that the mixing mechanisms are the essential elements in influencing the characteristics of combustion. In other words, the behavior of the combustion systems can be quite different depending on initial preparation of the fuel and oxidizer, i.e. whether being mixed or being separate in distinct spatial locations.

In premixed combustion where the fuel and oxidizer are well mixed before reaction taking place, the flame can inherently be regarded as a wave propagating in space, constituted by the fuel-oxidizer mixture, with specified moving velocity, i.e. the premixed flame speed, characterizing the consumption rate of the fuel-oxidizer mixture, thus the overall combustion reaction rate. More importantly, the premixed flame speed can be measured via techniques of fluid dynamics, thus provides reference and significant convenience for engineering design. The premixed flame speed thus defined depends upon various physical and chemical properties of the combustion. e.g. the flow characteristics, the chemical structures of fuels, and transport properties of the combustion systems. In specific, the premixed flame speeds in turbulent flows are much larger than those in laminar flows; the fuels with small molecular weight and compact structures have higher premixed flame speeds than the long chain hydrocarbons, and the premixed flame speeds of the same fuel-oxidizer mixture diluted in various inert gases should be different from each other.

In non-premixed combustion, the reactants are initially separated, and are transported towards each other through molecular process of diffusion and the bulk convective motion, to a specific region, i.e. the non-premixed flame, where the mixing and subsequently chemical reactions take place. The diffusive transport is the essential element in effecting the mixing of the fuel and oxidizer at the molecular level in non-premixed combustion, and to emphasize the importance of the diffusive transport mechanism that brings fuel and oxidizer together for combustion, the non-premixed flame is also known for "diffusion flame". However, it should be noted that in premixed combustion, the diffusion is still required to transport the fuel-oxidizer mixture to, and the heat release as well as the burnt product away from the reaction zone within the flame[40].

Unlike the premixed flame, the non-premixed flame tends to be anchored in space instead of moving with specific velocity. In general, the flame location is determined by the condition that the local equivalence ratio is unity, i.e. both fuel and oxidizer are completely consumed because if fuel (or oxidizer) was in surplus in the flame location, implying that the fuel (oxidizer) has additional potential to be diffusively transported to further distance, where the diffusive flux of oxidizer (fuel) becomes sufficiently high due to the increasing of gradient, to satisfy the requirement of unity equivalence ratio. Therefore, the non-premixed flame can adjust itself to the new stable location.

There are seldom examples of premixed combustion naturally occurring in the world because if the reactants are premixed, then they would have already reacted no matter how slight the reaction rate is. On the other hand, either by nature or engineering design, in most combustion systems fuel and oxidizer are initially separated in space, thus the combustion taking place there is of non-premixed type. The author of this thesis is particularly interest to two examples of non-premixed flames, namely the firewhirls and jet flame, which will be briefly described as follows.

Figure 0.1 A firewhirl taking place in the wildland. (cited from Wikipedia at the link: *https://en.wikipedia.org/wiki/Fire_whirl*)

The firewhirls are defined as spinning non-premixed flames that often occur in wild and urban fires and have potential to cause severe destruction and great suffering of human[13, 36], as shown in Figure 0.1. In the Great Kanto Earthquake of Japan in 1923, a firewhirl emerged shortly after the earthquake taking place, igniting a large city-size firestorm later. The resulting gigantic firewhirl took 38000 lives within just fifteen minutes in the Hifukusho-Ato region of Tokyo. Another example is the numerous large firewhirls developed after lightning struck an oil storage facility located in California in April, 1926. The firewhirls produced significant damage to the structures both nearby and located well away. Within the four-day-long firestorm, many whirlwinds were generated, which is coincident with the conditions that produced several thunderstorms, where the large firewhirls carried debris several kilometers away.

In experimental study, the firewhirl can be simulated by swirling pool flame, as is shown in the schematic of firewhirl in Figure 0.2. Due to the presence of circulation, the characteristics of pool flame vary significantly, resulting in enhancement of combustion intensity, elongation of flame height, and even transformation to blue firewhirl, which was discovered in very recent study[71]. Therefore, from the aspect of combustion science, the research of firewhirl would not only reduce the damage of firewhirl occurred in the nature, but also provide an effective approach in combustion performance control, which would be of great practicability in the design of combustion devices with swirling flow.

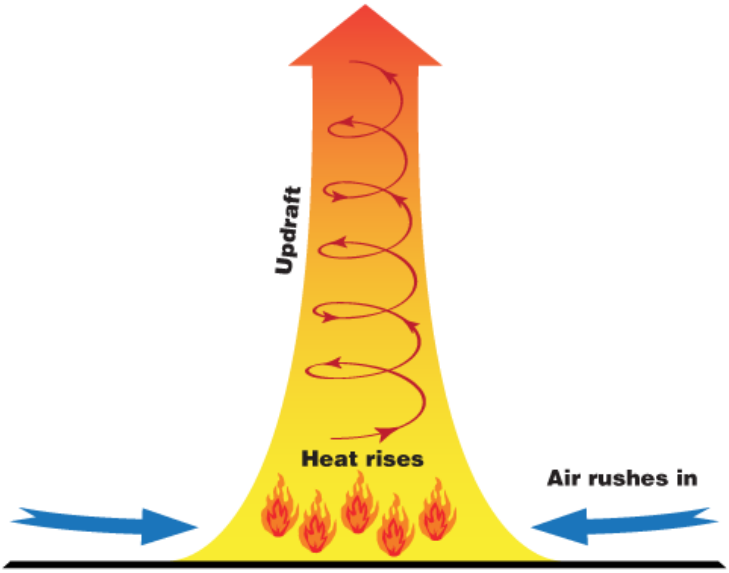

Figure 0.2 The schematic of a firewhirl (cited from SciJinks, a joint NOAA and NASA educational website, at the link: *https://scijinks.gov/firestorm/*)

Jet flame exists in many combustion devices, particularly the propulsion system, where the fuel is injected into the oxidizing environment in the form of a jet. As the fuel jet penetrates into the ambience, it entrains and in the meanwhile mixes with the surrounding fluids. Upon ignition, a non-premixed flame is established and also stabilized at a distance downstream from the nozzle exit. For civilian flight with the cruising speed being subsonic, turbofan engine is utilized to provide thrust, in which the fuel jet has sufficiently time to be mixed with the ambient compressed air in molecular level before combustion can take place, thus the combustion can be very robust to the variation of the environmental conditions. Whereas the situation is completely different for hypersonic airbreathing propulsion system, i.e. the supersonic combustion ramjet (scramjet)[2, 7, 18, 25], in which the combustion is designed to

proceed in the environment of supersonic flow as shown in the schematic of scramjet in Figure 0.3.

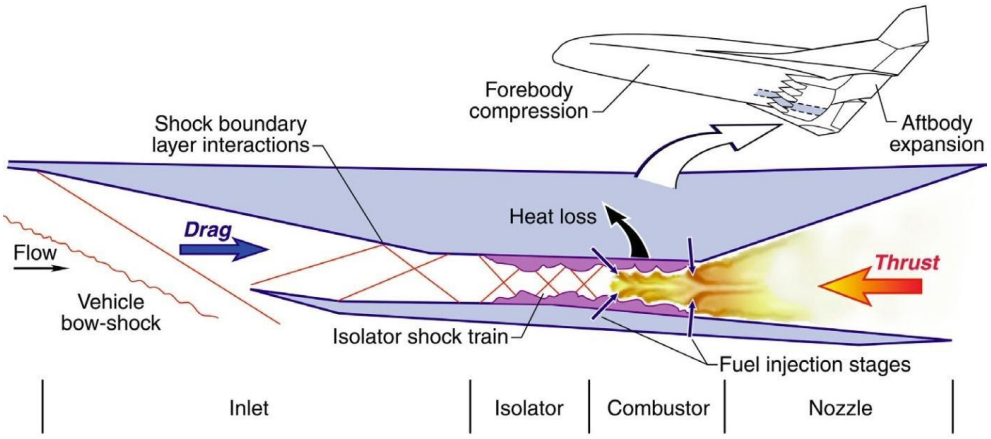

Figure 0.3 Schematic of the working mechanism of scramjet engine

(cited from NASA website at the link

https://www.nasa.gov/centers/langley/news/factsheets/X43A_2006_5.html)

A scramjet is composed of four components[18]: a converging inlet, in the front edge of which an inclined shock wave is formed to compress the incoming air, which is decelerated as moving inside, a combustion chamber where gaseous fuel is burned with atmospheric oxygen to produce heat, resulting in pressure increasing, an isolator sandwiched between the inlet and the combustion chamber to prevent the high pressure propagating upstream to detach the inlet shock wave thus shutting down the whole working process, a diverging nozzle, where the heated air is accelerated to produce the thrust. The rapidity of the flow in the combustion chamber brings about significant challenges in the mixing and chemical reaction processes. Since the combustion

performance depends vitally upon on the quality of mixing, therefore, various mixing enhancement mechanisms and relating methods have been developed to reduce the mixing time and thus shorten the fuel jet distance where the molecular mixing is achieved. One example of mixing enhancement technique is to implement periodic forcing to the fuel jet at the exit, thereby activating the intrinsic instability modes of the jet flow. The generated instability waves could evolve and amplify as the jet flow moving downstream, which facilitates the spreading of the jet shear layer, and thereby enhances the entrainment of ambient fluid into the jet flow. The entanglement of fuel and oxidize fluid forms large vortical structures in the jet shear layer, the breaking of which, as approaching to some critical size, could lead to the mixing of fuel and oxidizer in very small scales.

Noting the great potential in the research of firewhirls, recognizing the importance of mixing enhancement in supersonic combustion and more importantly, being inspired by the physical richness and mathematical beauty of combustion science, the author of this thesis conducted a series of theoretical studies on two aspects. The first is on the circulation-controlled firewhirls, considering the effects of variable physical properties, distinct transport properties and non-unity Lewis numbers, with focus on the variation of flame height, which is a crucial parameter in firewhirls that holds potential to leads to the spread of spot fires in distance. The second is on spreading behavior of periodically-excited jet flow, concerning the variation of optimal forcing frequency,

which corresponds to the maximum spreading of shear layer within the potential core, with respect to the various flow Mach numbers, as well as the changes of the optimal frequency-Mach number curve under the variation of other flow parameters, e.g., flow Reynolds number and the initial forcing amplitudes.

The author has experienced great satisfaction and joy from developing those theoretical studies on both circulation-controlled firewhirls and periodic-forced jet, and he also believes that the results he obtained can provide new insights in the physics of both problems, and in the meanwhile be regarded as useful reference for the more profound research work in the future.

Part I Circulation-Controlled Firewhirls

Nomenclature

Physical quantities

(English letters in alphabetical sequence)

a	=	strain rate of Burgers vortex
c	=	correction function in matching solutions of coupling function
c_p	=	constant pressure specific heat
$d_0(r_0)$	=	diameter (radius) of fuel pool
D	=	mass diffusivity
p	=	pressure
q_c	=	heat of combustion per unit mass of fuel
q_v	=	latent heat of vaporization per unit mass of fuel
r, x, θ	=	cylindrical coordinates
r_c	=	vortex core radius in physical coordinate
T	=	temperature
T_f	=	flame temperature
T_m	=	representative temperature
T_w	=	ground temperature profile

u, v, w = velocity components in x, r, θ directions

$\hat{u}, \hat{v}$ = velocity component in $\xi - \eta$ coordinate

W = molar weight

x_h = flame height location

x_f, r_f = flame contour location

X = molar fraction

Y = mass fraction

Z = mixture fraction

Z_{st} = stoichiometric mixture fraction

(Greek letters in alphabetical sequence)

α_D = ratio of fuel mass diffusivity to oxidizer mass diffusivity,

$$\alpha_D = D_F / D_O$$

α_T = parameter characterizing temperature-dependence mass diffusivity

α_{v1} = exponent in power-law vortex model (inside vortex core)

α_{v2} = exponent in power-law vortex model (outside vortex core)

α_v = overall exponent in power-law vortex model

α_Z = parametric coefficient in the equation for mixture fraction with non-

unity Lewis numbers

Γ = circulation of Burgers vortex

δ_{FN} = average collision diameter

$$\delta_{FN} = (\delta_F + \delta_N)/2$$

δ_{ON} = average collision diameter

$$\delta_{ON} = (\delta_O + \delta_N)/2$$

η_c = the vortex radius in $\xi - \eta$ space

κ = heat loss coefficient

λ = thermal conductivity

ν = kinematic viscosity

ρ = density

σ_{FO} = ratio of molar weights

$$\sigma_{FO} = \nu'_O W_O/(W_F \nu'_F)$$

χ_h = flame height location in $\chi - \zeta$ coordinate

Ω = angular velocity

Ω_{FN} = collision integral between fuel and nitrogen molecules

Average quantities at $x = 0$

$$Q_0 = \frac{1}{r_0}\int_0^{r_0} Q(0,r)dr\,, \qquad Q = (p, T, u, Y_F, \rho)$$

Non-dimensional numbers

Le = Lewis number (in Chapter II)

$$Le = \frac{\lambda}{\rho c_p D}$$

Le_F = fuel Lewis number (in Chapter III and IV)

$$Le_F = \frac{\lambda}{\rho c_p D_F}$$

Le_O = oxidizer Lewis number (in Chapter III and IV)

$$Le_O = \frac{\lambda}{\rho c_p D_O}$$

Pe = Peclet number (in Chapter II)

$$Pe = \frac{u_0 d_0}{D_0}$$

Pe = Peclet number (in Chapter III and IV)

$$Pe = \frac{u_0 d_0}{D_{F0}}$$

Non-dimensional parameters and normalized variables

(English letters in alphabetical sequence)

$\tilde{a}$ = $\tilde{a} = ar_0^2/\nu_0$

A = integral factor in far-field solution of coupling functions

$\widetilde{D}$ = D/D_0

$\tilde{p}$ = p/p_0

$(\tilde{r}, \tilde{x})$ = $(r, x)/r_0$

$\tilde{T}$ = $\tilde{T} = c_p T/q_c$

$(\tilde{u}, \tilde{v})$ = $(u, v)/u_0$

$\tilde{Y}_F$ = Y_F

$\tilde{Y}_O$ = $\tilde{Y}_O = Y_O/\sigma_{FO}$

(Greek letters in alphabetical sequence)

$\tilde{\Gamma}$ = $\tilde{\Gamma} = \Gamma/u_0 r_0$

$\tilde{\rho}$ = ρ/ρ_0

Transformed coordinates

ξ, η = density-mass diffusivity-weighted coordinates

χ, ζ = stream function coordinates

Subscripts

F = quantities on the fuel side

N	=	quantities for inert gas
O	=	quantities on the oxidizer side
0	=	quantities at $x = 0$
∞	=	quantities in far field

Chapter I Introduction

Firewhirls are spinning non-premixed flames that often occur in wild and urban fires and may cause severe destructions. A number of experimental and theoretical studies have been conducted to understand the occurrence and characteristics of firewhirls[5, 6, 11-13, 20, 24, 27, 34-39, 41-43, 61, 70, 79]. Flame length or flame height is an important parameter for characterizing a firewhirl[11-13, 35, 36, 39, 67], as the increasing rotational velocity and entrainment of ambient air result in an appreciable lengthening of the flame due to the conservation of angular momentum[5, 6, 13, 35]. Moreover, the increase of flame length may also enhance the radiant energy flux transmitted to the ambience which in turn leads to the spread of spot fires in distance[5, 6, 13, 35].

It was commonly believed that the flame length of a firewhirl is mainly controlled by the buoyancy effect, which can be characterized by Froude number (Fr) measuring the relative importance of the inertial force compared with the gravitational force. An upwardly convective flow will be induced by the buoyancy when a substantial density variation is caused by the large heat release from the firewhirl [5, 6, 11, 12, 20, 39, 70]. Since a firewhirl must involve a rotating fluid motion, its characterization often needs another non-dimensional parameter, the Rossby number (Ro), to measure the ratio of the inertial force to the Coriolis force.

Compared with a large number of experimental investigations reported in the literature, the theoretical analysis of firewhirls has not been attempted sufficiently. By assuming firewhirl as an inviscid and incompressible flow with buoyancy, Battaglia et al.[6] obtained the numerical solutions of velocity components near the axis for Ro>0.5. It is noted that a "non-Boussinesq" model was proposed in their study to account for the large density variation through a density-scaled velocity transformation, which was introduced by Yih [73] for incompressible stratified flows. Recently, Kuwana et al.[36] experimentally observed that the presence of a weak circulation in buoyancy-controlled firewhirls can have a considerable influence on the flame height by enhancing the burning rate. By introducing a modified "Top-hat" approximation for the axial velocity distribution near the axis, they obtained a linear relation between the dimensionless flame height and the Peclet number, which is the ratio of the flow velocity at the vaporizing liquid surface to the characteristic gaseous diffusion velocity.

In the recent study of Chuah *et al*.[13] on inclined firewhirls, the flame heights were found to be independent of the inclination angles and the burning rates. This observation implies that these firewhirls were controlled by flow circulation instead of buoyance, which would otherwise turn the firewhirls to the vertical direction. The physical explanation to the phenomena is that the inclined firewhirls remain to be inclined rather than turning vertical when sufficiently strong circulation was imposed onto the firewhirl. The strong vortex in the firewhirl stretches the flame along its axis

of rotation and preserves its direction under the constraint of the conservation of angular momentum.

To interpret the experimental observation, Chuah *et al.* [13] proposed a theory for the circulation-controlled firewhirls by means of mixture fraction formulation, in which the following assumptions were adopted, namely

(A-1) The Peclet number is a large quantity, i.e., $Pe \gg 1$.

(A-2) The physical properties, e.g., density and mass diffusivities of fuel and oxidizer, are constants.

(A-3) The vortical flow is modelled by a Burgers vortex.

(A-4) The Lewis number is unity in the whole field of the firewhirl system.

A dimensionless formula for the flame height was thereby derived as

$$\frac{x_h}{d_0} = \frac{Pe}{16Z_{st}} \tag{1.1}$$

Although the theory predicts the right trend that the scaled flame height, x_h/d_0, changes linearly with the stoichiometric-mixture-fraction-scaled Peclet number, $Pe/(16Z_{st})$, it significantly underestimates the flame heights in the presence of strong vortical flows [35].

Klimenko and Williams [35] revisited Chuah *et al.*'s firewhirl theory by using a similar mixture fraction formulation but replacing the Burgers vortex model by a strong

vortex model, because the Burgers vortex was found to be insufficiently strong to describe the realistic vortices, such as tornadoes, hurricanes [34] and firewhirls [9]. A revised formula for flame height, retaining the linear relation of Equation (1.1), contains an additional multiplicative factor, $2/\alpha_v$, as follows

$$\frac{x_h}{d_0} = \frac{2}{\alpha_v}\frac{Pe}{16Z_{st}} \tag{1.2}$$

This factor originates from the power-law model of strong vortices, in which the stream function is given by

$$\psi(r,x) = s(x)r^{\alpha_v} \tag{1.3}$$

and the velocity components are

$$u(r,x) = \frac{1}{r}\frac{\partial\psi}{\partial r} = \alpha_v s(x) r^{\alpha_v - 2} \tag{1.4a}$$

$$v(r,x) = -\frac{1}{r}\frac{\partial\psi}{\partial x} = -s'(x) r^{\alpha_v - 1} \tag{1.4b}$$

Here $s'(x)$ denotes the first-order derivative of $s(x)$. By setting $\alpha_v = 2$, Equation (1.2) can degenerate to Equation (1.1) because Equations (1.3) and (1.4) degenerate to the stream function and velocity components of the Burgers vortex, respectively. However, the exponent α_v must fall below 2 in realistic strong vortices.

Figure 1.1 shows the radial profiles of the scaled axial velocity, $u(x,r)/s(x)$, and the scaled radial velocity, $-v(x,r)/s'(x)$. It is seen that the magnitudes of the axial and radial velocities of strong vortices (i.e. those with $\alpha_v < 2$) are enhanced

significantly in the vicinity of axis, compared with those of Burgers vortex. Moreover, the enhancement of strong vortex increases with decreasing α_v, which varies between 4/3 and 3/2 according to Klimenko's studies [34, 35]. Consequently, Equation (1.2), with either $\alpha_v = 4/3$ or recommended $\alpha_v = 1.43$, predicts considerable enhancement of flame heights of firewhirls, agreeing well with Chuah *et al.*'s experimental data.

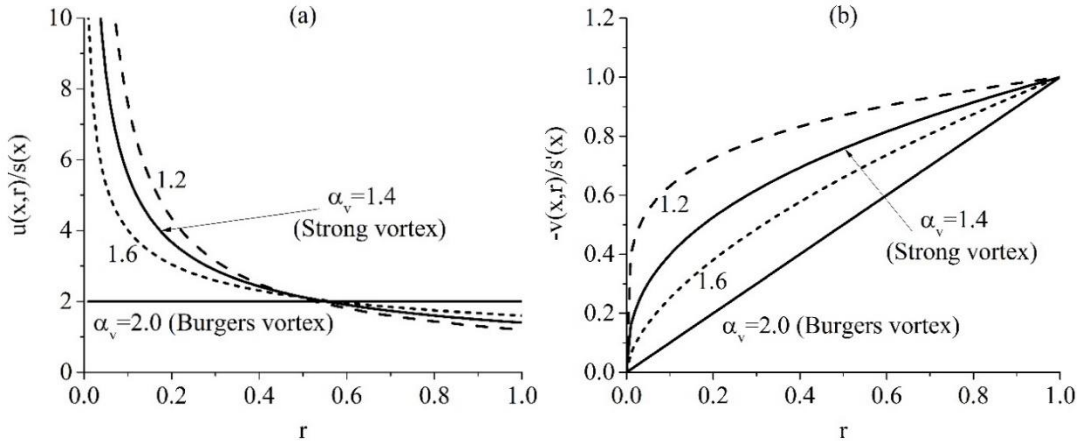

Figure 1.1 The radial profiles of (a) the axial velocity component and (b) the radial velocity component of power-law vortices.

It should be noted that Equation (1.4) with $\alpha_v < 2$ results in physically unrealistic axial velocity at the axis (i.e. $r = 0$), where the flame height is determined. To remedy the model deficiency, an alternative approach for deriving the flame height was proposed by Klimenko and Williams [35]. To facilitate a self-similar solution, which does not satisfy the boundary condition at the liquid fuel pool but is valid in the far field

of the fuel pool, the stream function and velocity components were assumed, being in accordance with the strong vortex approximation, as

$$\psi(r,x) = xf(r), \qquad u = x\frac{f'(r)}{r}, \qquad v = -\frac{f(r)}{r} \tag{1.5}$$

where the piecewise smooth function $f(r)$ is given by

$$f(r) = \begin{cases} r_c^{\alpha_v - 2} r^2, & r \le r_c \\ r^{\alpha_v}, & r \ge r_c \end{cases} \tag{1.6}$$

The singularity of the axial velocity at the axis is absent in the modified power-law vortex model by taking into account of a viscous vortex core of radius r_c. The flow within vortex core is similar to that of the Burgers vortex with $\alpha_v = 2$. Consequently, the influence of the unspecified vortex core radius on the flame height was accounted for in Equation (1.2) by treating α_v as a fitting parameter in the paper of Klimenko and Williams[35].

In spite of these worthy advances in understanding the factors affecting the firewhirl lengths, the approximation of constant density that is always invoked in the previous studies[13, 35] has not been adequately justified. The influence of density variation arising from the large temperature nonuniformity of firewhirl cannot be simply neglected. Because the decrease of density and hence the flow inertia within the high-temperature vortex core of a firewhirl flow renders the fuel mass more readily to be advected to a larger height. The Boussinesq assumption is often applied to account for the effect of variable density in body force, but it is not applicable for circulation-

controlled firewhirls [35]. It is noted that the "non-Boussinesq" approximation adopted in Battaglia et al.[6] for large temperature and density variations is essentially a low Mach number approximation that is however inappropriate when the circulation became sufficiently intense, corresponding to Ro being less than a threshold value 0.5.

In chapter II, we established a "variable density and diffusivity" model in order to propose an alternative interpretation to the experimentally observed flame height of the circulation-controlled firewhirls, in which the assumptions (A-1), large Peclet number, (A-3), Burgers vortex model, and (A-4), unity Lewis number, are retained [75]. By analytically solving the problem in the coupling function formulation, a flame height formula was derived as

$$\frac{x_h}{d_0} = \left(\frac{T_m}{T_0}\right)^{2-\alpha_T} \frac{Pe}{16 Z_{st}} \tag{1.7}$$

where the multiplicative factor, $(T_m/T_0)^{2-\alpha_T}$, is always larger than unity and therefore provides another enhancement mechanism for the flame height due to variable density. This is because the "mean" temperature T_m, which denotes an exact albeit complicated integral of flow temperature, is always higher than T_0, and the parameter α_T, which is the exponent in the power-law formula characterizing the temperature-dependence of mass diffusivity, is always less than 2. For $\alpha_T = 1.5$ from the kinetic theory of gases employing rigid-sphere model, and $\alpha_T = 1.8$ suggested by Chuah *et al.* [13], the predictions of Equation (1.7) agree well with Chuah *et al.*'s experimental data.

It is seen that Equations (1.2) and (1.7) provide distinctly different "enhancement" mechanisms for predicting the flame heights, both reveal essential physics of the circulation-controlled firewhirls, and separately lead to results agreeing well with the experimental observations. It motivates that these two independent mechanisms must be integrated into a unified formulation. Nevertheless, it was subsequently found that any simple combination of these mechanisms could overshoot the experimental data of flame heights, implying that additional "loss" mechanisms may have been overlooked in the previous studies. Inspired by the classical results on single droplet combustion in a quiescent environment [40], that the d^2-law theory based on the unity-Lewis-number and equal-diffusivity assumptions significantly overestimates the flame standoff distance, and accounting for that the much smaller diffusivity of fuel vapor compared with that of oxidizer can substantially reduce the distance, we hypothesized that the dissimilar diffusivities of liquid fuel and air in Chuah *et al.*'s experiments might play a similar role of reducing the flame height. Specifically, the shape of the non-premixed firewhirl flame is determined by the local stoichiometry; the smaller mass-diffusivity of fuel vapor results in that the iso-surface of stoichiometry tends to move towards the fuel pool.

In chapter III, we established a theory to investigate the flame heights of circulation-controlled firewhirls by integrating the following three factors based on the above considerations, but still retaining the assumptions of (A-1), large Peclet number,

and (A-4), unity Lewis numbers for both fuel and oxidizer. First, the physical properties such as density and mass diffusivity are treated as variables as it is dealt with in chapter II. Second, the mass diffusivities are distinct on the fuel and oxidizer sides of the flame. Third, a singularity-free power-law vortex model, consisting two power-law regimes with different exponents, is adopted. Solving the coupling function formulation by means of approximate matching approach, a composite flame height expression is derived as

$$\frac{x_h}{d_0} = \alpha_D \frac{2}{\alpha_v} \left(\frac{T_m}{T_0}\right)^{2-\alpha_T} \frac{Pe}{16 Z_{st}} \tag{1.8}$$

where the parameter $\alpha_D = D_F/D_O$ specifies one appropriate loss mechanism for the flame height since the fuel adopted in Chuah et al.'s experiments are methanol, ethanol and 2-propanol, whose molecular weights are all larger than that of air, thus having smaller mass diffusivities according to Chapman-Enskog theory, indicating that the parameter α_D must be less than unity.

Of the four assumptions in Chuah et al.'s theory, (A-1), the large Peclet number, reveals the physics responsible for the circulation-controlling effect, thus should definitely be retained. Whereas in many combustion problems, (A-4), the unity-Lewis number assumptions, can seldom be exactly satisfied[40, 69], which facilities the theoretical study on the effect of non-unity Lewis number in the circulation-controlled firewhirls. In general case of non-unity and non-equal Lewis numbers, the conventional coupling function formulation turns to be invalid. The exact solution to such problem

requires the matching of mass fractions of fuel and oxidizer at the two-dimensional flame locations, the contour of which remains to be specified and depends on the matched solutions themselves, which in the end must involve iterations. The mathematical formulation of such matching method turns to be extremely complicated, thus can hardly be solved analytically.

In chapter IV, we consider a particular situation that the deviations of Lewis numbers from unity can be regarded as a small quantities, thereby the Lewis-number-weighted mass fractions of fuel and oxidizer can be expanded in asymptotic series[15]. The modified coupling functions thus formed possess better mathematical properties at flame location, being continuous in both value and gradient, than the conventional ones, having discontinuities in gradient there. More importantly, the modified coupling functions can be solved by means of perturbation method. In leading order approximation, the modified coupling functions satisfy the conservation equations as if the Lewis numbers were unity. The inhomogeneous terms in the equations for the first order problem can be determined by their leading order solutions, implying that first order modified coupling functions can be solved in terms of Green's function, which can be regarded as the inverse to the differential operator of the first order problem. The combinations of leading and first orders of modified coupling functions can completely specify the combustion system in asymptotic sense, thereby the flame contour and flame height can be derived, which in leading order approximation can be written as

$$\frac{x_h}{d_0} = \frac{Le_O}{Le_F}\frac{2}{\alpha_v}\left(\frac{T_m}{T_0}\right)^{2-\alpha_T}\frac{Pe}{16Z_{st}} \tag{1.9}$$

In first order approximation, the above expression tends to be modified by the deviations of Lewis numbers from unity.

In chapter V, a concluding remark is presented on the progressive theoretical studies in Chapter II – IV on the flame height of circulation-controlled firewhirls.

Chapter II Variable Physical Properties Effects

2.1 Coupling function formulation

A firewhirl is called circulation-controlled when the vortex-stretching effect plays a dominant role in determining the flame height and the buoyancy effect is negligible. We consider such a firewhirl as a steady non-premixed flame in a forced, axisymmetric rotating flow with chemical reaction in place[11, 13, 35, 36]. The schematic of such a firewhirl is shown in Figure 2.1.

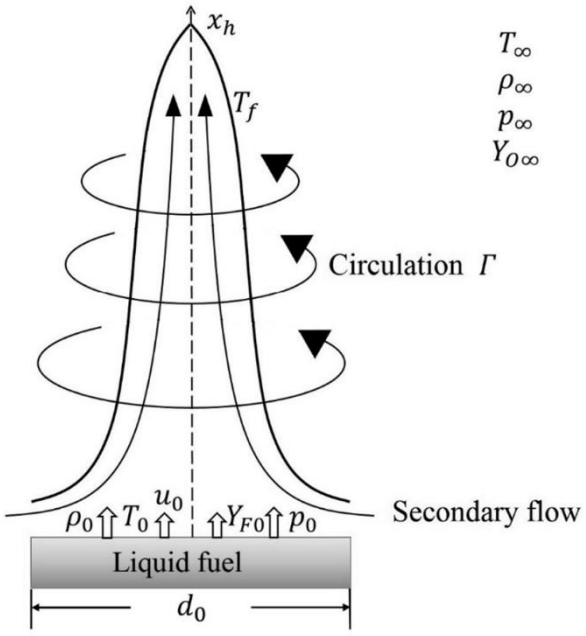

Figure 2.1. Schematic of circulation-controlled firewhirls

The flow temperature varies considerably in space due to the large heat release from the flame and therefore causes a substantial variation in density as the pressure change insignificantly in low Mach number flows[40]. To analytically characterize the

firewhirl, we need to solve the spatial distributions of fuel, oxidizer mass fractions and temperature, which constitute two coupling functions β_{FO} and β_{FT} defined by

$$\beta_{FO} = \tilde{Y}_F - \tilde{Y}_O \tag{2.1}$$

$$\beta_{FT} = \tilde{Y}_F + \tilde{T} \tag{2.2}$$

by assuming that the fuel and oxidizer have equal density-weighted mass diffusivity ρD and the Lewis number $Le = \lambda/\rho c_p D$ is unity.

The dimensional transport equation for the coupling functions can be written as

$$\rho ur \frac{\partial \beta_{FO}}{\partial x} + \rho vr \frac{\partial \beta_{FO}}{\partial r} = \frac{\partial}{\partial x}\left(\rho Dr \frac{\partial \beta_{FO}}{\partial x}\right) + \frac{\partial}{\partial r}\left(\rho Dr \frac{\partial \beta_{FO}}{\partial r}\right) \tag{2.3}$$

$$\rho ur \frac{\partial \beta_{FT}}{\partial x} + \rho vr \frac{\partial \beta_{FT}}{\partial r} = \frac{\partial}{\partial x}\left(\rho Dr \frac{\partial \beta_{FT}}{\partial x}\right) + \frac{\partial}{\partial r}\left(\rho Dr \frac{\partial \beta_{FT}}{\partial r}\right) \tag{2.4}$$

The boundary conditions (BC for short hereinafter) for Equations (2.3) and (2.4) are specified as follows:

BC(i) at $r = 0$,

$$\frac{\partial \beta_{FO}}{\partial r} = \frac{\partial \beta_{FT}}{\partial r} = 0$$

BC(ii) at $r \to \infty$

$$\frac{\partial \beta_{FO}}{\partial r} = \frac{\partial \beta_{FT}}{\partial r} = 0$$

BC(iii-a) at $x = 0$ and $r \le r_0$

$$\beta_{FO} = \tilde{Y}_{F0}$$

$$\beta_{FT} = \tilde{Y}_{F0} + \tilde{T}_0$$

BC(iii-b) at $x = 0$ and $r > r_0$

$$\frac{\partial \beta_{FO}}{\partial x} = \frac{\partial \beta_{FT}}{\partial x} = 0$$

BC(iv) at $x \to \infty$

$$\beta_{FO} = -\tilde{Y}_{O\infty}, \qquad \beta_{FT} = \tilde{T}_{\infty}$$

BC(i) specifies to the axisymmetric condition in radial direction. BC(ii) refers to the natural condition far away from the axis of symmetric in radial direction. It should be noted that it contains two unspecified quantities, $\tilde{Y}_{F0}$ and $\tilde{T}_0$ in BC(iii-a), whose determination belongs to a part of the "closure problem", describing the additional physical conditions on a liquid fuel pool of radius r_0: the diffusive and convective transport of fuel is balanced by the fuel evaporation[13, 40], which is driven by heat transport from the flame [40]. Such closure problem will be discussed in detail in the end of this chapter. Being compatible with BC (ii), BC(iv) literally indicates that no fuel is present in the far field of the fuel source, as the result of the assumption of infinitely fast reaction rate or equivalently the flame sheet assumption. The reason for adopting the infinite fast reaction rate assumption can be interpreted that the flame scale in the current problem is not limited to intermediate size, implying that the heat loss effect is inconsiderable, therefore the reaction characteristic time scale should be much smaller than that of the flow, indicating that the chemical reaction within the firewhirls can be regarded as in equilibrium.

2.2 Coordinate transformation

To transform Equations (2.3) and (2.4) into an analytically tractable form, we shall first rewrite it in terms of the non-dimensional variables defined in the nomenclature, and then introduce a density-mass diffusivity-weighted coordinate system defined by

$$\xi = \frac{D_0}{u_0 r_0}\int_0^{\tilde{x}} \tilde{\rho}^2 \widetilde{D}\, dx', \qquad \eta = \int_0^{\tilde{r}} \tilde{\rho} dr' \tag{2.5}$$

which is an analog of the well-known Howarth-Dorodnitsyn transformation[14] for compressible boundary layers, in spite of the latter is particularly useful for self-similar flow fields. In the present problem, the flow is not self-similar because of the characteristic length scale r_0. It is noted that the strong-vortex solution of Klimenko and Williams[35] was obtained by forcing self-similarity in the firewhirl flow.

Applying the transformation (2.5) to Equations (2.3) and (2.4), we can have

$$\begin{aligned}\hat{u}\frac{\partial \beta_{FO}}{\partial \xi} + \hat{v}\frac{\partial \beta_{FO}}{\partial \eta} &= \frac{4}{Pe^2\tilde{\rho}}\left(\frac{\partial}{\partial \xi} + h\frac{\partial}{\partial \eta}\right)\left[\tilde{\rho}^3\widetilde{D}^2\left(\frac{\partial \beta_{FO}}{\partial \xi} + h\frac{\partial \beta_{FO}}{\partial \eta}\right)\right] \\ &+ \left(\frac{2g}{Pe\tilde{\rho}\tilde{r}}\frac{\partial}{\partial \xi} + \frac{1}{\tilde{\rho}^2\widetilde{D}\tilde{r}}\frac{\partial}{\partial \eta}\right)\left(\frac{2\tilde{\rho}^3\widetilde{D}^2 g\tilde{r}}{Pe}\frac{\partial \beta_{FO}}{\partial \xi}\right. \\ &\left. + \tilde{\rho}^2\widetilde{D}\tilde{r}\frac{\partial \beta_{FO}}{\partial \eta}\right)\end{aligned} \tag{2.6a}$$

$$\hat{u}\frac{\partial \beta_{FT}}{\partial \xi}+\hat{v}\frac{\partial \beta_{FT}}{\partial \eta}$$
$$=\frac{4}{Pe^2\tilde{\rho}}\left(\frac{\partial}{\partial \xi}+h\frac{\partial}{\partial \eta}\right)\left[\tilde{\rho}^3\widetilde{D}^2\left(\frac{\partial \beta_{FT}}{\partial \xi}+h\frac{\partial \beta_{FT}}{\partial \eta}\right)\right]$$
$$+\left(\frac{2g}{Pe\tilde{\rho}\tilde{r}}\frac{\partial}{\partial \xi}+\frac{1}{\tilde{\rho}^2\widetilde{D}\tilde{r}}\frac{\partial}{\partial \eta}\right)\left(\frac{2\tilde{\rho}^3\widetilde{D}^2 g\tilde{r}}{Pe}\frac{\partial \beta_{FT}}{\partial \xi}\right.$$
$$\left.+\tilde{\rho}^2\widetilde{D}\tilde{r}\frac{\partial \beta_{FT}}{\partial \eta}\right) \quad (2.6b)$$

where we have

$$g(\tilde{x},\tilde{r})=\frac{1}{\tilde{\rho}^2\widetilde{D}_F}\int_0^{\tilde{x}}\frac{\partial}{\partial \tilde{r}}\left(\tilde{\rho}^2\widetilde{D}_F\right)dx' \quad (2.7a)$$

$$h(\tilde{x},\tilde{r})=\frac{Pe}{2\tilde{\rho}^2\widetilde{D}_F}\int_0^{\tilde{r}}\frac{\partial \tilde{\rho}}{\partial \tilde{x}}dr' \quad (2.7b)$$

to account for the variations of density and mass diffusivity gradients in axial and radial directions. In addition, the non-dimensional velocity components in Equations (2.6a) and (2.6b) are given by

$$\hat{u}=2\tilde{u}+2g\tilde{v}, \qquad \hat{v}=2h\tilde{u}+\frac{Pe}{\tilde{\rho}\widetilde{D}_F}\tilde{v} \quad (2.8)$$

The detailed derivations in the coordinate transformation have been presented in the Appendix A. Correspondingly, the boundary conditions BC(i-iv) are rewritten in the following form

BC(i') at $\eta=0$

$$\frac{\partial \beta_{FO}}{\partial \eta}=\frac{\partial \beta_{FT}}{\partial \eta}=0$$

BC(ii') at $\eta \to \infty$

$$\frac{\partial \beta_{FO}}{\partial \eta} = \frac{\partial \beta_{FT}}{\partial \eta} = 0$$

BC(iii-a') at $\xi = 0$ and $\eta \leq 1$

$$\beta_{FO} = \tilde{Y}_{F0}$$

$$\beta_{FT} = \tilde{Y}_{F0} + \tilde{T}_0$$

BC(iii-b') at $\xi = 0$ and $\eta > 1$

$$\frac{\partial \beta_{FO}}{\partial \xi} = \frac{\partial \beta_{FT}}{\partial \xi} = 0$$

BC(iv') at $\xi \to \infty$

$$\beta_{FO} = -\tilde{Y}_{O\infty}, \qquad \beta_{FT} = \tilde{T}_{\infty}$$

As far as the circulation-controlled firewhirls being concerned, we can apply the large Peclet number approximation, i.e., $Pe \gg 1$, to simply the above equations. Physically, the firewhirl with large Peclet numbers is substantially elongated along the axial direction due to the strong axial convection dominant over the diffusion and the flame height is thus significantly larger than the radius of the fuel pool. Consequently, the axial coordinate is scaled by a factor of $2/Pe$ by the transformation (2.5) so that the non-dimensional velocities $\hat{u}$ and $\hat{v}$ in the $\xi - \eta$ space have the same order of magnitude. As a consequence, we can deduce from Equations (2.7a) and (2.7b) that $h \sim O(1), g \sim O(1)$ and $\tilde{u} \sim O(1), \tilde{v} \sim O(Pe^{-1})$, which implies that the radial velocity v in physical coordinate is smaller than u_0 by a factor $1/Pe$.

An alternative way to make the above estimations of orders of magnitude is as follows. We have used the radius of the fuel pool to nondimensionalize the coordinates, so the derivative with respect to the axial coordinate yields an $1/Pe$, which cancels out with a factor of Pe outside the integral in Equations (2.7a) and (2.7b), resulting in $h \sim O(1)$. Because $\tilde{\rho}^2\tilde{D}$ weakly depends on temperature so that its radial derivative is of $O(1/Pe)$, which is cancelled out by another factor of Pe produced from the axial integration of the radial derivative, rendering g to be of $O(1)$.

Based on the above considerations, we can neglect all the terms of $O(Pe^{-1})$ and $O(Pe^{-2})$ in Equations (2.6a) and (2.6b) and invoke a less restrictive Chapman-Rubesin-like approximation that

$$\tilde{\rho}^2\tilde{D}\tilde{r}\left(\int_0^{\tilde{r}}\tilde{\rho}dr'\right)^{-1} = C(\xi) \tag{2.9}$$

is independent of the coordinate η, and is assumed to be a global constant [59], the Equations (2.6a) and (2.6b) can be simplified to

$$\hat{u}\frac{\partial\beta_{FO}}{\partial\xi} + \hat{v}\frac{\partial\beta_{FO}}{\partial\eta} = \frac{1}{\eta}\frac{\partial}{\partial\eta}\left(\eta\frac{\partial\beta_{FO}}{\partial\eta}\right) \tag{2.10a}$$

$$\hat{u}\frac{\partial\beta_{FT}}{\partial\xi} + \hat{v}\frac{\partial\beta_{FT}}{\partial\eta} = \frac{1}{\eta}\frac{\partial}{\partial\eta}\left(\eta\frac{\partial\beta_{FT}}{\partial\eta}\right) \tag{2.10b}$$

In the same way, the boundary conditions become

BC(i'') at $\eta = 0$

$$\frac{\partial \beta_{FO}}{\partial \eta} = \frac{\partial \beta_{FT}}{\partial \eta} = 0$$

BC(ii'') at $\eta \to \infty$

$$\frac{\partial \beta_{FO}}{\partial \eta} = \frac{\partial \beta_{FT}}{\partial \eta} = 0$$

BC(iii-a'') at $\xi = 0$ and $\eta \leq 1$

$$\beta_{FO} = \tilde{Y}_{F0}$$

$$\beta_{FT} = \tilde{Y}_{F0} + \tilde{T}_0$$

BC(iii-b'') at $\xi = 0$ and $\eta > 1$

$$\beta_{FO} = -\tilde{Y}_{O\infty}, \qquad \beta_{FT} = \tilde{T}_\infty$$

The mixed boundary condition BC(iii-a') is replaced by the Dirichlet boundary condition BC(iii-a'') for mathematical convenience without losing the physics because the determination of the fuel vapor concentration $\tilde{Y}_{F0}$ requires BC(iii-a'). The coupling function is valid in the whole flow field so that β_{FT} and β_{FO} must satisfy BC(iii-a''), given the quantities on the evaporating fuel pool are known. BC(iii-b'') actually implies an isothermal ground surface outside the pool flame. Such a boundary condition is not required by the previously theories [13, 35] based on the mixture fraction formulation, but it brings significant mathematical convenience to the theoretical analysis based on the coupling function formulation, resulting in the Burke-Schumann-like solutions produced by the mixture fraction formulations [13, 35]. One could formulate a theory with a prescribed ground temperature profile $\tilde{T}_w$, which however lacks experimental

data and causes unnecessary mathematical complexities. Furthermore, the wall temperature $\tilde{T}_w$, being scaled by the heat of combustion q_c/c_p, is much smaller than the flame temperature $\tilde{T}_f$ and the mass fractions $\tilde{Y}_F$ and $\tilde{Y}_O$. In consequence, replacing $\tilde{T}_\infty$ by $\tilde{T}_w$ in the solutions of β_{FT} and β_{FO} is unlikely to make significant difference. Moreover, BC(iv') is not needed for solving Equations (2.10a) and (2.10b) which are parabolic partial differential equations.

Formally, we can regard the coordinates (ξ, η) as "constant density" ones, in which we approximate the firewhirl flow as a Burgers vortex[13]. Burgers vortex[9] is a generalization of two-dimensional Oseen vortex[62] by introducing an additional linear radial and axial secondary flow to account for the vortex-stretching effect, which plays a crucial role in determining the flame heights of circulation-controlled firewhirls. The stream function of the Burgers vortex is given by

$$\psi = \left(\frac{\tilde{a}}{2}\xi + \frac{1}{2}\right)\eta^2 \tag{2.11}$$

In terms of the stream function ψ, the axial velocity $\hat{u}$, the scaled radial velocity $\hat{v}$, and the azimuthal velocity $\hat{w}$ can be expressed by

$$\hat{u} = \frac{1}{\eta}\frac{\partial \psi}{\partial \eta} = \tilde{a}\xi + 1 \tag{2.12}$$

$$\hat{v} = -\frac{1}{\eta}\frac{\partial \psi}{\partial \xi} = -\frac{1}{2}\tilde{a}\eta \tag{2.13}$$

$$\hat{w} = \frac{\tilde{\Gamma}}{2\pi\eta}\left[1 - \exp\left(-\frac{\tilde{a}\eta^2}{4\tilde{\nu}}\right)\right] \tag{2.14}$$

In the physical coordinates, Equations (2.12)-(2.14) can be written as

$$\hat{u} = a\int_0^x \left(\frac{\rho}{\rho_0}\right)^2 \frac{D}{D_0} dx' + u_0 \tag{2.15}$$

$$\hat{v} = -\frac{1}{2} a \frac{\rho}{\rho_0}\frac{D}{D_0}\int_0^r \left(\frac{\rho}{\rho_0}\right) dr' \tag{2.16}$$

$$\hat{w} = \frac{\Gamma}{2\pi \int_0^r \rho/\rho_0 \, dr'}\left[1 - e^{-\frac{a}{4\nu}\left(\int_0^r \frac{\rho}{\rho_0} dr'\right)^2}\right] \tag{2.17}$$

where the integrals in the velocity components represent the stretching effects of the density variation. Given that the density is a slowly-varying function of x and Chapman-Rubesin number is constant, it is readily seen that Equations (2.15)-(2.17) satisfies the equation of continuity as does the primitive model[62]. The direct validation of Equations (2.12)-(2.14) is not available in the present study while it merits future study when experimental measurements are available.

Making use of the stream function ψ, we can introduce the stream function coordinate defined as

$$\chi = \xi, \qquad \zeta = \sqrt{2\psi} \tag{2.18}$$

which was also used by Klimenko and Williams[35] in a dimensional form. Equations (2.10a) and (2.10b) can be rewritten in the stream function coordinate (χ, ζ) as

$$\frac{\partial \beta_{FO}}{\partial \chi} = \frac{1}{\zeta}\frac{\partial}{\partial \zeta}\left(\zeta \frac{\partial \beta_{FO}}{\partial \zeta}\right) \tag{2.19}$$

$$\frac{\partial \beta_{FT}}{\partial \chi} = \frac{1}{\zeta}\frac{\partial}{\partial \zeta}\left(\zeta \frac{\partial \beta_{FT}}{\partial \zeta}\right) \tag{2.20}$$

Correspondingly, the boundary conditions are transformed to

BC(a) at $\zeta = 0$

$$\frac{\partial \beta_{FO}}{\partial \zeta} = \frac{\partial \beta_{FT}}{\partial \zeta} = 0$$

BC(b) at $\zeta \to \infty$

$$\frac{\partial \beta_{FO}}{\partial \zeta} = \frac{\partial \beta_{FT}}{\partial \zeta} = 0$$

BC(c-1) at $\chi = 0$ and $\zeta \leq 1$

$$\beta_{FO} = \tilde{Y}_{F0}, \qquad \beta_{FT} = \tilde{Y}_{F0} + \tilde{T}_0$$

BC(c-2) at $\chi = 0$ and $\zeta > 1$

$$\beta_{FO} = -\tilde{Y}_{O\infty}, \qquad \beta_{FT} = \tilde{T}_\infty$$

Equations (2.19) and (2.20) together with BCs (a)-(c) constitute an analytically solvable formulation describing the firewhirl problem, to be solved in the following section.

2.3 Solution for coupling functions

Equations (2.19) and (2.20) can be solved by means of separation of variables which results in the Bessel function of the first kind[69]. After taking into account of BCs (a)-(c), we have

$$\beta_{FO} = -\tilde{Y}_{O\infty} + \left(\tilde{Y}_{F0} + \tilde{Y}_{O\infty}\right) \int_0^\infty J_1(\omega) J_0(\omega\zeta) e^{-\omega^2 \chi} d\omega \tag{2.21}$$

$$\beta_{FT} = \tilde{T}_\infty + \left(\tilde{T}_0 + \tilde{Y}_{F0} - \tilde{T}_\infty\right) \int_0^\infty J_1(\omega) J_0(\omega\zeta) e^{-\omega^2 \chi} d\omega \tag{2.22}$$

where J_0 and J_1 are the zeroth- and the first-order Bessel functions of the first kind, respectively.

The flame location, expressed by $\chi_f = f(\zeta)$, can be determined by using $\beta_{FO} = 0$ in Equation (2.21) because the reactants vanish on the non-premixed flame sheet. Since oxidizer is absent on the fuel side in the flame-sheet assumption, $\tilde{Y}_F$ is determined from Equation (2.21) by

$$\tilde{Y}_F = \beta_{FO} = -\tilde{Y}_{O\infty} + \left(\tilde{Y}_{F0} + \tilde{Y}_{O\infty}\right) \int_0^\infty J_1(\omega) J_0(\omega\zeta) e^{-\omega^2 \chi} d\omega \tag{2.23}$$

and $\tilde{T}$ from Equations (2.21) and (2.22) by

$$\begin{aligned} \tilde{T} &= \beta_{FT} - \beta_{FO} \\ &= \tilde{T}_\infty + \tilde{Y}_{O\infty} + \left(\tilde{T}_0 - \tilde{T}_\infty - \tilde{Y}_{O\infty}\right) \int_0^\infty J_1(\omega) J_0(\omega\zeta) e^{-\omega^2 \chi} d\omega \end{aligned} \tag{2.24}$$

Similarly, fuel vanishes on the oxidizer size and we hence have

$$\tilde{Y}_O = -\beta_{FO} = \tilde{Y}_{O\infty} - \left(\tilde{Y}_{F0} + \tilde{Y}_{O\infty}\right) \int_0^\infty J_1(\omega) J_0(\omega\zeta) e^{-\omega^2 \chi} d\omega \qquad (2.25)$$

and

$$\tilde{T} = \beta_{FT} = \tilde{T}_\infty + \left(\tilde{T}_0 + \tilde{Y}_{F0} - \tilde{T}_\infty\right) \int_0^\infty J_1(\omega) J_0(\omega\zeta) e^{-\omega^2 \chi} d\omega \qquad (2.26)$$

Transforming χ and ζ in the Equations (2.23)-(2.26) back to $\tilde{x}$ and $\tilde{r}$ and expressing $\tilde{T}$ and $\tilde{Y}$ in their dimensional forms, we can obtain the spatial distributions of T, Y_F and Y_O in physical coordinates and hence the firewhirl is completely determined.

2.4 Flame height and variable density effect

The flame height of the firewhirls is defined as the highest flame location on the χ-axis and denoted by χ_h, which can be determined by setting both ζ and β_{FO} equal to zero in Equation (2.21), yielding

$$\int_0^\infty J_1(\omega) e^{-\omega^2 \chi_h} d\omega = \frac{\tilde{Y}_{O\infty}}{\tilde{Y}_{F0} + \tilde{Y}_{O\infty}} = Z_{st} \qquad (2.27)$$

In actual experimental conditions, the flame height is usually significantly larger than the radius of fuel source pool, namely, $\chi_h \gg 1$. Therefore, the integral on the LHS of Equation (2.27) is mainly attributed to a small region around $\omega = 0$ [55]. By using the Taylor expansion of the Bessel function $J_1(\omega)$ around $\omega = 0$, i.e.,

$$J_1(\omega) = \frac{\omega}{2} - \frac{\omega^3}{16} + \cdots \tag{2.28}$$

substituting it into Equation (2.27), and using integration by parts, we have

$$\frac{1}{4\chi_h}\left(1 - \frac{1}{8\chi_h}\right) = Z_{st} \tag{2.29}$$

Therefore, we can write the approximate flame height expression as

$$\chi_h = \frac{1}{4Z_{st}} - \frac{1}{8} \tag{2.30}$$

where only the first two terms in the Taylor expansion were used because of $8\chi_h \gg 1$. To facilitate the comparison with previous experimental observations, we write χ_h in its dimensional form by

$$\chi_h = \frac{1}{\rho_0^2 u_0 r_0^2}\int_0^{x_h} \rho^2 D dx = \frac{T_0^2}{u_0 r_0^2}\int_0^{x_h} \frac{D}{T^2} dx \tag{2.31}$$

To derive the above equation, we have adopted the isobaric approximation [13, 35, 40] which has been well justified in low Mach number flows. Substituting (2.31) to the LHS of Equation (2.30), we have

$$\int_0^{x_h} T^{a_T-2} dx = \mathrm{Pe} T_0^{a_T-2} d_0 \left(\frac{1}{16Z_{st}} - \frac{1}{32}\right) \tag{2.32}$$

where the mass diffusivity in arbitrary axial location is related to D_0 at $x = 0$ through the relation

$$D = D_0\left(\frac{T}{T_0}\right)^{\alpha_T} \tag{2.33}$$

in which α_T is usually less than 2 [13, 72] and equal to 1.5 in the kinetic theory of gases employing the rigid-sphere model [40]. It should be noted that we do not distinguish the mass diffusivities of fuel and oxidizer in this Chapter, thus D may equivalently refer to D_F for fuel or D_O for oxidizer.

Because Z_{st} is around 0.1 under the actual experimental conditions[13], we can neglect 1/32 in Equation (2.32) and formally rewrite the equation as

$$\frac{x_h}{d_0} = \left(\frac{T_m}{T_0}\right)^{2-a_T} \frac{\mathrm{Pe}}{16 Z_{st}} \tag{2.34}$$

which has exactly the same form as that given by Klimenko and Williams[35] except for the additional term $(T_m/T_0)^{2-a_T}$ describing variable density effect on the flame heights. Introduced for mathematical convenience, T_m denotes the integral

$$T_m = \left[\frac{1}{x_h}\int_0^{x_h} T^{a_T-2} dx\right]^{1/(\alpha_T-2)} \tag{2.35}$$

and is determined, with the help of Equation (2.24), by

$$T_m = \left\{\frac{1}{x_h}\int_0^{x_h}\left[T_\infty + \frac{q_c Y_{O\infty}}{\sigma_{FO} c_p} + \left(T_0 - \frac{q_c Y_{O\infty}}{\sigma_{FO} c_p}\right)\times \int_0^\infty J_1(\omega)\exp\left(-\omega^2\int_0^{x/r_0}\tilde{\rho}^2\widetilde{D}\,dx'\right)d\omega\right]^{\alpha_T-2} dx\right\}^{\frac{1}{\alpha_T-2}} \tag{2.36}$$

Considering that directly evaluating T_m by means of (2.36) is mathematically challenging due to multiple-fold integrations of a product of Bessel function with exponential function, we can roughly estimate T_m by the arithmetic mean, the

geometric average or the well-known $1/3$-rule[40] to facilitate the interpretation of variable density effects and the comparison between theory and experiments.

For the following illustrations, both the $1/3$-rule,

$$T_m \cong \frac{T_0 + 2T_f}{3} \tag{2.37}$$

and the arithmetic mean,

$$T_m \cong \frac{T_0 + T_f}{2} \tag{2.38}$$

are adopted to estimate T_m, where the quantity T_f denotes the flame temperature. In Chuah et al.'s experiments, T_f of alcohols (methanol, ethanol and 2-propanol) are estimated at 1300K [13] rather than 1500K[72] since the alcohols burn cooler than hydrocarbons. T_0 is approximated as 337K, the boiling point temperature of methanol at atmospheric pressure, although T_0 should be lower than the actual boiling point temperature. The slight difference of the boiling point temperatures between methanol (337K) and 2-propanol (370K) does not cause any significant change to the temperature factor $(T_m/T_0)^{2-a_T}$. Two typical values for the exponent α_T, such as 1.5 from the kinetic theory of gases[40] and 1.8 suggested by Chuah et al. [13], will be used and compared to minimize the uncertainty caused by the choice of the exponent.

Figure 2.2 shows the present theoretical predictions for different values of α_T and different estimates of the mean temperature. For comparison, the previous theoretical results based on the constant density assumption are also shown and can be readily

reproduced by using a physically unrealistic value of $\alpha_T = 2$ in the present theory. It is seen that the constant density predictions result in a linear relation with a unity slope in the parameter space of the normalized flame height, x_h/d_0, and the modified Peclet number, $\mathrm{Pe}/16Z_{st}$. When the variable density effect is taken into account in the present theory, the linearity between x_h/d_0 and $\mathrm{Pe}/16Z_{st}$ remains while the slope is modified by a factor $(T_m/T_0)^{2-\alpha_T} > 1$ because $T_m > T_0$ and $\alpha_T < 2$. This result implies that the flame height undergoes an additional increase in circulation-controlled firewhirls when the variable density effect is taken into account. The underlying physics can be understood by that the decrease of density and hence the flow inertia within the high-temperature vortex core of a firewhirl flow renders the fuel mass more readily to be advected to a larger height.

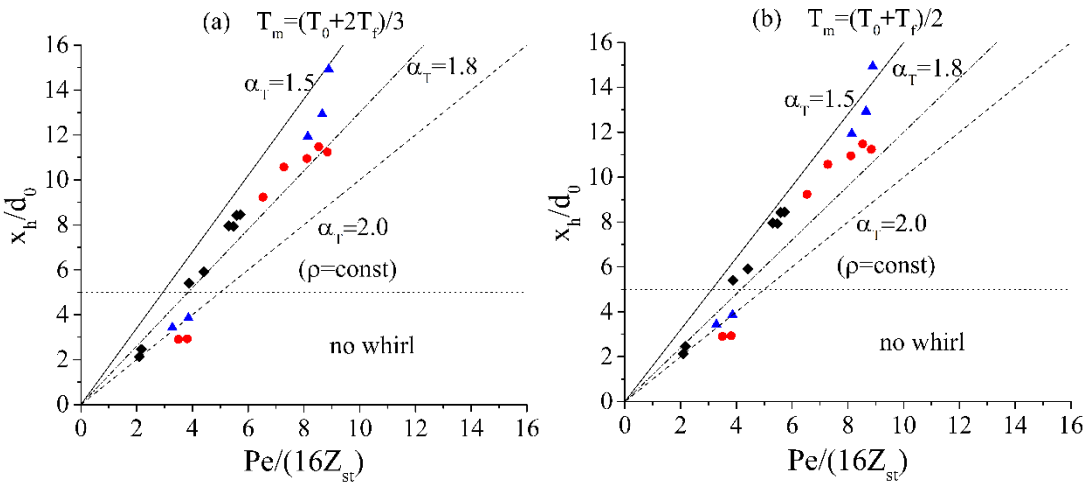

Figure 2.2 Normalized flame length plotted against normalized Peclet number. Solid symbols represent experimental data given by Chuah et al[13]. Fuel types are distinguished by solid symbols, methanol (♦), ethanol (●), 2-propanol (▲).

It is also seen by comparing Figure 2.2(a) with Figure 2.2(b) that the different approximation methods for estimating the mean temperature T_m do not cause any qualitative changes to the theoretical predictions. Furthermore, the good agreements with the experimental data have been achieved by the present theory with either $\alpha_T = 1.5$ or $\alpha_T = 1.8$, while the latter seems better and more physically realistic. It is noted that the present theory seems to moderately overestimate the experimental data below the horizontal dot line, which however represent the experimental cases without whirl and therefore should not be used for a direct comparison. As circulation decreases, the buoyancy effect may become a nontrivial or even dominant factor in determining the flame height.

An alternative way to estimate T_f is by evaluating Equation (2.24) at x_h and setting ζ equal to zero. Neglecting the slight difference between $\tilde{T}_\infty$ and $\tilde{T}_0'$ in most actual situations and evaluating T_m and using the arithmetic mean as an example, we have

$$\frac{x_h}{d_0} = \left(\frac{1+\kappa}{2} + \kappa \frac{q_c}{2c_p T_0} Z_{st}\right)^{2-\alpha_T} \frac{\mathrm{Pe}}{16 Z_{st}} \tag{2.39}$$

where the inclusion of the coefficient κ is to account for possible heat loss due to radiation and other factors, which might play important role and therefore merits further studies. Although it is noted that q_c and Z_{st} do not vary significantly for common hydrocarbon fuels, Equation (2.39) also indicates the influence of other physical-

chemical properties, such as c_p and T_0 on the flame height. Detailed investigation on these properties is beyond the scope of the present study due to the currently unavailable experimental data.

2.5 Specification of boundary conditions for condensed fuels

Because the fuel pool is in condensed phase, the physics of Stefan flow at the evaporating surface should be considered to derive three auxiliary equations to determine the fuel vapor mass fraction Y_{F0}, the Stefan flow velocity u_0, and the temperature T_0, for closuring the two-phase problem. First, the axial diffusive and convective transport of fuel feeding the flame is balanced by the fuel evaporation from liquid phase to gaseous phase, yielding a mass balance equation. Second, the energy required by the evaporation is supplied by the heat transport from the flame, yielding the energy balance equation. Third, the Clausius-Clapeyron equation is needed to relate Y_{F0} and T_0. In addition, the equation of state and the Bernoulli's equation can be used to determine the pressure p_0 and the density ρ_0 on the evaporation layer. For the present focus of establishing a relation between the diameter-scaled flame height x_h/d_0 and modified Peclet number $Pe/(16Z_{st})$, we can assume those physical quantities on the evaporation are prescribed. It should be also noted that only axial transport is considered to derive the auxiliary equations for the problem closure because

of the large Peclet number assumption. Therefore, the equations cannot be applied in the $O(1/Pe)$ neighborhood of the origin, where the assumption is invalid.

By applying the stretched coordinates such as $\tilde{x} = 2\tilde{x}'/Pe$, $\tilde{r} = \tilde{r}'$ to the transport equation for Y_F, we have

$$\frac{\partial}{\partial \tilde{x}'}(\tilde{\rho}\tilde{u}\tilde{r}'Y_F) + \frac{2}{\mathrm{Pe}}\frac{\partial}{\partial \tilde{r}'}(\tilde{\rho}\tilde{v}\tilde{r}'Y_F) = \frac{\partial}{\partial \tilde{x}'}\left(\tilde{\rho}\widetilde{D}\tilde{r}'\frac{\partial Y_F}{\partial \tilde{x}'}\right) + \frac{4}{\mathrm{Pe}^2}\frac{\partial}{\partial \tilde{r}'}\left(\tilde{\rho}\widetilde{D}\tilde{r}'\frac{\partial Y_F}{\partial \tilde{r}'}\right) \tag{2.40}$$

Neglecting the radial convection and diffusion terms in Equation (2.40) because of the large Peclet number and integrating the equation over $\tilde{x}'$ across the evaporation layer, we have

$$\tilde{\rho}\tilde{u}Y_F - \tilde{\rho}\widetilde{D}\frac{\partial Y_F}{\partial \tilde{x}'} = c_F \tag{2.41}$$

which indicates that the convective and diffusive transport of fuel is balanced by the evaporation. Since both the inert gas and the oxidizer gas are non-condensable, the total mass flux at the evaporating surface is completely attributed to the fuel vapor. We hence have

$$\rho u Y_F\big|_{x=0} - \rho D\frac{dY_F}{dx}\big|_{x=0} = \rho u\big|_{x=0} \tag{2.42}$$

Similarly, by considering the heat transport in the evaporation layer, we have

$$\lambda\frac{dT}{dx}\big|_{x=0} = q_v\rho u\big|_{x=0} \tag{2.43}$$

Combining Equations (2.42) and (2.43), we can solve for $Y_F(0,r)$ and $u(0,r)$ as

$$u(0,r)=\frac{D_0}{r_0}\left\{\begin{array}{l}\dfrac{c_pT_\infty-c_pT(0,r)+q_c\,Y_{O\infty}/\sigma_{FO}+q_v}{q_v}\\ \times\displaystyle\int_0^\infty \omega J_1(\omega)\left[\omega J_0\left(\frac{\omega r}{r_0}\right)+\frac{a}{2}\frac{r}{r_0}J_1\left(\frac{\omega r}{r_0}\right)\right]d\omega\end{array}\right\}^{1/2} \tag{2.44}$$

$$Y_F(0,r)=1-\frac{q_v(1+Y_{O\infty}/\sigma_{FO})}{c_pT_\infty-c_pT(0,r)+q_c\,Y_{O\infty}/\sigma_{FO}+q_v} \tag{2.45}$$

In Equations (2.44) and (2.45), $T(0,r)$ is related to $p(0,r)$ by the Clausius-Clapeyron relation,

$$\frac{Y_F(0,r)/W_F}{Y_F(0,r)/W_F+[1-Y_F(0,r)]/W_N}=\frac{p_\infty}{p(0,r)}\exp\left\{\frac{q_v}{R}\left[\frac{1}{T_{b,\infty}}-\frac{1}{T(0,r)}\right]\right\} \tag{2.46}$$

Furthermore, $p(0,r)$ can be approximately determined by using the body-force-free Bernoulli's equation and the velocity components of the Burgers vortex as follows

$$p(0,r)=p_\infty-\frac{1}{2}\rho(0,r)\left[u_0^2+\frac{1}{4}a^2r^2+\frac{\Gamma^2}{4\pi^2r^2}\left(1-e^{-ar^2/4\nu}\right)^2\right] \tag{2.47}$$

In addition, the equation of state gives another relation

$$\rho(0,r)=\frac{p(0,r)}{RT(0,r)}=\frac{p_\infty}{RT(0,r)(1+\gamma Ma^2/2)} \tag{2.48}$$

According to Equation (2.47), increasing the vortex circulation, the static pressure $p(0,r)$ over the fuel pool becomes smaller and so does the temperature $T(0,r)$ due to Equation (2.46) because the temperature is close to the boiling point temperature under the reduced pressure[40]. As a result, both $u(0,r)$ and $\rho(0,r)$ and therefore

the evaporation flux $\rho(0,r)u(0,r)$ increases with the circulation with the circulation, given that the vortex Mach number is sufficiently small.

By solving Equations (2.44)-(2.48), we can obtain Y_F, u, T, p and ρ at the evaporating fuel surface. Therefore, the firewhirl system considered in the present problem is closured with the boundary conditions specified in the section 2.2.

Chapter III Distinct Transport Properties Effect

3.1 Coupling function formulation

A circulation-controlled firewhirl is modelled as a steady non-premixed flame in a forced axisymmetric vortical flow without buoyance effects [13, 35]. By following the previous studies [13, 35, 75], we assume that the Lewis number is unity throughout the flow field to invoke a coupling-function formulation. However, we abandoned the assumption of constant physical properties by considering not only variable density but also distinct, variable transport properties on the fuel and oxidizer sides of the flame, and as such we have

$$Le_F = \frac{\lambda_F}{\rho c_p D_F} = 1;\ Le_O = \frac{\lambda_O}{\rho c_p D_O} = 1;\ \lambda_F \neq \lambda_O;\ D_F \neq D_O \tag{3.1}$$

Consequently, the present problem can be characterized by two species-enthalpy coupling functions, namely, β_F and β_O defined by

$$\beta_F = \tilde{Y}_F + \tilde{T} \tag{3.2}$$

$$\beta_O = \tilde{Y}_O + \tilde{T} \tag{3.3}$$

It is noted that the species coupling functions adopted in Chapter II are not applicable because of the distinct mass diffusivities for fuel and oxidizer. The transport equations for β_F and β_O are given by

$$\rho u\frac{\partial \beta_F}{\partial x}+\rho v\frac{\partial \beta_F}{\partial r}-\frac{\partial}{\partial x}\left(\rho D_F\frac{\partial \beta_F}{\partial x}\right)-\frac{1}{r}\frac{\partial}{\partial r}\left(\rho D_F r\frac{\partial \beta_F}{\partial r}\right)=0 \qquad (3.4)$$

$$\rho u\frac{\partial \beta_O}{\partial x}+\rho v\frac{\partial \beta_O}{\partial r}-\frac{\partial}{\partial x}\left(\frac{1}{\alpha_D}\rho D_F\frac{\partial \beta_O}{\partial x}\right)-\frac{1}{r}\frac{\partial}{\partial r}\left(\frac{1}{\alpha_D}\rho D_F r\frac{\partial \beta_O}{\partial r}\right)=0 \qquad (3.5)$$

The temperature- and pressure-dependent mass diffusivity for binary diffusion (as nitrogen is abundant in the gas mixtures) can be evaluated by using the Chapman-Enskog theory [19]. The ratio of the mass diffusivities is thus given by

$$\alpha_D=\frac{D_F}{D_O}=\frac{\delta_{FN}^2\Omega_{FN}\sqrt{1/W_F+1/W_N}}{\delta_{ON}^2\Omega_{ON}\sqrt{1/W_O+1/W_N}} \qquad (3.6)$$

Because the temperature- and pressure-dependent factors of D_F and D_O have been cancelled out in deriving the equation, α_D can be regarded as a constant in the entire flow field, only dependent on the fuel type.

Equations (3.4) and (3.5) are rigorously valid on the fuel and oxidizer sides of the flame sheet, respectively, and are approximate on the other side. The exact solutions must be determined by matching β_F and β_O at the flame sheet, where both reactants vanish and temperature is the flame temperature T_f, rendering $\beta_F=\beta_O=T_f$ [40]. Although such a matching solution approach works for one-dimensional flames such as the classical droplet flame, it is however mathematically inapplicable to the present problem because the general solution to the partial differential equations (3.4) and (3.5) cannot be obtained without the prescribed boundary conditions at the two-dimensional flame sheet. In order to resolve the mathematical difficulty, we proposed an

approximate matching solution procedure, which will be applied to the parabolized version of Equations (3.4) and (3.5) in Section 3.5.

The corresponding boundary conditions (denoted by BC for short and hereinafter) are given by

BC(1), at $r = 0$

$$\frac{\partial \beta_F}{\partial r} = \frac{\partial \beta_O}{\partial r} = 0$$

BC(2), at $r \to \infty$

$$\frac{\partial \beta_F}{\partial r} = \frac{\partial \beta_O}{\partial r} = 0$$

BC(3a), at $x = 0$ and $r \leq r_0$

$$\beta_F = \tilde{Y}_{F0} + \tilde{T}_0$$

$$\beta_O = \tilde{T}_0$$

BC(3b), at $x = 0$ and $r > r_0$

$$\frac{\partial \beta_F}{\partial x} = \frac{\partial \beta_O}{\partial x} = 0$$

BC(4), at $x \to \infty$

$$\beta_F = \tilde{T}_\infty, \qquad \beta_O = \tilde{Y}_{O\infty} + \tilde{T}_\infty$$

BC(1) and BC(2) refer to the boundary conditions at the axis and in the far field, respectively. The unspecified quantities $\tilde{Y}_{F0}$ and $\tilde{T}_0$ describes the Stefan flow in the evaporation layer, where the diffusive and convective transport of fuel along the axial

direction is balanced by the fuel evaporation, and the energy required by the evaporation is supplied by the heat transported from the flame. The determination of those quantities has been discussed in detail in the "closure problem" in the end of the last chapter, thus would not be repeated in this chapter.

3.2 Coordinate Transformation

Following the same approach adopted in Chapter II, we introduced a density-mass-diffusivity-weighted coordinate system in the form of

$$\xi = \frac{D_{F0}}{u_0 r_0}\int_0^{\tilde{x}} \tilde{\rho}^2 \widetilde{D}_F dx' = \frac{2}{Pe}\int_0^{\tilde{x}} \tilde{\rho}^2 \widetilde{D}_F dx' , \qquad \eta = \int_0^{\tilde{r}} \tilde{\rho} dr' \tag{3.7}$$

The transformation (3.7) is analogous to the well-known Howarth-Dorodnitsyn transformation [14, 51], which is widely used in self-similar compressible boundary layer problems. It should be noted that the present problem is not a self-similar flow because of the characteristic length scale r_0. A valuable self-similar solution can however be derived at the far field of fuel pool [35] and will be discussed shortly in the section 3.8.

Applying the coordinate transformation to Equations (3.4) and (3.5) as well as the boundary conditions BC(1)-(4), yields

$$\hat{u}\frac{\partial \beta_F}{\partial \xi}+\hat{v}\frac{\partial \beta_F}{\partial \eta}=\frac{4}{Pe^2\tilde{\rho}}\left(\frac{\partial}{\partial \xi}+h\frac{\partial}{\partial \eta}\right)\left[\tilde{\rho}^3\widetilde{D}_F^2\left(\frac{\partial \beta_F}{\partial \xi}+h\frac{\partial \beta_F}{\partial \eta}\right)\right]+\left(\frac{2g}{Pe\tilde{\rho}\tilde{r}}\frac{\partial}{\partial \xi}+\frac{1}{\tilde{\rho}^2\widetilde{D}_F\tilde{r}}\frac{\partial}{\partial \eta}\right)\left(\frac{2\tilde{\rho}^3\widetilde{D}_F^2 g\tilde{r}}{Pe}\frac{\partial \beta_F}{\partial \xi}+\tilde{\rho}^2\widetilde{D}_F\tilde{r}\frac{\partial \beta_F}{\partial \eta}\right) \tag{3.8}$$

$$\hat{u}\frac{\partial \beta_O}{\partial \xi}+\hat{v}\frac{\partial \beta_O}{\partial \eta}=\frac{4}{\alpha_D Pe^2\tilde{\rho}}\left(\frac{\partial}{\partial \xi}+h\frac{\partial}{\partial \eta}\right)\left[\tilde{\rho}^3\widetilde{D}_F^2\left(\frac{\partial \beta_O}{\partial \xi}+h\frac{\partial \beta_O}{\partial \eta}\right)\right]+\frac{1}{\alpha_D}\left[\frac{2g}{Pe\tilde{\rho}\tilde{r}}\frac{\partial}{\partial \xi}+\frac{1}{\tilde{\rho}^2\widetilde{D}_F\tilde{r}}\frac{\partial}{\partial \eta}\right]\left(\frac{2\tilde{\rho}^3\widetilde{D}_F^2 g\tilde{r}}{Pe}\frac{\partial \beta_O}{\partial \xi}+\tilde{\rho}^2\widetilde{D}_F\tilde{r}\frac{\partial \beta_O}{\partial \eta}\right) \tag{3.9}$$

where the functions g and h have the quite similar mathematical form as in the last chapter, i.e.

$$g(\tilde{x},\tilde{r})=\frac{1}{\tilde{\rho}^2\widetilde{D}_F}\int_0^{\tilde{x}}\frac{\partial}{\partial \tilde{r}}\left(\tilde{\rho}^2\widetilde{D}_F\right)dx' \tag{3.10}$$

$$h(\tilde{x},\tilde{r})=\frac{Pe}{2\tilde{\rho}^2\widetilde{D}_F}\int_0^{\tilde{r}}\frac{\partial \tilde{\rho}}{\partial \tilde{x}}dr' \tag{3.11}$$

as well as the physical interpretation to account for the variations of density and mass diffusivity gradients in axial and radial directions. As expected, the non-dimensional velocity components in Equations (3.8) and (3.9) are given by

$$\hat{u}=2\tilde{u}+2g\tilde{v} \tag{3.12}$$

$$\hat{v} = 2h\tilde{u} + \frac{Pe}{\tilde{\rho}\widetilde{D}_F}\tilde{v} \tag{3.13}$$

Correspondingly, the boundary conditions BCs (1)-(4) can be rewritten by

BC(1') at $\eta = 0$

$$\frac{\partial \beta_F}{\partial \eta} = \frac{\partial \beta_O}{\partial \eta} = 0$$

BC(2') at $\eta \to \infty$

$$\frac{\partial \beta_F}{\partial \eta} = \frac{\partial \beta_O}{\partial \eta} = 0$$

BC(3a') at $\xi = 0$ and $\eta \leq 1$

$$\beta_F = \tilde{Y}_{F0} + \tilde{T}_0$$

$$\beta_O = \tilde{T}_0$$

BC(3b') at $\xi = 0$ and $\eta > 1$

$$\frac{\partial \beta_F}{\partial \xi} = \frac{\partial \beta_O}{\partial \xi} = 0$$

BC(4') at $\eta \to \infty$

$$\beta_F = \tilde{T}_\infty, \qquad \beta_O = \tilde{Y}_{O\infty} + \tilde{T}_\infty$$

As far as the circulation-controlled firewhirls being concerned, we can apply the large Peclet number approximation, i.e., $Pe \gg 1$, to simply the above equations as we did in the last chapter. Based on the above considerations, we can neglect all the terms of $O(Pe^{-1})$ and $O(Pe^{-2})$ in Equations (3.8) and (3.9) and then have

$$\hat{u}\frac{\partial \beta_F}{\partial \xi} + \hat{v}\frac{\partial \beta_F}{\partial \eta} = \frac{1}{\eta}\frac{\partial}{\partial \eta}\left(\eta \frac{\partial \beta_F}{\partial \eta}\right) \tag{3.14}$$

$$\hat{u}\frac{\partial \beta_O}{\partial \xi} + \hat{v}\frac{\partial \beta_O}{\partial \eta} = \frac{1}{\alpha_D}\frac{1}{\eta}\frac{\partial}{\partial \eta}\left(\eta \frac{\partial \beta_O}{\partial \eta}\right) \tag{3.15}$$

During the derivation of the above equations, we also adopted the less restrictive Chapman-Rubesin-like approximation that

$$\frac{\tilde{\rho}^2 \widetilde{D}_F \tilde{r}}{\int_0^{\tilde{r}} \tilde{\rho} dr'} = C(\xi) \tag{3.16}$$

is independent of the coordinate η. Accordingly, the boundary conditions BCs (1')-(4') become

BC(i) at $\eta = 0$,

$$\frac{\partial \beta_F}{\partial \eta} = \frac{\partial \beta_O}{\partial \eta} = 0$$

BC(ii) at $\eta \to \infty$,

$$\frac{\partial \beta_F}{\partial \eta} = \frac{\partial \beta_O}{\partial \eta} = 0$$

BC(iiia) at $\xi = 0$ and $\eta \leq 1$,

$$\beta_F = \tilde{Y}_{F0} + \tilde{T}_0, \qquad \beta_O = \tilde{T}_0$$

BC(iiib) at $\xi = 0$ and $\eta > 1$,

$$\beta_F = \tilde{T}_\infty, \qquad \beta_O = \tilde{T}_\infty + \tilde{Y}_{O\infty}$$

The mixed boundary condition BC(3a') is replaced by the Dirichlet boundary condition BC(iiia) for mathematical convenience without losing the physics because

the determination of the fuel vapor concentration Y_{F0} requires BC(3a'). The physical interpretation to such boundary condition transformation has been discussed in detail in Chapter II, thus will not be repeated in this chapter.

3.3 Power-law vortex model

In Chuah *et al.*'s theory, the vortical flow was assumed to be a Burgers vortex, whose stream function contains a second-order power function of the radial coordinate, namely, Equation (3) with $\alpha_v = 2$ [13]. To characterize the strong vortical flow of firewhirls, Klimenko and Williams adopted a power-law vortex model expressed in Equation (3.3) with $1 < \alpha_v < 2$ and further introduced a Burgers vortex core to eliminate the velocity singularity at the axis. To generalize these models, we assume that the stream function of the vortical flow can be described by a piecewise power-law vortex model in the $\xi - \eta$ space as

$$\psi = \begin{cases} s(\xi)\eta^{\alpha_{v1}}, & \eta < \eta_c \\ \eta_c^{\alpha_{v1}-\alpha_{v2}} s(\xi)\eta^{\alpha_{v2}}, & \eta \geq \eta_c \end{cases} \tag{3.17}$$

and the resulting velocity components are given by

$$\hat{u} = \begin{cases} \alpha_{v1}\eta^{\alpha_{v1}-2} s(\xi), & \eta < \eta_c \\ \alpha_{v2}\eta_c^{\alpha_{v1}-\alpha_{v2}} s(\xi)\eta^{\alpha_{v2}-2}, & \eta \geq \eta_c \end{cases} \tag{3.18}$$

$$\hat{v} = \begin{cases} -s'(\xi)\eta^{\alpha_{v1}-1}, & \eta < \eta_c \\ -\eta_c^{\alpha_{v1}-\alpha_{v2}} s'(\xi)\eta^{\alpha_{v2}-1}, & \eta \geq \eta_c \end{cases} \tag{3.19}$$

where η_c is the radius of the vortex core and $s(\xi)$ is subject to other conservation laws and boundary conditions. α_{v1}, the exponent of the power law model in the inner regime, must be larger than or equal to 2 to avoid the velocity singularity at the axis, which does not physically exist in firewhirls. Furthermore, we can make use of $\eta_c \ll 1$, which physically means that the radius of the vortex core is sufficiently smaller than that of the fuel pool.

A few remarks should be given to the present vortex model. By transforming $\hat{u}$ and $\hat{v}$ back to the physical coordinates, we can have the velocity field satisfying the continuity equation, indicating that the power-law vortex in the $\xi - \eta$ space is physically realistic. The detailed derivations are presented in Appendix B. In the vortex models of the present study and Klimenko and Williams [35], a discontinuity of the axial velocity exists at the edge of the vortex core. The discontinuity can however be readily eliminated by adding higher order correction term of $O(\eta^{\alpha_{v1}+1})$ to the inner part of the stream function. Because the term decreases at least cubically (as $\alpha_{v1} \geq 2$) with the radius of vortex core, neglecting the discontinuity does not cause any significant influence on the flame height. Furthermore, it is noted that the exponents in the stream function may slightly change with density variation. Nevertheless, the circulation-controlled firewhirls addressed in the present study presumes that the vortical flow field is so strong that it is unlikely to be substantially affected by the

density variation, and that the functional form of the vortex model should remain as the power-law functional forms suggested by Klimenko and Williams [35].

3.4 Stream function coordinates

In order to facilitate analytical solutions of Equations (3.14) and (3.15) subject to the boundary conditions of BC(i), BC(ii) and BC(iii), we introduce the stream function coordinates, defined by

$$\chi = \frac{\alpha_v}{2}\xi, \qquad \zeta = \sqrt{2\psi} \tag{3.20}$$

where α_v can be regarded as an overall exponent characterizing the generalized power-law vortex, and can be determined in terms of α_{v1} and α_{v2}, which will be discussed in the section of similarity solution. Similar transformation in the dimensional form were adopted by Klimenko and Williams [35]. Applying Equation (3.20) to Equations (3.14) and (3.15), we have

$$\frac{\partial \beta_F}{\partial \chi} = \frac{1}{\zeta}\frac{\partial}{\partial \zeta}\left(\zeta \frac{\partial \beta_F}{\partial \zeta}\right) \tag{3.21}$$

$$\frac{\partial \beta_O}{\partial \chi} = \frac{1}{\alpha_D}\frac{1}{\zeta}\frac{\partial}{\partial \zeta}\left(\zeta \frac{\partial \beta_O}{\partial \zeta}\right) \tag{3.22}$$

Accordingly, the boundary conditions in the stream function coordinates are given by

BC(I) at $\zeta = 0$

$$\frac{\partial \beta_F}{\partial \zeta} = \frac{\partial \beta_O}{\partial \zeta} = 0$$

BC(II) at $\zeta \to \infty$

$$\frac{\partial \beta_F}{\partial \zeta} = \frac{\partial \beta_O}{\partial \zeta} = 0$$

BC(III-a) at $\chi = 0$ and $\zeta \leq 1$

$$\beta_F = \tilde{Y}_{F0} + \tilde{T}_0, \qquad \beta_O = \tilde{T}_0$$

BC(III-b) at $\chi = 0$ and $\zeta > 1$

$$\beta_F = \tilde{T}_\infty, \qquad \beta_O = \tilde{T}_\infty + \tilde{Y}_{O\infty}$$

Equation (3.21) and (3.22) together with BCs (I)-(III) formulate an analytically solvable PDE system describing the firewhirls.

3.5 Approximate matching solutions of coupling functions

Similar to Equations (3.4) and (3.5), Equations (3.21) and (3.22) are rigorously valid on the fuel and oxidizer sides of the flame sheet, and are approximate on the other side. The exact solution must be obtained by means of matching at the flame sheet location, as we have discussed in the preceding section. Considering that the rigorous matching of the solutions of Equations (3.21) and (3.22) is analytically impossible, recognizing that the two equations are linear and almost identical (except the factor $1/\alpha_D$), and noting that the far-field and axisymmetric boundary conditions are formally

valid for β_F and β_O, we constructed the approximate matching solutions in the form of

$$\beta_F(\chi,\zeta) = \beta_F^{(0)}(\chi,\zeta) + c_F(\chi,\zeta)\beta_F^{(1)}(\chi,\zeta) \tag{3.23}$$

$$\beta_O(\chi,\zeta) = \beta_O^{(0)}(\chi,\zeta) - c_O(\chi,\zeta)\beta_O^{(1)}(\chi,\zeta) \tag{3.24}$$

where

$$\beta_F^{(0)} = \tilde{T}_\infty + \left(\tilde{Y}_{F0} + \tilde{T}_0 - \tilde{T}_\infty\right)\int_0^\infty J_0(\omega\zeta)J_1(\omega)\exp(-\omega^2\chi)\,d\omega \tag{3.25}$$

$$\begin{aligned}\beta_O^{(0)} = {} & \tilde{T}_\infty + \tilde{Y}_{O\infty} \\ & + \left(\tilde{T}_0 - \tilde{T}_\infty - \tilde{Y}_{O\infty}\right)\int_0^\infty J_0(\omega\zeta)J_1(\omega)\exp\left(-\frac{\omega^2}{\alpha_D}\chi\right)d\omega\end{aligned} \tag{3.26}$$

are the leading order solutions obtained by formally extending Equations (3.21) and (3.22) to the entire flow field, and

$$\begin{aligned}\beta_F^{(1)} = {} & \left(\tilde{Y}_{F0} + \tilde{T}_0 - \tilde{T}_\infty\right) \\ & \times \int_0^\infty J_0(\omega\zeta)J_1(\omega)\left[\exp\left(-\frac{\omega^2}{\alpha_D}\chi\right)\right. \\ & \left. - \exp(-\omega^2\chi)\right]d\omega\end{aligned} \tag{3.27}$$

$$\begin{aligned}\beta_O^{(1)} = {} & \left(\tilde{T}_0 - \tilde{T}_\infty - \tilde{Y}_{O\infty}\right) \\ & \times \int_0^\infty J_0(\omega\zeta)J_1(\omega)\left[\exp\left(-\frac{\omega^2}{\alpha_D}\chi\right)\right. \\ & \left. - \exp(-\omega^2\chi)\right]d\omega\end{aligned} \tag{3.28}$$

are the first-order corrections due to the factor $1/\alpha_D$. $c_F(\chi,\zeta)$ and $c_O(\chi,\zeta)$ are bounded functions asymptotically satisfying

$$c_F(\chi < \chi_h, 0) = c_O(\chi, \infty) = 0 \tag{3.29}$$

and

$$c_F(\chi, \infty) = c_O(\chi < \chi_h, 0) = 1 \tag{3.30}$$

which are proved in the Appendix C.

3.6 Far-field solutions

In the present power-law vortex model, the ξ-dependence of the stream function is described by $s(\xi)$ according to Equation (3.17). If the function $s(\xi)$ is assumed to be a linear function of ξ, special far-field solutions of β_F and β_O can be found regardless of the functional form of the η-dependence of the stream function, which is not restricted to power functions. Such special far-field solutions can be given by

$$\beta_F = \frac{\tilde{Y}_{F0} + \tilde{T}_0 - \tilde{T}_\infty}{2\xi A} \exp\left(\int_0^\eta \hat{v} d\eta'\right) + \tilde{T}_\infty \tag{3.31}$$

$$\beta_O = \alpha_D \frac{\tilde{T}_0 - \tilde{T}_\infty - \tilde{Y}_{O\infty}}{2\xi A} \exp\left(\alpha_D \int_0^\eta \hat{v} d\eta'\right) + \tilde{T}_\infty + \tilde{Y}_{O\infty} \tag{3.32}$$

where the constant A is defined by

$$A = \frac{1}{\xi}\int_0^{\infty} \hat{u} \exp\left(\int_0^{\eta} \hat{v} d\eta\right) \eta d\eta \tag{3.33}$$

The solutions (3.31) and (3.32) exactly satisfy the governing equations (3.21) and (3.22), respectively, subject to the boundary conditions BC (I) and BC(II), but they do not satisfy the boundary conditions BC(IIIa) and BC(IIIb). This can be regarded as a variant and generalized version of the result obtained by Klimenko and Williams[35], where a far-field solution of mixture fraction in physical coordinates was obtained for constant physical properties. In Equations (3.31) and (3.32), the effects of variable physical properties have been implicitly included in the coordinates η and ξ.

3.7 Flame height equation

The flame height can be determined by equating β_F and β_O from Equations (3.23) and (3.24), setting ζ_f equal to zero, resulting in the implicit expression for χ_h as $\beta_F(\chi_h, 0) = \beta_O(\chi_h, 0)$, which is written in detailed form by

$$
\begin{aligned}
&\left(\tilde{Y}_{F0}+\tilde{T}_0-\tilde{T}_\infty\right)\int_0^\infty J_1(\omega)\exp(-\omega^2\chi_h)\,d\omega \\
&\quad+c_F(\chi_h,0)\left(\tilde{Y}_{F0}+\tilde{T}_0-\tilde{T}_\infty\right) \\
&\quad\times\int_0^\infty J_1(\omega)\left[\exp\left(-\frac{\omega^2}{\alpha_D}\chi_h\right)-\exp(-\omega^2\chi_h)\right]d\omega \\
&\quad=\tilde{Y}_{O\infty} \\
&\quad+\left(\tilde{T}_0-\tilde{T}_\infty-\tilde{Y}_{O\infty}\right)\int_0^\infty J_1(\omega)\exp\left(-\frac{\omega^2}{\alpha_D}\chi_h\right)d\omega \\
&\quad-c_O(\chi_h,0)\left(\tilde{T}_0-\tilde{T}_\infty-\tilde{Y}_{O\infty}\right) \\
&\quad\times\int_0^\infty J_1(\omega)\left[\exp\left(-\frac{\omega^2}{\alpha_D}\chi_h\right)-\exp(-\omega^2\chi_h)\right]d\omega
\end{aligned}
\tag{3.34}
$$

where χ_h refers to the flame height location in $\chi-\zeta$ coordiantes. Evaluating the integrals exactly, we have

$$
\int_0^\infty J_1(\omega)\exp(-\omega^2\chi_h)d\omega=1-\exp\left(-\frac{1}{4\chi_h}\right) \tag{3.35}
$$

$$
\int_0^\infty J_1(\omega)\exp\left(-\frac{\omega^2}{\alpha_D}\chi_h\right)d\omega=1-\exp\left(-\frac{\alpha_D}{4\chi_h}\right) \tag{3.36}
$$

Substituting (3.35) and (3.36) into (3.34) and recalling the result that $4\chi_h\gg 1$ [13, 35, 75], we can expand the above exponential terms in Taylor series, retain the first order correction, and have

$$
\exp\left(-\frac{1}{4\chi_h}\right)\sim 1-\frac{1}{4\chi_h},\qquad \exp\left(-\frac{\alpha_D}{4\chi_h}\right)\sim 1-\frac{\alpha_D}{4\chi_h} \tag{3.37}
$$

Substituting Equation (3.37) into Equation (3.34), we have the flame height expression in the explicit form of

$$\chi_h = \frac{\alpha_D}{4Z_{st}}\left\{1 + \frac{Z_{st}(1-\alpha_D)}{\alpha_D} \times \left[\frac{(1-c_F-c_O)\left(\tilde{T}_0 - \tilde{T}_\infty\right)}{\tilde{Y}_{O\infty}} - (1-c_F)\frac{\tilde{Y}_{F0}}{\tilde{Y}_{O\infty}} + c_O\right]\right\} \tag{3.38}$$

To further simplify Equation (3.39), we can make the following estimation of the order of magnitude for the second term in the bracket. The stoichiometric mixture fraction, Z_{st}, is much smaller than unity for commonly used hydrocarbon fuels [13, 69]. The mass diffusivity ratio α_D is a quantity of order $O(1)$ for the concerned fuels, implying that $(1-\alpha_D)/\alpha_D$ is of order $O(1)$ as well. Moreover, the factor $\left(\tilde{T}_0 + \tilde{Y}_{F0} - \tilde{T}_\infty\right)/\tilde{Y}_{O\infty}$ can be written in the dimensional form by $\left(c_p T_0 + Y_{F0} q_c - c_p T_\infty\right)/Y_{O\infty} q_c$, which can be approximated by $Y_{F0}/Y_{O\infty} \sim O(1)$ because q_c is much larger than either $c_p T_0$ or $c_p T_\infty$. As we have proved in Appendix C,

$$|c_F| \sim O(1) \ll \frac{1}{Z_{st}} \tag{3.39}$$

and

$$|c_O| \sim O(1) \ll \frac{1}{Z_{st}} \tag{3.40}$$

Therefore, we can neglect the second term in the brace of Equation (3.38) and have

$$\chi_h = \frac{\alpha_D}{4Z_{st}} \tag{3.41}$$

To obtain the flame height in physical dimension, we should convert χ_h into its dimensional form. According to Equations (3.21), we have

$$\chi_h = \frac{\alpha_v}{2}\frac{1}{\rho_0^2 u_0 r_0^2}\int_0^{x_h} \rho^2 D_F dx' = \frac{\alpha_v}{2}\frac{T_0^2}{u_0 r_0^2}\int_0^{x_h} \frac{D_F}{T^2}\,dx \tag{3.42}$$

where the isobaric approximation has been adopted because it is well justified in low Mach number flows [40]. Substituting Equation (3.42) to Equation (3.41), we have

$$\int_0^{x_h} T^{\alpha_T - 2} dx = \frac{PeT_0^{\alpha_T - 2} d_0 \alpha_D}{8\alpha_v Z_{st}} \tag{3.43}$$

To derive Equation (3.43), we have considered the temperature-dependence of the mass diffusivity within the flame through the relation

$$D_F = D_{F0}\left(\frac{T}{T_0}\right)^{\alpha_T} \tag{3.44}$$

in which α_T is usually less than 2 [13, 72] and equal to 3/2 in the kinetic theory of gases employing the rigid-sphere model.

To facilitate an explicit and concise mathematical expression for the flame height, we denoted the following integral by T_m

$$T_m = \left[\frac{1}{x_h}\int_0^{x_h} T^{\alpha_T - 2} dx\right]^{1/(\alpha_T - 2)} \tag{3.44}$$

which can be treated as a representative temperature in the flame and exactly calculated as in the last chapter, which will not be repeated here. Substituting Eq. (3.44) into Eq. (3.43) we obtain the flame height of firewhirls as

$$\frac{x_h}{d_0} = \alpha_D \frac{2}{\alpha_v} \left(\frac{T_m}{T_0}\right)^{2-\alpha_T} \frac{Pe}{16 Z_{st}} \tag{3.45}$$

in which the effect of variable density and mass diffusivity are represented by the factor of $(T_m/T_0)^{2-\alpha_T}$, identical to that in Chapter II; the effect of strong vortex model is reflected in the factor $2/\alpha_v$, which is formally the same as that obtained by Klimenko and Williams' [35], but the determination of α_v is slightly different and will be discussed shortly in following subsection; the newly identified effect of distinct mass diffusivities for fuel and oxidizer, represented by the factor α_D, will be discussed in detail in Section 3.8.

3.8 Determination of α_v

To obtain an analytical form for the overall exponent α_v in Equation (3.45), we first recall that the flame height is determined by the farthermost axial location where both fuel and oxidizer vanish on the flame sheet. Because the axial location is sufficiently far away from the fuel pool, namely the flame height is substantially larger than the radius of the pool, the fuel and oxidizer profiles around the flame top can be described by their far-field solutions. Consequently, we can apply the alternative

method, which was first proposed by Klimenko and Williams [35], to determine the flame height by making use of the far-field solutions of coupling functions (3.31) and (3.32). By equating the Eq. (3.31) to Eq. (3.32), we have

$$\xi_h = \frac{\alpha_D}{2AZ_{st}}\left[1 + Z_{st}\frac{(1-\alpha_D)}{\alpha_D}\frac{\left(\tilde{T}_0 + \tilde{Y}_{F0} - \tilde{T}_\infty\right)}{\tilde{Y}_{O\infty}}\right] \tag{3.46}$$

Using the same arguments on deriving Equation (3.38) from (3.41), Equation (3.46) can be simplified to

$$\xi_h = \frac{\alpha_D}{2AZ_{st}} \tag{3.47}$$

Rewriting Equation (3.47) in physical coordinates by using transformation (3.7), we have the alternative expression of the flame height based on the far-field solutions as

$$\frac{x_h}{d_0} = \alpha_D \frac{2}{A}\left(\frac{T_m}{T_0}\right)^{2-\alpha_T}\frac{Pe}{16Z_{st}} \tag{3.48}$$

Comparing Equation (3.48) with Equation (3.45), we can conclude that the overall exponent α_v should be the same as the integral factor A:

$$\alpha_v = A = \frac{1}{\xi}\int_0^\infty \hat{u}\exp\left(\int_0^\eta \hat{v}d\eta\right)\eta d\eta \tag{3.49}$$

By substituting the axial and radial velocity profiles given by Equation (3.18) in the above equation and assuming $s(\xi)$ as a linear function of ξ, we thus obtain an explicit expression for α_v as

$$\alpha_v = \alpha_{v1} - (\alpha_{v1} - \alpha_{v2}) \exp\left(-\frac{\eta_c^{\alpha_{v1}}}{\alpha_{v1}}\right) \tag{3.50}$$

It is seen that α_v relies on the radius of the vortex core as such it is equal to α_{v2} in the limiting case of $\eta_c \to 0$ and to α_{v1} in the opposite limiting case of $\eta_c \to \infty$. Because there is lack of velocity measurement of firewhirl in Chuah *et al.*'s experiment, it is impossible for the present study to further determine the precise value of α_v from Equation (3.53). As a result, α_v will be treated as a fitting parameter within the range of 1.33 to 1.43, suggested by Klimenko and Williams[35]. It should be also noted that Equation (3.53) is a generalization to the result obtained by Klimenko and Williams [35] because the assumptions of constant density and mass diffusivity are removed in the present study and because the inner regime is not restricted to the Burgers vortex.

3.9 "Enhancement" and "reduction" mechanism of flame height

The expression for the flame height features a linear relation between the diameter-scaled flame height, x_h/d_0 and the modified Peclet number, $Pe/(16Z_{st})$; the gradient of the linearity is affected by the three multiplicative factors, namely, $(T_m/T_0)^{2-\alpha_T}$, $2/\alpha_v$ and α_D. The physical significance of each factor will be discussed in detail as follows.

The factor $(T_m/T_0)^{2-\alpha_T}$ characterizes the effect of variable density and mass diffusivity on the flame height, and has been identified and thoroughly discussed in the recent study of Yu and Zhang [75]. In summary, $(T_m/T_0)^{2-\alpha_T}$ provides an "enhancement" mechanism to the flame height because it is always larger than unity. Specifically, the representative temperature T_m, defined by Equation (34), is always larger than T_0, and the exponent α_T of a power-law function characterizing the temperature dependence of mass diffusivity is always smaller than 2 (for example, $\alpha_T = 1.5$ according to the kinetic theory employing the rigid sphere model and $\alpha_T = 1.8$ as suggested by Chuah *et al*. [13]). The enhancement mechanism of the variable density and mass diffusivity can be physically interpreted by that the flow density decreases with increasing the flow temperature, that the flow with reduced density becomes more readily to be advected to larger height, leading to that the flame height tends to increase. For illustration, Figure 3.1 shows the ethanol flame contours, as an example, in the stream function coordinates (χ, ζ), the density-mass diffusivity-weighted coordinates (ξ, η), and the physical coordinates (x, r). The flame contour calculated by ignoring the density variation is also shown for comparison. It is seen that the variable density tends to expand the flame contour in both radial and axial directions without significantly changing their shape, leading to an increase of flame height [75].

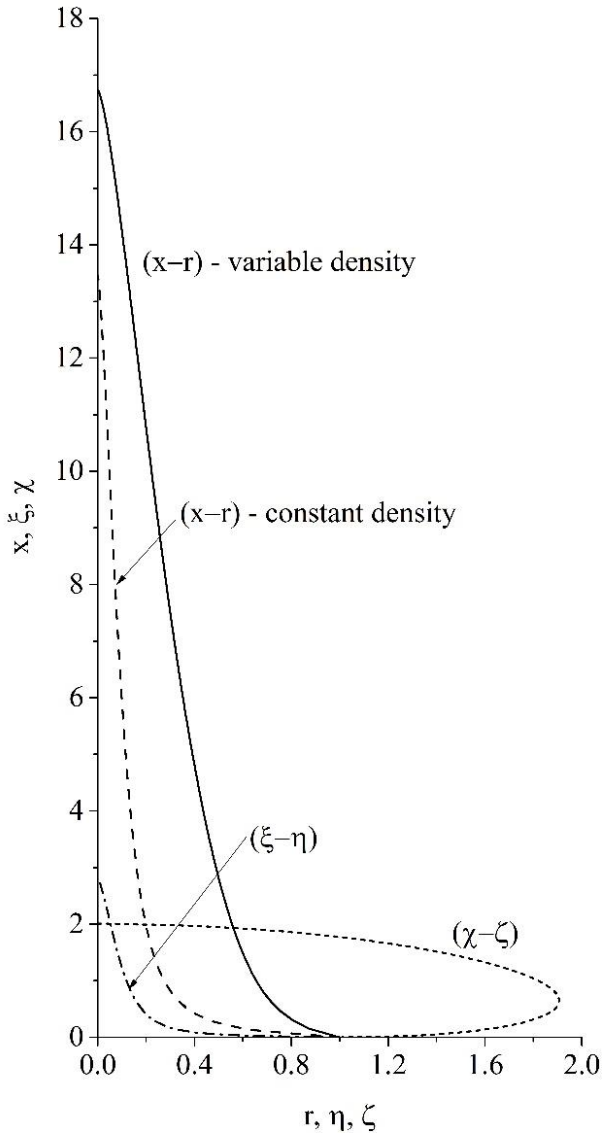

Figure 3.1 Ethanol firewhirl contours in various coordinates.

The factor $2/\alpha_v$, which is formally identical to the correction factor identified by Klimenko and Williams [35], characterizes another "enhancement" mechanism for the flame height because the power-law strong vortex ($\alpha_v < 2$) generates more rapid axial flow near the axis, leading to more intensive axial stretching than the Burgers vortex ($\alpha_v = 2$). In consequence, the flame top is risen to a larger height by a factor of $2/\alpha_v$. It should be noted that the parameter α_v differs from either α_{v1} in the vortex core or

α_{v2} in the outer regime. It is physically improper to adopt a constant exponent $\alpha_v \neq 2$ for the entire flow field without either causing a singularity of axial velocity at the axis or violating the boundary condition at the radial infinity. The mathematical representative of the combining effects of both exponents is the overall exponent α_v, whose analytical expression is given by Equation (3.50). Following Klimenko and Williams' approach [35], α_v will be treated as a fitting parameter in the present study because its precise determination is impossible due to the insufficient experimental observations on the vortical flow field in firewhirls. To facilitate the comparison with Klimenko and Williams' study, we shall use $\alpha_v = 1.33$ and $\alpha_v = 1.43$ recommended in their study [35].

The factor α_D characterizes the effect of distinct mass diffusivities of fuel and oxidizer, which can lead to a substantial reduction of the flame height, as will be shown shortly. The underlying physics is that the mass diffusivities of common liquid hydrocarbons are smaller than that of oxygen in air, because the binary mass diffusivity decreases with increasing the molecular weight of the concerned species according to the Chapman-Enskog theory [19]. The ratio of fuel mass diffusivity to oxidizer mass diffusivity depends on the fuel type and we have $\alpha_D = 0.85$ for methanol, $\alpha_D = 0.70$ for ethanol, and $\alpha_D = 0.52$ for 2-propanol [19]. Consequently, the required higher gradient of fuel mass fraction within the firewhirl flame causes the flame contour to move inside to the fuel side and therefore lead to the reduction of flame height.

Equation (3.45) is the expression for the flame heights of firewhirls, which can degenerate to that of Chuah *et al.* [13] in the case of $\alpha_v = 2$, $\alpha_T = 2$ and $\alpha_D = 1$, to that of Klimenko and Williams [35] in the case of $\alpha_T = 2$ and $\alpha_D = 1$, and to that of Yu and Zhang [75] in the case of $\alpha_v = 2$ and $\alpha_D = 1$.

To illustrate the comparison between different theories with experimental results, Figure 3.2 shows the theoretical predictions by Equation (3.45) with different combinations of α_v and α_T. In each subplot for a combination of α_v and α_T, the mass diffusivity ratio α_D varies according to the fuel types adopted in Chuah *et al.*'s study [13].

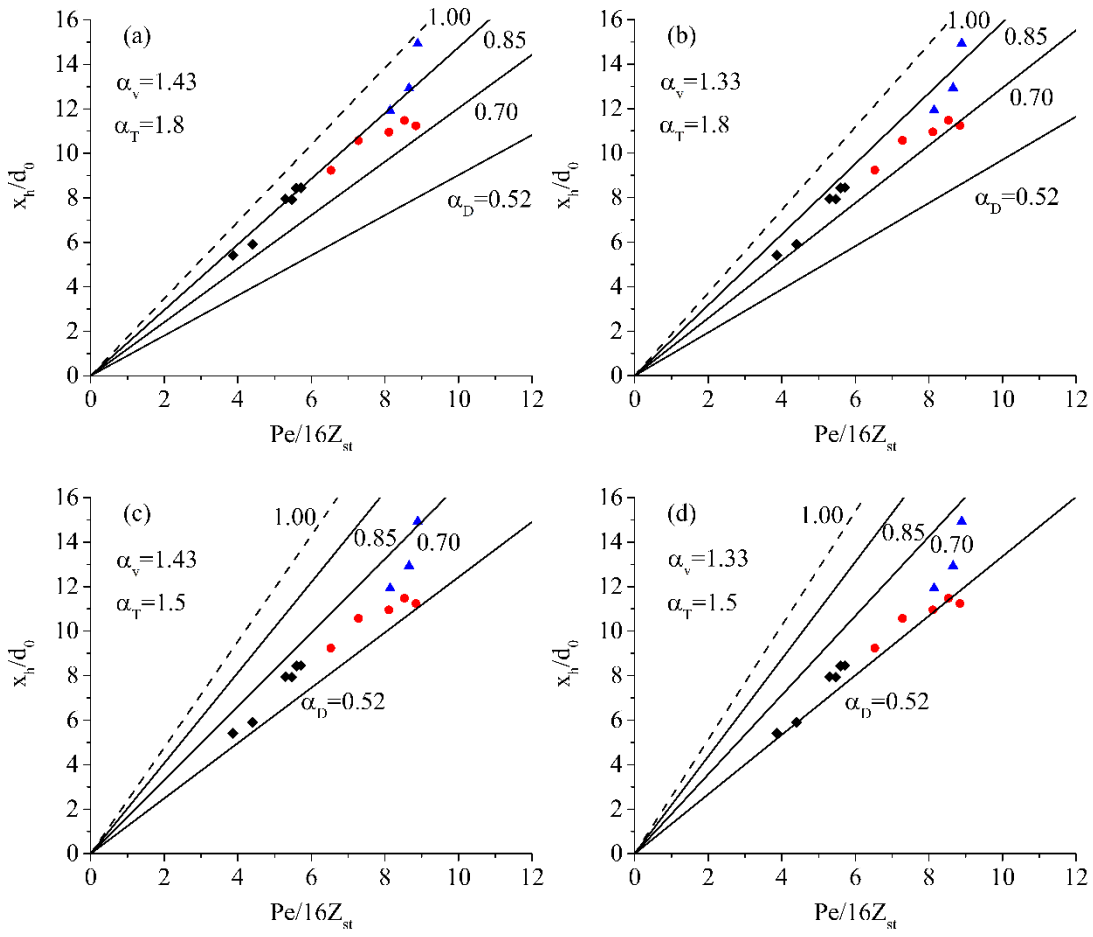

Figure 3.2 Diameter-scaled flame height plotted against modified Peclet number. Solid symbols represent experimental data from Chuah *et al.* [5] for various alcohols: methanol (♦), ethanol (●) and 2-propanol (▲). The lines represent the theoretical predictions with various ratios of mass diffusivities of fuel and oxidizer.

First, we discuss about the situation of $\alpha_D = 1$, which is represented by the dashed line in each subplot. It is seen that x_h/d_0 tends to increase with decreasing either α_v or α_T or both. Within the physically realistic ranges of α_v and α_T, namely, $1.33 \leq \alpha_v \leq 1.43$ and $1.5 \leq \alpha_T \leq 1.8$, the theoretical predictions always overshoot the experimental data. This means that the combined "enhancement" mechanisms due to the strong power-law vortex and variable physical properties produce a considerable overestimation to the flame height, which must be counteracted by some "reduction" mechanism.

The "reduction" mechanism owing to $\alpha_D < 1$ generates anew good theoretical predictions of flame height, presented as the solid lines in each subfigure of Figure 3, with the experimental data. The degree of the "reduction" depends on the fuel types so that it is more substantial for burning 2-propanol than for burning methanol. The discrepancy may be attributed to that the flame temperature of propanol firewhirl is higher than that of the other two alcohols and using a higher propanol flame temperature can improve the theoretical predictions, as already pointed out by Yu and Zhang [75]. In the present calculations, the flame temperature for all liquid fuels is set as 1300K as

suggested by Chua *et al.* [13] and further analysis of the propanol firewhirls is impossible without more details and uncertainty quantification about the experiments.

Chapter IV Non-unity Lewis number effects

4.1 Governing equations

Unlike the previous studies, the fuel and oxidizer Lewis numbers Le_F and Le_O are not restricted to be unity. Adopting the formulation by Chung and Law[15], the governing equations for fuel and oxidizer fractions can be combined to eliminate the chemical reaction terms in each of them, giving

$$\left(\tilde{\rho}\tilde{u}\frac{\partial}{\partial\tilde{x}}+\tilde{\rho}\tilde{v}\frac{\partial}{\partial\tilde{r}}\right)\left(\tilde{Y}_F-\tilde{Y}_O\right)-\frac{2Le_F}{Pe}\frac{\partial}{\partial\tilde{x}}\left[\tilde{\rho}\widetilde{D}_F\frac{\partial}{\partial\tilde{x}}\left(\frac{\tilde{Y}_F}{Le_F}-\frac{\tilde{Y}_O}{Le_O}\right)\right] - \frac{2Le_F}{Pe}\frac{1}{\tilde{r}}\frac{\partial}{\partial\tilde{r}}\left[\tilde{\rho}\widetilde{D}_F\tilde{r}\frac{\partial}{\partial\tilde{r}}\left(\frac{\tilde{Y}_F}{Le_F}-\frac{\tilde{Y}_O}{Le_O}\right)\right]=0 \tag{4.1}$$

In a similar approach, combining the governing equations for fuel mass fraction and enthalpy yields

$$\left(\tilde{\rho}\tilde{u}\frac{\partial}{\partial\tilde{x}}+\tilde{\rho}\tilde{v}\frac{\partial}{\partial\tilde{r}}\right)\left(\tilde{Y}_F+\tilde{T}\right)-\frac{2Le_F}{Pe}\frac{\partial}{\partial\tilde{x}}\left[\tilde{\rho}\widetilde{D}_F\frac{\partial}{\partial\tilde{x}}\left(\frac{\tilde{Y}_F}{Le_F}+\tilde{T}\right)\right] - \frac{2Le_F}{Pe}\frac{1}{\tilde{r}}\frac{\partial}{\partial\tilde{r}}\left[\tilde{\rho}\widetilde{D}_F\tilde{r}\frac{\partial}{\partial\tilde{r}}\left(\frac{\tilde{Y}_F}{Le_F}+\tilde{T}\right)\right]=0 \tag{4.2}$$

In the particular case of unity Lewis numbers, i.e., $Le_F = Le_O = 1$, equations (4.1) and (4.2) reduced to the conservation equations for the conventional species-species coupling function defined by $\tilde{Y}_F - \tilde{Y}_O$ and species-enthalpy coupling function defined by $\tilde{Y}_F + \tilde{T}$, respectively.

The nondimensional boundary conditions to equations (4.1) and (4.2) are given by

BC(1) at $\tilde{r} = 0$

$$\frac{\partial \tilde{Y}_F}{\partial \tilde{r}} = \frac{\partial \tilde{Y}_O}{\partial \tilde{r}} = \frac{\partial \tilde{T}}{\partial \tilde{r}} = 0$$

BC(2) at $\tilde{r} \to \infty$

$$\frac{\partial \tilde{Y}_F}{\partial \tilde{r}} = \frac{\partial \tilde{Y}_O}{\partial \tilde{r}} = \frac{\partial \tilde{T}}{\partial \tilde{r}} = 0$$

BC(3a) at $\tilde{x} = 0$ and $\tilde{r} \leq 1$

$$\tilde{Y}_F = \tilde{Y}_{F0}, \qquad \tilde{Y}_O = 0, \qquad \tilde{T} = \tilde{T}_0$$

BC(3b) at $\tilde{x} = 0$ and $\tilde{r} > 1$

$$\frac{\partial \tilde{Y}_F}{\partial \tilde{x}} = \frac{\partial \tilde{Y}_O}{\partial \tilde{x}} = \frac{\partial \tilde{T}}{\partial \tilde{x}} = 0$$

BC(4) at $\tilde{x} \to \infty$

$$\tilde{Y}_F = 0, \qquad \tilde{Y}_O = \tilde{Y}_{O,\infty}, \qquad \tilde{T} = \tilde{T}_\infty$$

BC(1) and BC(2) are the axisymmetric and radial far field conditions, respectively. The unspecified quantities in BC(3a), $\tilde{Y}_{F0}$ and $\tilde{T}_0$ should be determined by analyzing the Stefan flow within the evaporation layer, which has been discussed in detail in the

closure problem section in Chapter II, thus would not be repeated here. BC(3b) specifies the non-vaporizing surface outside fuel pool. BC(4) indicates that there is no fuel on the oxidizer side of the flame, a result from the flame sheet assumption.

4.2 Coordinate transformation

Introducing a density-mass-diffusivity-weighted coordinate system defined in terms of $\tilde{x}$ and $\tilde{r}$ in integral form as

$$\xi = \frac{D_{F0}}{u_0 r_0}\int_0^{\tilde{x}} \tilde{\rho}^2 \widetilde{D}_F dx' = \frac{2}{Pe}\int_0^{\tilde{x}} \tilde{\rho}^2 \widetilde{D}_F dx', \qquad \eta = \int_0^{\tilde{r}} \tilde{\rho} dr' \tag{4.3}$$

and writing equations (4.1) and (4.2) in ξ and η coordinates, we obtain

$$\begin{aligned}
&\left(\hat{u}\frac{\partial}{\partial\xi} + \hat{v}\frac{\partial}{\partial\eta}\right)\left(\tilde{Y}_F + \tilde{T}\right) \\
&\quad - \frac{4Le_F}{Pe^2\tilde{\rho}}\left(\frac{\partial}{\partial\xi} + h\frac{\partial}{\partial\eta}\right)\left[\tilde{\rho}^3\widetilde{D}_F^2\left(\frac{\partial}{\partial\xi} + h\frac{\partial}{\partial\eta}\right)\right]\left(\frac{\tilde{Y}_F}{Le_F} + \tilde{T}\right) \\
&\quad - Le_F\left(\frac{2g}{Pe\tilde{\rho}\tilde{r}}\frac{\partial}{\partial\xi} + \frac{1}{\tilde{\rho}^2\widetilde{D}_F\tilde{r}}\frac{\partial}{\partial\eta}\right) \\
&\quad \times\left(\frac{2\tilde{\rho}^3\widetilde{D}_F^2 g\tilde{r}}{Pe}\frac{\partial}{\partial\xi} + \tilde{\rho}^2\widetilde{D}_F\tilde{r}\frac{\partial}{\partial\eta}\right)\left(\frac{\tilde{Y}_F}{Le_F} + \tilde{T}\right) = 0
\end{aligned} \tag{4.4}$$

$$\left(\hat{u}\frac{\partial}{\partial\xi}+\hat{v}\frac{\partial}{\partial\eta}\right)\left(\tilde{Y}_F-\tilde{Y}_O\right)$$
$$-\frac{4Le_F}{Pe^2\tilde{\rho}}\left(\frac{\partial}{\partial\xi}+h\frac{\partial}{\partial\eta}\right)\left[\tilde{\rho}^3\tilde{D}_F^2\left(\frac{\partial}{\partial\xi}+h\frac{\partial}{\partial\eta}\right)\right]\left(\frac{\tilde{Y}_F}{Le_F}-\frac{\tilde{Y}_O}{Le_O}\right)$$
$$-Le_F\left(\frac{2g}{Pe\tilde{\rho}\tilde{r}}\frac{\partial}{\partial\xi}+\frac{1}{\tilde{\rho}^2\tilde{D}_F\tilde{r}}\frac{\partial}{\partial\eta}\right) \tag{4.5}$$
$$\times\left(\frac{2\tilde{\rho}^3\tilde{D}_F^2 g\tilde{r}}{Pe}\frac{\partial}{\partial\xi}+\tilde{\rho}^2\tilde{D}_F\tilde{r}\frac{\partial}{\partial\eta}\right)\left(\frac{\tilde{Y}_F}{Le_F}-\frac{\tilde{Y}_O}{Le_O}\right)=0$$

where we have defined two functions g and h in the forms of

$$g(\tilde{x},\tilde{r})=\frac{1}{\tilde{\rho}^2\tilde{D}_F}\int_0^{\tilde{x}}\frac{\partial}{\partial\tilde{r}}\left(\tilde{\rho}^2\tilde{D}_F\right)dx' \tag{4.6a}$$

$$h(\tilde{x},\tilde{r})=\frac{Pe}{2\tilde{\rho}^2\tilde{D}_F}\int_0^{\tilde{r}}\frac{\partial\tilde{\rho}}{\partial\tilde{x}}dr' \tag{4.6b}$$

to account for the variations of density and mass diffusivity gradients in axial and radial directions, in terms of which, the non-dimensional velocity components in equation (4.4) and (4.5) should be defined as

$$\hat{u}=2\tilde{u}+2g\tilde{v} \tag{4.7a}$$

$$\hat{v}=2h\tilde{u}+\frac{Pe}{\tilde{\rho}\tilde{D}_F}\tilde{v} \tag{4.7b}$$

which is fully consistent with the results in Chapter II and Chapter III. In correspondence, the boundary conditions BCs (1)-(4) are transformed to

BC(1') at $\eta=0$

$$\frac{\partial \tilde{Y}_F}{\partial \eta} = \frac{\partial \tilde{Y}_O}{\partial \eta} = \frac{\partial \tilde{T}}{\partial \eta} = 0$$

BC(2') at $\eta \to \infty$

$$\frac{\partial \tilde{Y}_F}{\partial \eta} = \frac{\partial \tilde{Y}_O}{\partial \eta} = \frac{\partial \tilde{T}}{\partial \eta} = 0$$

BC(3a') at $\xi = 0$ and $\eta \leq 1$

$$\tilde{Y}_F = \tilde{Y}_{F0}, \qquad \tilde{T} = \tilde{T}_0, \qquad \tilde{Y}_O = 0$$

BC(3b') at $\xi = 0$ and $\eta > 1$

$$\frac{\partial \tilde{Y}_F}{\partial \xi} = \frac{\partial \tilde{T}}{\partial \xi} = \frac{\partial \tilde{Y}_O}{\partial \xi} = 0$$

BC(4') at $\xi \to \infty$

$$\tilde{Y}_F = 0, \qquad \tilde{Y}_O = \tilde{Y}_{O,\infty}, \qquad \tilde{T} = \tilde{T}_\infty$$

As far as concerning the circulation-controlled firewhirls, we can adopt the large Peclet number approximation, i.e., $Pe \gg 1$, to simplify the above equations. In the meanwhile, as stated in Chapter II and Chapter III, the nondimensional velocities $\hat{u}$ and $\hat{v}$ in the $\xi - \eta$ space should be in the same order of magnitude. As a consequence, we can deduce from equation (4.6) that $h \sim O(1)$, $g \sim O(1)$, $\tilde{u} \sim O(1)$, and $\tilde{v} \sim O(1/Pe)$, the detail procedure has been discussed in Chapter II and would not be repeated here.

Based on the above considerations, we can neglect all terms containing $1/Pe$ and $1/Pe^2$ in equations (4.4) and (4.5), giving

$$\left(\hat{u}\frac{\partial}{\partial\xi}+\hat{v}\frac{\partial}{\partial\eta}\right)\left(\tilde{Y}_F+\tilde{T}\right)=Le_F\frac{1}{\eta}\frac{\partial}{\partial\eta}\left[\eta\frac{\partial}{\partial\eta}\left(\frac{\tilde{Y}_F}{Le_F}+\tilde{T}\right)\right] \tag{4.8}$$

$$\left(\hat{u}\frac{\partial}{\partial\xi}+\hat{v}\frac{\partial}{\partial\eta}\right)\left(\tilde{Y}_F-\tilde{Y}_O\right)=Le_F\frac{1}{\eta}\frac{\partial}{\partial\eta}\left[\eta\frac{\partial}{\partial\eta}\left(\frac{\tilde{Y}_F}{Le_F}-\frac{\tilde{Y}_O}{Le_O}\right)\right] \tag{4.9}$$

To derive equations (4.8) and (4.9), we have invoked an approximation that

$$\frac{\tilde{\rho}^2\tilde{D}_F\tilde{r}}{\int_0^{\tilde{r}}\tilde{\rho}dr'}=C(\xi) \tag{4.10}$$

is independent of the coordinate η, which is weak version of the Chapman-Rubesin approximation[59], which further assumes $C(\xi)$ being a global constant. In accordance, the boundary conditions BC(1')-BC(4') become

BC(I) at $\eta=0$

$$\frac{\partial\tilde{Y}_F}{\partial\eta}=\frac{\partial\tilde{Y}_O}{\partial\eta}=\frac{\partial\tilde{T}}{\partial\eta}=0$$

BC(II) at $\eta\to\infty$

$$\frac{\partial\tilde{Y}_F}{\partial\eta}=\frac{\partial\tilde{Y}_O}{\partial\eta}=\frac{\partial\tilde{T}}{\partial\eta}=0$$

BC(III-a) at $\xi=0$ and $\eta\leq1$

$$\tilde{Y}_F=\tilde{Y}_{F0},\qquad\tilde{T}=\tilde{T}_0,\qquad\tilde{Y}_O=0$$

BC(III-b) at $\xi=0$ and $\eta>1$

$$\tilde{Y}_F=0,\qquad\tilde{T}=\tilde{T}_\infty,\qquad\tilde{Y}_O=\tilde{Y}_{O,\infty}$$

In Chuah et al.'s theory, the vortical flow was described by a Burgers vortex, whose stream function contains a second order power function of the radial coordinate. To characterizing the strong vortical flow of firewhirl, Klimenko and Williams proposed a power-law vortex containing a Burgers vortex core to eliminate the velocity singularity at the axis. In Chapter III, we have adopted a piecewise power-law vortex model in the $\xi-\eta$ space with two exponents, namely, α_{v2} accounting for the deviation of the vortical flow from Burgers vortex in the far field, and α_{v1} characterizing the flow within the vortex core. By transforming $\hat{u}$ and $\hat{v}$ back to the physical coordinates, we can have the velocity field satisfying the continuity equation[74], indicating that the power-law vortex in the ξ-η space is physically realistic. In this chapter, we retain the piecewise generalized power-law vortex model as in Chapter III, and write its stream function in the form of

$$\psi = \begin{cases} s(\xi)\eta^{\alpha_{v1}}, & \eta < \eta_c \\ \eta_c^{\alpha_{v1}-\alpha_{v2}} s(\xi)\eta^{\alpha_{v2}}, & \eta \geq \eta_c \end{cases} \tag{4.11}$$

in terms of which the velocity components can be calculated by

$$\hat{u} = \begin{cases} \alpha_{v1}\eta^{\alpha_{v1}-2} s(\xi), & \eta < \eta_c \\ \alpha_{v2}\eta_c^{\alpha_{v1}-\alpha_{v2}} s(\xi)\eta^{\alpha_{v2}-2}, & \eta \geq \eta_c \end{cases} \tag{4.12a}$$

$$\hat{v} = \begin{cases} -s'(\xi)\eta^{\alpha_{v1}-1}, & \eta < \eta_c \\ -\eta_c^{\alpha_{v1}-\alpha_{v2}} s'(\xi)\eta^{\alpha_{v2}-1}, & \eta \geq \eta_c \end{cases} \tag{4.12b}$$

where η_c is the radius of the vortex core and $s(\xi)$ is subject to other conservation laws and boundary conditions. α_{v1}, the exponent of the power law model in the inner regime, must be greater than or equal to 2 to ensure the regularity of axial velocity.

Furthermore, we can make use of $\eta_c \ll 1$, which physically means that the radius of the vortex core is sufficiently smaller than that of the fuel pool.

To facilitate analytical solutions of equations (4.8) and (4.9) under boundary conditions BC(I) – (III), we introduce the stream function coordinates defined by

$$\chi = \frac{\alpha_v}{2}\xi, \qquad \zeta = \sqrt{2\psi} \tag{4.13}$$

where α_v represents an overall exponential characterizing the generalized-power vortex as that in Chapter III. Applying the coordinate transformation (4.13) to equations (4.8) and (4.9) gives

$$\frac{\partial}{\partial\chi}\left(\tilde{Y}_F + \tilde{T}\right) = Le_F \frac{1}{\zeta}\frac{\partial}{\partial\zeta}\left[\zeta\frac{\partial}{\partial\zeta}\left(\frac{\tilde{Y}_F}{Le_F} + \tilde{T}\right)\right] \tag{4.14}$$

$$\frac{\partial}{\partial\chi}\left(\tilde{Y}_F - \tilde{Y}_O\right) = Le_F \frac{1}{\zeta}\frac{\partial}{\partial\zeta}\left[\zeta\frac{\partial}{\partial\zeta}\left(\frac{\tilde{Y}_F}{Le_F} - \frac{\tilde{Y}_O}{Le_O}\right)\right] \tag{4.15}$$

Accordingly, the boundary conditions in the stream function coordinates are given by

BC(i) at $\zeta = 0$

$$\frac{\partial\tilde{Y}_F}{\partial\zeta} = \frac{\partial\tilde{Y}_O}{\partial\zeta} = \frac{\partial\tilde{T}}{\partial\zeta} = 0$$

BC(ii) at $\zeta \to \infty$

$$\frac{\partial\tilde{Y}_F}{\partial\zeta} = \frac{\partial\tilde{Y}_O}{\partial\zeta} = \frac{\partial\tilde{T}}{\partial\zeta} = 0$$

BC(iii-a) at $\chi = 0$ and $\zeta \leq 1$

$$\tilde{Y}_F = \tilde{Y}_{F0}, \qquad \tilde{T} = \tilde{T}_0, \qquad \tilde{Y}_O = 0$$

BC(iii-b) at $\chi = 0$ and $\zeta > 1$

$$\tilde{Y}_F = 0, \qquad \tilde{T} = \tilde{T}_\infty, \qquad \tilde{Y}_O = \tilde{Y}_{O,\infty}$$

Equations (4.14) and (4.15) with BC(i)-BC(iii) formulate the analytical solvable problem by means of perturbation, which is discussed as follows.

4.3 Perturbation formulation

Due to the mathematical complication of matching solution in dealing with the general situation of non-unity and non-equal Lewis numbers, we consider a particular case of both fuel and oxidizer Lewis numbers being close to unity. In this case the both the fuel and oxidizer mass fractions and the enthalpy can be expanded in asymptotic series regarding the deviations of Lewis numbers from unity as small parameters.

It should be noted that the jump conditions for fuel and oxidizer mass fractions at the flame location with general non-unity Lewis numbers, $Le_F \neq 1$ and $Le_O \neq 1$, should be in the form of[15, 40, 69]

$$\frac{\partial}{\partial n}\left(\frac{\tilde{Y}_F}{Le_F}\right)_{n_f^+} = \frac{\partial}{\partial n}\left(\frac{\tilde{Y}_O}{Le_O}\right)_{n_f^-} \tag{4.16}$$

where $\partial/\partial n$ represents the directional derivative normal to the flame sheet location n_f considered, and the superscript "+" (or "$-$") indicates the derivatives being

evaluated in the fuel (or, oxidizer) inside of the flame contour. The modified species-species and species-enthalpy coupling functions defined in terms of Lewis numbers weighted mass fractions according to (4.16) are continuous both in value and gradient at flame location, whereas the conventional coupling functions become discontinuous in gradient in this case[15]. The modified species-species coupling function is defined by

$$\beta_S = \frac{\tilde{Y}_F}{Le_F} - \frac{\tilde{Y}_O}{Le_O} \tag{4.17}$$

and similarly, the modified species-enthalpy coupling function is defined by

$$\beta_T = \frac{\tilde{Y}_F}{Le_F} + \tilde{T} \tag{4.18}$$

In terms of β_S and β_T defined above, we can rewrite equations (14) and (15) as

$$\frac{\partial \beta_T}{\partial \chi} - Le_F \frac{1}{\zeta}\frac{\partial}{\partial \zeta}\left(\zeta \frac{\partial \beta_T}{\partial \zeta}\right) = -\left(1 - \frac{1}{Le_F}\right)\frac{\partial \tilde{Y}_F}{\partial \chi} \tag{4.19}$$

$$\frac{\partial \beta_S}{\partial \chi} - Le_F \frac{1}{\zeta}\frac{\partial}{\partial \zeta}\left(\zeta \frac{\partial \beta_S}{\partial \zeta}\right) = -\left(1 - \frac{1}{Le_F}\right)\frac{\partial \tilde{Y}_F}{\partial \chi} + \left(1 - \frac{1}{Le_O}\right)\frac{\partial \tilde{Y}_O}{\partial \chi} \tag{4.20}$$

Since we are concerning the fuel and oxidizer Lewis numbers close to unity, we can introduce small quantities in the form of

$$\left(1 - \frac{1}{Le_i}\right) = l_i \quad \text{such that } |l_i| \ll 1, \qquad i = F, O \tag{4.21}$$

Using l_F as the small parameter, we can expand $\tilde{T}$, $\tilde{Y}_F$, and $\tilde{Y}_O$ as

$$\tilde{T} = \tilde{T}^0 + l_F\tilde{T}^1 + \cdots \tag{4.22a}$$

$$\tilde{Y}_F = \tilde{Y}_F^0 + l_F\tilde{Y}_F^1 + \cdots \tag{4.22b}$$

$$\tilde{Y}_O = \tilde{Y}_O^0 + l_F\tilde{Y}_O^1 + \cdots \tag{4.22c}$$

Substituting into equations (4.19) and (4.20) and collecting terms of equal order, we obtain the governing equation with boundary conditions for the leading and first order problems, respectively as

Leading order equation

$$\frac{\partial\beta_T^0}{\partial\chi} - Le_F\frac{1}{\zeta}\frac{\partial}{\partial\zeta}\left(\zeta\frac{\partial\beta_T^0}{\partial\zeta}\right) = 0 \tag{4.23}$$

$$\frac{\partial\beta_S^0}{\partial\chi} - Le_F\frac{1}{\zeta}\frac{\partial}{\partial\zeta}\left(\zeta\frac{\partial\beta_S^0}{\partial\zeta}\right) = 0 \tag{4.24}$$

with boundary conditions

LBC(1) at $\zeta = 0$

$$\frac{\partial\beta_S^0}{\partial\zeta} = \frac{\partial\beta_T^0}{\partial\zeta} = 0$$

LBC(2) at $\zeta \to \infty$

$$\frac{\partial\beta_S^0}{\partial\zeta} = \frac{\partial\beta_T^0}{\partial\zeta} = 0$$

LBC(4-a) at $\chi = 0$ and $\zeta \leq 1$

$$\beta_S^0 = \frac{\tilde{Y}_{F0}}{Le_F}, \qquad \beta_T^0 = \frac{\tilde{Y}_{F0}}{Le_F} + \tilde{T}_0$$

LBC(4-b) at $\chi = 0$ and $\zeta > 1$

$$\beta_S^0 = -\frac{\tilde{Y}_{O,\infty}}{Le_O}, \qquad \beta_T^0 = \tilde{T}_\infty$$

First order equation

$$\frac{\partial \beta_T^1}{\partial \chi} - Le_F \frac{1}{\zeta}\frac{\partial}{\partial \zeta}\left(\zeta \frac{\partial \beta_T^1}{\partial \zeta}\right) = -\frac{\partial \tilde{Y}_F^0}{\partial \chi} \tag{4.25}$$

$$\frac{\partial \beta_S^1}{\partial \chi} - Le_F \frac{1}{\zeta}\frac{\partial}{\partial \zeta}\left(\zeta \frac{\partial \beta_S^1}{\partial \zeta}\right) = -\frac{\partial \tilde{Y}_F^0}{\partial \chi} + \frac{l_O}{l_F}\frac{\partial \tilde{Y}_O^0}{\partial \chi} \tag{4.26}$$

with boundary conditions

FBC(1) at $\zeta = 0$

$$\frac{\partial \beta_S^1}{\partial \zeta} = \frac{\partial \beta_T^1}{\partial \zeta} = 0$$

FBC(2) at $\zeta \to \infty$

$$\frac{\partial \beta_S^1}{\partial \zeta} = \frac{\partial \beta_T^1}{\partial \zeta} = 0$$

FBC(4-a) at $\chi = 0$ and $\zeta \leq 1$

$$\beta_S^1 = 0, \qquad \beta_T^1 = 0$$

FBC(4-b) at $\chi = 0$ and $\zeta > 1$

$$\beta_S^1 = 0, \qquad \beta_T^0 = 0$$

The complete solutions of leading and first orders of modified coupling functions,

$$\beta_S = \beta_S^0 + l_F \beta_S^1$$

and

$$\beta_T = \beta_T^0 + l_F \beta_T^1$$

completely characterize the combustion system, though in asymptotic sense, which will be discussed in the following section.

4.4 Perturbation solution

The solution of the leading order coupling functions β_S^0 and β_T^0 can be obtained by means of separation of variables and utilizing Fourier-Bessel expansion giving

$$\beta_S^0 = -\frac{\tilde{Y}_{O,\infty}}{Le_O} + \left(\frac{\tilde{Y}_{F0}}{Le_F} + \frac{\tilde{Y}_{O,\infty}}{Le_O}\right) \int_0^\infty J_0(\omega\zeta) J_1(\omega) \exp(-Le_F \omega^2 \chi) d\omega \qquad (4.27)$$

$$\beta_T^0 = \tilde{T}_\infty + \left(\frac{\tilde{Y}_{F0}}{Le_F} + \tilde{T}_0 - \tilde{T}_\infty\right) \int_0^\infty J_0(\omega\zeta) J_1(\omega) \exp(-Le_F \omega^2 \chi) d\omega \qquad (4.28)$$

The first order solution of the coupling functions β_S^1 and β_T^1 should be calculated by means of Green's function corresponding to the common differential operator on the left-hand-side (LHS) of equations (4.23) – (4.26), which is denoted by

$$\hat{L}_{\chi,\zeta} = \frac{\partial}{\partial \chi} - Le_F \frac{1}{\zeta} \frac{\partial}{\partial \zeta}\left(\zeta \frac{\partial}{\partial \zeta}\right) \qquad (4.29)$$

The Green's function corresponding to the differential operator $\hat{L}_{\chi,\zeta}$ must satisfy the differential equation with delta functions $\delta(\chi-\chi')\delta(\zeta-\zeta')$ as the inhomogeneous term, i.e.,

$$\hat{L}_{\chi,\zeta}G(\chi,\chi',\zeta,\zeta') = \delta(\chi-\chi')\delta(\zeta-\zeta') \tag{4.30}$$

Integrating equation (40) over the whole domain, i.e., the half-infinite space, denoted by $\mathcal{D}$, it formally yields

$$\int_{\mathcal{D}} \hat{L}_{\chi,\zeta}G(\chi,\chi',\zeta,\zeta')d\mathcal{V} = 1 \tag{4.31}$$

where $d\mathcal{V}$ is the differential element of the domain $\mathcal{D}$. Equation (4.31) implies that the Green's function $G(\chi,\chi',\zeta,\zeta')$ can be regarded as the "inverse" of the operator $\hat{L}_{\chi,\zeta}$, i.e., $G = \hat{L}^{-1}_{\chi,\zeta}$, because the LHS of equation (4.31) can be regarded as an inner product of two operators in Hilbert space[23]. Rewriting equations (4.25) and (4.26) in terms of $\hat{L}_{\chi,\zeta}$, we obtain

$$\hat{L}_{\chi,\zeta}\beta_i^1 = h_i, \qquad i = T,S \tag{4.32}$$

where h_T and h_S refer to the inhomogeneous terms of equations (4.25) and (4.26), respectively. In form, the solution to equation (4.32) can be written as

$$\beta_i^1 = \hat{L}^{-1}_{\chi,\zeta}h_i, \qquad i = T,S \tag{4.33}$$

Substituting the specific definition of h_T and h_S, and regarding the right-hand-side (RHS) of equation (4.33) as the inner product like equation (4.31), we can write the formal solutions of β_T^1 and β_S^1, respectively as

$$\beta_T^1(\chi,\zeta) = -\int_0^\infty d\chi' \int_0^\infty G(\chi,\chi',\zeta,\zeta') \frac{\partial}{\partial \chi'} \tilde{Y}_F^0(\chi',\zeta')\zeta' d\zeta' \tag{4.34}$$

$$\begin{aligned} \beta_S^1(\chi,\zeta) = -\int_0^\infty d\chi' \int_0^\infty & G(\chi,\chi',\zeta,\zeta') \\ & \times \left[\frac{\partial}{\partial \chi'} \tilde{Y}_F^0(\chi',\zeta') - \frac{l_O}{l_F}\frac{\partial}{\partial \chi'} \tilde{Y}_O^0(\chi',\zeta')\right] \zeta' d\zeta' \end{aligned} \tag{4.35}$$

The Green's function $G(\chi,\chi',\zeta,\zeta')$ can be constructed by means of eigenfunction expansion as[23]

$$\begin{aligned} G(\chi,\chi',\zeta,\zeta') = & H(\chi-\chi') \\ & \times \int_0^\infty \omega J_0(\omega\zeta') J_0(\omega\zeta) \exp[-\omega^2 Le_F(\chi-\chi')] d\omega \end{aligned} \tag{4.36}$$

The validity of the Green's function (4.36) can be tested according to the definition that it satisfies equation (4.30). The detail procedures are presented in Appendix D.

The inhomogeneous terms on the RHS of equations (4.25) and (4.26) can be evaluated by recognizing that in the flame sheet formulation the coupling function β_S^0 is equal to either $\tilde{Y}_F^0/Le_F$ or $-\tilde{Y}_O^0/Le_O$, respectively in the fuel or the oxidizer side. After a complex mathematical maneuver, the first order solution of β_S can be calculated, and combining the leading order solutions (4.27) and (4.28), the final form of modified coupling functions can be written as

$$
\begin{aligned}
&\beta_S(\chi,\zeta)\\
&= -\frac{\tilde{Y}_{O,\infty}}{Le_O} + \left(\frac{\tilde{Y}_{F0}}{Le_F} + \frac{\tilde{Y}_{O,\infty}}{Le_O}\right)\int_0^\infty J_0(\omega\zeta)J_1(\omega)\exp(-Le_F\omega^2\chi)d\omega\\
&+ Le_F Le_O\left(\frac{\tilde{Y}_{F0}}{Le_F} + \frac{\tilde{Y}_{O,\infty}}{Le_O}\right)\\
&\times\left\{\frac{l_F\zeta_f^2 H(\chi_f-\chi)}{16Le_O Le_F^2}\int_0^{\chi_f}\frac{1}{(\chi-\chi')\chi'^2}\exp\left[-\frac{\chi+\chi'(\zeta^2-1)}{4Le_F\chi'(\chi-\chi')}\right]d\chi'\right.\\
&+ l_O H(\chi_f-\chi)\int_0^\infty \chi_f\omega^2 J_0(\omega\zeta)J_1(\omega)\exp(-Le_F\omega^2\chi)d\omega\\
&\left.+ l_O\, H(\chi-\chi_f)\int_0^\infty(\chi-\chi_f)\omega^2 J_0(\omega\zeta)J_1(\omega)\exp(-Le_F\omega^2\chi)d\omega\right\}
\end{aligned}
\tag{4.37}
$$

$$
\begin{aligned}
\beta_T(\chi,\zeta) = \tilde{T}_\infty &+ \left(\frac{\tilde{Y}_{F0}}{Le_F} + \tilde{T}_0 - \tilde{T}_\infty\right)\int_0^\infty J_0(\omega\zeta)J_1(\omega)\exp(-Le_F\omega^2\chi)d\omega\\
&+ \frac{l_F}{16Le_F}\left(\frac{\tilde{Y}_{F0}}{Le_F} + \frac{\tilde{Y}_{O,\infty}}{Le_O}\right)\zeta_f^2 H(\chi_f-\chi)\\
&\times\int_0^{\chi_f}\frac{1}{(\chi-\chi')\chi'^2}\exp\left[-\frac{\chi+\chi'(\zeta^2-1)}{4Le_F\chi'(\chi-\chi')}\right]d\chi'
\end{aligned}
\tag{4.38}
$$

The detailed derivation of equations (4.39) and (4.40) has be presented in Appendix E.

4.5 Flame contour

In flame sheet approximation, the both fuel and oxidizer are completely consumed according to stoichiometry, implying the vanishing of β_S in equation (4.37), therefore, the flame contour can be determined in an implicit form

$$\frac{Z_{st}/Le_O}{1-l_F+Z_{st}l_F-Z_{st}l_O} = \int_0^\infty J_0(\omega\zeta_f)J_1(\omega)\exp(-Le_F\omega^2\chi_f)d\omega + \frac{l_F\zeta_f^2}{16Le_F}\int_0^{\chi_f}\frac{1}{(\chi_f-\chi')\chi'^2}\exp\left[-\frac{\chi_f+\chi'(\zeta_f^2-1)}{4Le_F\chi'(\chi_f-\chi')}\right]d\chi' + l_O Le_F Le_O\chi_f\int_0^\infty \omega^2 J_0(\omega\zeta_f)J_1(\omega)\exp(-Le_F\omega^2\chi_f)d\omega \quad (4.39)$$

where we have utilized the definition of stoichiometric mixture fraction in terms of $\tilde{Y}_{F0}$ and $\tilde{Y}_{O,\infty}$ as

$$Z_{st} = \frac{\tilde{Y}_{O,\infty}}{\tilde{Y}_{F0}+\tilde{Y}_{O,\infty}} \quad (4.40)$$

as well as the definitions of small quantities l_F and l_O by equation (4.21).

Closing to the fuel pool surface, $\chi_f \to 0$, the first order corrections in equation (4.39) vanishes, i.e., the flame contour can be determined by leading order solutions of species-species coupling functions alone. In physics, it implies that the non-unity Lewis number has gentle effects on the flame geometry close to the fuel pool, as indicated in Figure 1. The reason is that the flame is anchored to the rim of the fuel pool according to infinite fast reaction rate in flame sheet approximation, thus the flame contour there is determined by the geometry of the fuel pool rather than the physical properties of the combustion system. However, it should be noted that in reality the flame must be detached from the rim of fuel pool due to finiteness of combustion reaction rate[12, 36].

For flame sufficiently remote from the fuel pool, $\chi_f \sim O(1)$ and $\zeta_f \ll 1$, the third term on the RHS of equation (4.39), being proportional to χ_f, becomes much larger than the second term, which is multiplied by $\zeta_f^2/16$ thus can be neglected. Therefore, the first order corrections in the flame contour becomes significant, especially in determining the flame height.

$$\frac{Z_{st}/Le_O}{1-l_F+Z_{st}l_F-Z_{st}l_O} = \int_0^\infty J_0(\omega\zeta_f)J_1(\omega)\exp(-Le_F\omega^2\chi_f)d\omega + l_O Le_F Le_O \chi_f \int_0^\infty \omega^2 J_0(\omega\zeta_f)J_1(\omega)\exp(-Le_F\omega^2\chi_f)d\omega \quad (4.41)$$

In this case an analytically explicit expression for the flame contour can be derived as follows. For large axial flame location, the main contribution to the integrals on the RHS of equation (4.41) are made by ω in the interval near zero point, in the sense of Laplace integration. Thus, we can expand the function $J_1(\omega)$ in Taylor series and retain the first order term, i.e.,

$$J_1(\omega) \sim \frac{1}{2}\omega + \cdots \quad (4.42)$$

Substitution of (4.42) into (4.41), the integrals can be evaluated in analytical form, giving

$$\frac{Z_{st}/Le_O}{(1-l_F)+Z_{st}l_F-Z_{st}l_O} = \frac{1}{4Le_F\chi_f}\left(1+l_O Le_O\frac{-\zeta_f^2+4Le_F\chi_f}{4Le_F\chi_f}\right)\exp\left(-\frac{\zeta_f^2}{4Le_F\chi_f}\right) \quad (43)$$

In leading order approximation, we may neglect all terms of order $O(l_F)$ and $O(l_O)$ in equation (4.43), which after algebraic arrangement, gives an explicit flame contour expression as

$$\zeta_f^2 \approx 4Le_F\chi_f \ln\left(\frac{1}{4Le_F\chi_f Z_{st}/Le_O}\right) \tag{4.44}$$

Substitution of the leading order approximation (4.44) into the first order term in (4.43), which is proportional to $l_O Le_O$, we can furthermore obtain an explicit flame contour expression retaining first order correction terms as

$$\frac{\zeta_f^2}{4Le_F} \approx \chi_f \ln\left[\frac{1 - l_F + Z_{st}l_F - Z_{st}l_O + l_O Le_O \ln\left(4eLe_F\chi_f\, Z_{st}/Le_O\right)}{4Le_F\chi_f\, Z_{st}/Le_O}\right] \tag{4.45}$$

Applying inverse transformations of (4.6) and (4.13) to equations (4.39) and (4.45), which can be regarded as proper scaling according to the vortical flow characteristics and the variations of density and mass diffusivity radially and axially, we can obtain the flame contours in physical coordinates, as shown in Figure 4.1.

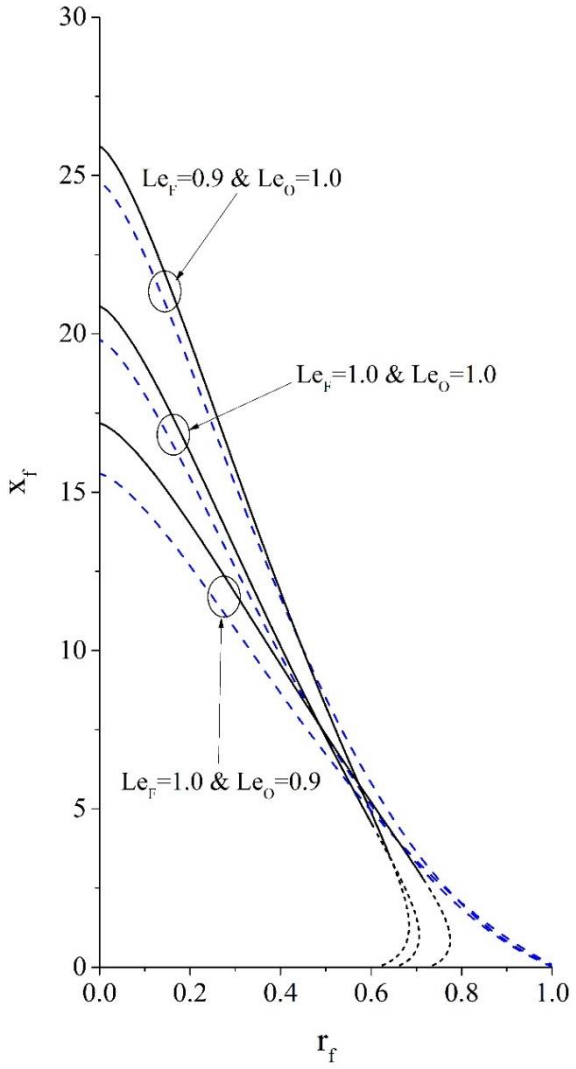

Figure 4.1 The Lewis number effects on flame contour. The solid lines represent the explicit (approximate) flame contours determined by equation (4.45), and the dashed lines are the corresponding implicit (accurate) flame contours according to equation (4.39).

The flame contours with respect to various pairs of Lewis numbers are plotted in Figure 4.1, according to which, decreasing of fuel Lewis number tends to expand the flame contour, particularly in axial direction, while the oxidizer Lewis number exhibits the inverse effect on the flame contour. The reason can be interpreted as follows. The

Lewis numbers can in physics be interpreted as the ratio of thermal diffusivity to mass diffusivity. The smaller Lewis number of fuel than that of oxidizer implies that the fuel has larger mass diffusivity than oxidizer, due to which the fuel has higher capability to be transported to larger altitude, i.e., extending the flame contour in axial direction. In opposite situation, i.e., Lewis number of oxidizer being lower than that of fuel, the larger mass diffusivity of oxidizer tends to squeeze flame contour, especially in the axial direction because the flame end close to the fuel pool is anchored at the rim of fuel pool due to flame sheet approximation. According to Chung and Law [15] the flame characteristics determined by the near-unity Lewis number asymptotic analysis is of high accuracy at least as the Lewis numbers ranging from 0.7 to 1.3, and can be extrapolated into a larger variation of Lewis number with acceptable accuracy.

In Figure 4.1 it shows that the deviations between the explicit flame contours (4.45) and the implicit ones (4.39) become more significant as the flame closing to the fuel pool surface, as indicated by the short dashed turning curves. The mathematical reason is that for small axial flame locations, $\chi_f \ll 1$, the integrals in equation (4.41) cannot be evaluated asymptotically in the sense of Laplace. In a particular case of $\chi_f = 0$, the integrals in (4.41) becomes divergent as indicated in previous studies[12, 36]. In physics, such problem results from the fact that the large Peclet number approximation, which is the basis of most formulations of circulation-controlled firewhirls[13, 35, 74,

75], becomes invalid close to the fuel pool surface, i.e., the axial diffusion can by no means be neglected.

4.6 Flame height

One particular location on the flame contour is the flame height, where $\zeta_f = 0$. Accordingly, equation (4.39) can be simplified to

$$\frac{Z_{st}/Le_O}{(1-l_F)+Z_{st}l_F-Z_{st}l_O} = \int_0^\infty J_1(\omega)\exp\left(-Le_F\omega^2\chi_f\right)d\omega + l_O Le_O \times \int_0^\infty Le_F\chi_f\omega^2 J_1(\omega)\exp\left(-\omega^2 Le_F\chi_f\right)d\omega \quad (4.41)$$

Both integrals on the RHS of equation (41) can be evaluated exactly as

$$\int_0^\infty J_1(\omega)\exp\left(-Le_F\omega^2\chi_f\right)d\omega = 1-\exp\left(-\frac{1}{4Le_F\chi_h}\right) \quad (4.42)$$

$$\int_0^\infty Le_F\chi_f\omega^2 J_1(\omega)\exp\left(-Le_F\omega^2\chi_f\right)d\omega = \frac{1}{4Le\chi_f}\exp\left(-\frac{1}{4Le_F\chi_f}\right) \quad (4.43)$$

Substitution of equations (4.42) and (4.43) into (4.41) and recalling the fact that $4Le_F\chi_f \gg 1$ in circulation controlled firewhirls, the flame height expression simplifies to

$$\chi_h = \frac{Le_O}{4Le_F}\left(\frac{1}{Z_{st}}+\frac{l_O Le_O}{Z_{st}}-\frac{l_F}{Z_{st}}+l_F-l_O\right) \quad (4.44)$$

where terms of order higher than $O(l_F)$ or $O(l_O)$ have been neglected. The leading order approximation to the flame height can be obtained by further removing all terms of first order, giving

$$\chi_h^0 = \frac{Le_O}{Le_F}\frac{1}{4Z_{st}} \tag{4.45}$$

Writing the Lewis numbers Le_F and Le_O in terms of their definitions, equation (4.45) becomes

$$\chi_h^0 = \frac{D_F}{D_O}\frac{1}{4Z_{st}} = \frac{\alpha_D}{4Z_{st}} \tag{4.46}$$

which coincides with the flame height in Chapter III considering distinct mass diffusivities for fuel and oxidizer[74], implying that the effect of the latter is the leading order approximation of that of non-unity Lewis number.

Applying inverse transformations of (4.6) and (4.13) to the flame height expression (4.44), we obtain an explicit expression of flame height in physical coordinates, i.e.,

$$\frac{x_h}{d_0} = \frac{Le_O}{Le_F}\frac{2}{\alpha_v}\left(\frac{T_m}{T_0}\right)^{2-\alpha_T}\frac{Pe}{16Z_{st}}(1 + l_O Le_O - l_F + Z_{st}l_F - Z_{st}l_O) \tag{4.47}$$

where T_m denotes a representative temperature[74, 75] defined by

$$T_m = \left[\frac{1}{x_h}\int_0^{x_h} T^{\alpha_T - 2}dx\right]^{1/(\alpha_T - 2)} \tag{4.48}$$

whose magnitude is definitely larger than the bottom temperature at the fuel pool T_0. And α_T specifies the temperature-dependence of mass diffusivities within the flame through

$$D_F = D_{F0}\left(\frac{T}{T_0}\right)^{\alpha_T} \tag{4.49}$$

in which α_T is usually less than 2 and equal to 3/2 in kinetic theory of gases employing the rigid-sphere model. The combining of T_m and α_T in the term $(T_m/T_0)^{2-\alpha_T}$ specifies that regarding density and mass diffusivity as variables results in a larger flame height than treating those physical properties as constants. The physics can be interpreted that the density decreases due to the presence of flame, so is the flow inertia, thus the fuel flux tends to be more readily to be transported to higher altitude, i.e., lengthening of flame height.

The overall exponent α_v characterizes the overall behavior of the generalized power-law vortical flow[33-35]. In the special case of Burgers vortex, the exponent is exactly equal to 2, whereas in real vortical flow, particularly for circulation-controlled firewhirls, the overall exponent should be smaller than 2[33-35], because the strong circulation flow could induce more rapid axial flow according to continuity of fluid, therefore, an intensified axial stretching tends to elongate the flame height than that of Burgers vortex. The overall exponent α_v can be expressed in terms of inner exponent α_{v1} and outer exponent α_{v2} by adopting the self-similar mixture fraction solutions, which will be discussed in the following section.

4.7 Determination of α_v

Due to non-unity Lewis numbers, the overall conserved species-species coupling function cannot be easily defined. Whereas, the mixture defined by

$$Z = \frac{\tilde{Y}_F + \tilde{Y}_{O\infty} - \tilde{Y}_O}{\tilde{Y}_{F0} + \tilde{Y}_{O\infty}} \tag{4.50}$$

satisfies the conservation equation with distinct transport coefficients in fuel and oxidizer region respectively, i.e.,

$$\tilde{\rho}\tilde{u}\frac{\partial Z}{\partial \tilde{x}} + \tilde{\rho}\tilde{v}\frac{\partial Z}{\partial \tilde{r}} - \alpha_Z \frac{2}{Pe}\frac{\partial}{\partial \tilde{x}}\left(\tilde{\rho}\widetilde{D}_F \frac{\partial Z}{\partial \tilde{x}}\right) - \alpha_Z \frac{2}{Pe}\frac{1}{\tilde{r}}\frac{\partial}{\partial \tilde{r}}\left(\tilde{\rho}\widetilde{D}_F \tilde{r}\frac{\partial Z}{\partial \tilde{r}}\right) = 0 \tag{4.51}$$

where $\alpha_Z = 1$ for $Z > Z_{st}$ in the fuel region, and $\alpha_Z = Le_F/Le_O$ for $Z < Z_{st}$ in the oxidizer region.

Applying transformation (6) to equation (51), assuming large Peclet number, we obtain

$$\hat{u}\frac{\partial Z}{\partial \xi} + \hat{v}\frac{\partial Z}{\partial \eta} - \alpha_Z \frac{1}{\eta}\frac{\partial}{\partial \eta}\left(\eta \frac{\partial Z}{\partial \eta}\right) = 0 \tag{4.52}$$

Utilizing Klimenko's self-similar solution[34, 35], the mixture fraction distributions in the fuel and oxidizer regions can be determined as

$$Z_F = \frac{1}{2\xi A}\exp\left(\int_0^\eta \hat{v}d\eta'\right), \qquad Z_O = \frac{Le_O}{Le_F}\frac{1}{2\xi A}\exp\left(\frac{Le_O}{Le_F}\int_0^\eta \hat{v}d\eta'\right) \tag{4.53}$$

where

$$A = \frac{1}{\xi}\int_0^{\infty} \hat{u} \exp\left(\int_0^{\eta} \hat{v} d\eta'\right) \eta d\eta \tag{4.54}$$

is regarded as constant[34, 35].

The general mixture fraction can formally be written as a combination of Z_F and Z_O in the form of

$$Z = Z_O + c(\xi, \eta)(Z_F - Z_O) \tag{4.55}$$

where $c(\xi, \eta)$ approaches to unity near the fuel pool and to zero far away from the flame, thus the magnitude of $c(\xi, \eta)$ should be bounded in the interval $[0,1]$.

The flame height can be determined by setting "radial" coordinate η equal to zero and the mixture fraction Z in (4.55) to Z_{st}, i.e.,

$$\xi_h = \frac{Le_O}{Le_F}\frac{1}{2AZ_{st}}[1 + c(\chi, \eta)(l_F - l_O)] \tag{4.56}$$

where the Lewis number ratio has been written in terms of l_F and l_O. Applying the inverse transformation (4.6) to (4.56), we can obtain the flame height in physical coordinates as

$$\frac{x_h}{d_0} = \frac{Le_O}{Le_F}\frac{2}{A}\left(\frac{T_m}{T_0}\right)^{2-\alpha_T}\frac{Pe}{16Z_{st}}[1 + c(\chi, \eta)(l_F - l_O)] \tag{4.57}$$

Comparing to flame height expression (47), it indicates that the constant A plays the same role as the overall exponent of the generalized power-law vortex model, thus we can regard

$$\alpha_v = A = \frac{1}{\xi}\int_0^{\infty} \hat{u} \exp\left(\int_0^{\eta} \hat{v} d\eta'\right) \eta d\eta \tag{4.58}$$

Substitution of velocity components in (4.12) we can determine the overall exponent in the form of

$$\alpha_v = \alpha_{v1} - (\alpha_{v1} - \alpha_{v2}) \exp\left(-\frac{\eta_c^{\alpha_{v1}}}{\alpha_{v1}}\right) \tag{4.59}$$

4.8 Equal Lewis numbers

In a particular case of equal Lewis numbers, the flame height tends to remain almost fixed according to equation (4.44), or particular in leading order approximation, (4.46), whereas the flame contour should depend on the magnitudes of Lewis numbers. Figure 4.2 testifies the independence of flame height on the equal Lewis numbers, while the flame contours with larger Lewis number magnitudes tend to be slimmer than those with lower Lewis number magnitudes. The physical reason can be interpreted as follows. The larger Lewis numbers for both fuel and oxidizer implies lower overall mass diffusivities, in case of which the axial convection effect tends to be more dominant than diffusion, resulting in a preference of flame contour in axial direction. In the opposite situation, i.e., lower Lewis numbers for fuel and oxidizer, the intensified diffusion, to some extent, tends to overcome the axial preference of flame contour due to convection, rendering the flame contour to be stout.

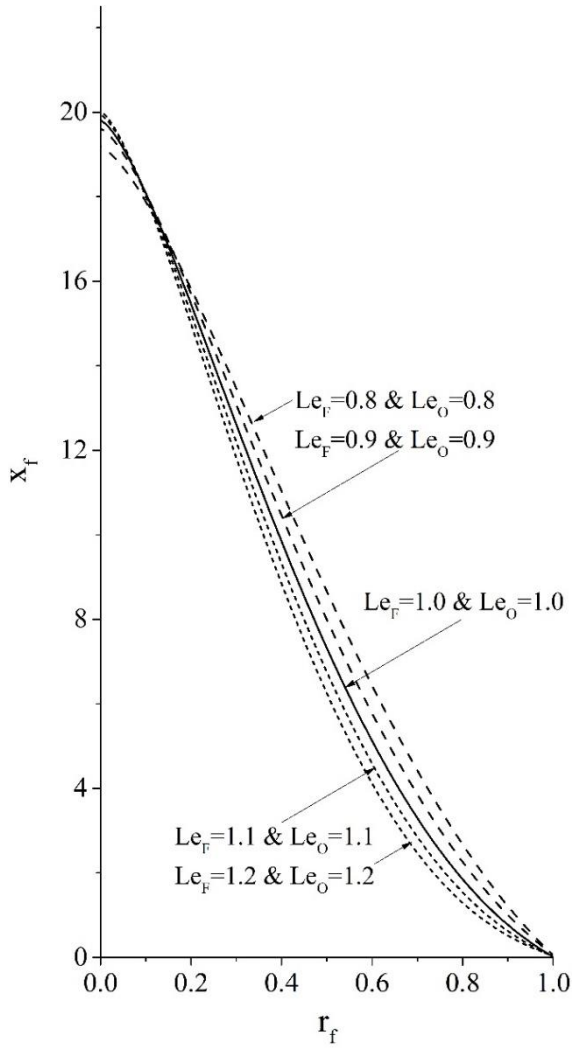

Figure 4.2 The effects of equal Lewis numbers on the flame contours.

Chapter V Concluding Remarks

In this part, we have conducted a series of theoretical studies on the flame height of circulation-controlled firewhirls, concerning the effects of variable physical properties, distinct transport properties and non-unity Lewis number, respectively in chapter II to chapter IV, the summary to each of which is given as follows.

In chapter II, the variable density effect on the flame height of circulation-controlled firewhirls is investigated theoretically by assuming the flow field as steady, axisymmetric Burgers vortex. Through a Howarth-Dorodnitsyn-like, density-mass-diffusivity-weighted coordinate transformation, the governing equation for the coupling functions are simplified to the density-mass-diffusivity-implicit form. Then the existing formulations for constant density and mass diffusivities can be formally adopted. Similar to the previous studies based on the constant density assumption, the normalized flame height x_h/d_0 can be expressed as a linear function of the modified Peclet number $\mathrm{Pe}/16Z_{st}$. An additional increase in flame height due to the variable density effect is determined by a multiplication factor $(T_m/T_0)^{2-\alpha_T}$, in which T_m is a temperature integral within the core of firewhirl, T_0 the average temperature of fuel vapor on the surface, and α_T determines the temperature dependence of mass diffusivity. Either the physically realistic $\alpha_T = 1.8$ or the approximate value $\alpha_T = 1.5$ from the kinetic theory of gases predict well the previous experimental data by Chuah et al. [13]. Consequently, the present theory provides an alternative

interpretation to the increased flame heights of circulation-controlled firewhirls, which was attributed by Klimenko and Williams to the deficiency of constant-density Burgers vortex in accounting for strong rotation.

In chapter III, a theory of the flame height of firewhirls has been established by means of coupling function formulation, with a particular interest in approximately combining variable physical properties, a power-law vortex model and a mass-diffusivity-ratio model in the theory. Although the specified boundary conditions and the adopted approximations remain to be further verified, interesting and useful understanding on the problem has been obtained.

In terms of the approximate matching solutions of the coupling functions, the theory yields a composite expression for the flame height, which can degenerate to those obtained in the previous studies [13, 35, 75], in the expression, the linearity between the diameter-scaled flame height x_h/d_0 and modified Peclet number $Pe/(16Z_{st})$ remains; the slope of the linear reaction is characterized by three factors, each of which interprets independent and indispensable physics. Specifically, the effect of variable density and diffusivities, characterized by $\left(T_m/T_0\right)^{2-\alpha_T}$, results in reduced flow inertia and thus tends to increase the flame height. The effect of the power-law strong vortex, characterized by $2/\alpha_v$ with $\alpha_v < 2$, leads to the intensified axial stretching of the vortical flow near the axis thus causes the flame tip at the axis to grow higher. The effect of the distinct mass diffusivities of fuel and oxidizer, characterized

by $\alpha_D < 1$, requires a larger gradient of fuel mass fraction within the flame contour, moves the flame closer to the fuel pool, and thus reduces the flame height. Combining the first two effects yields a considerable overestimation for the flame height, which can be satisfactorily corrected by the third factor, resulting good agreement with the experimental results.

In chapter IV, a theory of the flame contour, particularly the flame height of circulation-controlled firewhirls with emphasis on the effect of non-unity Lewis numbers has been established in the present study by means of perturbation method, regarding the deviations of fuel and oxidizer Lewis numbers from unity as small parameters. In this theory, the variable physical properties and generalized power-law vortex model has also been implemented. Although the perturbation method restricts the variations of Lewis number to close to unity, interesting and meaning understanding on the problem has been obtained.

Retaining first order corrections in the asymptotic expansion modified coupling functions the theory yields both an implicit (accurate) and an explicit (approximate) flame contours, which coincides with the former at locations not to close to the fuel pool, where the deviations become significant. Both flame contour expressions indicate that decreasing of fuel Lewis number tends to extend the flame contour, particular in axial direction, whereas lowering the oxidizer Lewis numbers results in the shrinking of flame contour. The physical reason is that small Lewis numbers for fuel and oxidizer

implies large mass diffusivities, respectively, the former of which enables the fuel to be transported to larger altitude, thus extending the flame height, whereas the latter of which tends to suppress the transport of fuel, resulting in the decrease of flame height.

Either by means of the perturbation solution of modified coupling functions or self-similar solutions of mixture fractions we can determine composite flame height expressions in physical coordinates, respectively, as equation (4.47) and (4.58), which coincide with each other to the dominating order of $O(1/Z_{st})$. In the flame height expressions, the slope of linear relation between the diameter-scaled flame height x_h/d_0 and the modified Peclet number $Pe/16Z_{st}$ consists of three factors, namely, $(T_m/T_0)^{2-\alpha_T}$, characterizing the variable density and mass diffusivity effect, resulting in reduced flow inertia and thus tends to elongate the flame height, $2/\alpha_v$, specifying the power-law strong vortex, leading to the intensified axial stretching of the vortical flow near the axis, thus causing the flame tip to grow higher, and Le_O/Le_F, indicating the non-unity Lewis number effect, modulating diffusion transport capabilities of fuel and oxidizer, resulting in flame height extension for $Le_F < Le_O$ or shrinking in the opposite situation.

For equal Lewis numbers, the flame height almost remains fixed, whereas the flame contour undergoes deformation. For large Lewis numbers, the overall mass diffusivity becomes lower, thus the flame contour tends to be more dominated by the axial convection due to large Peclet number, thus to be slim. In the contrary, small Lewis

numbers implies large overall mass diffusivity, thereby the intensified diffusion could to some extend compete with the axial convection, thus overcoming the axial preference and resulting in stout flame contour.

Part II Periodically-Forced Jets

Nomenclature

Physical quantities

(English letters in alphabetical sequence)

a = speed of sound

A = amplitude of the periodic perturbation

$$A(x) = A_0 \exp(-\alpha_i x)$$

c_p = constant pressure specific heat

c_v = constant volume specific heat

D = diameter of the nozzle exit

f = physical frequency of the periodic perturbation

p = pressure

r = radial coordinate

t = time

T = temperature

u = axial velocity component

v = radial velocity component

w = azimuthal velocity component

x = axial coordinate

(Greek letters in alphabetical sequence)

α = complex angular wave number of the periodic perturbation

α_i = imaginary part of α, denoting the spatial growth rate of the periodic perturbation

α_r = real part of α, denoting the spatial periodicity of the perturbation

γ = heat capacity ratio

$$\gamma = c_p / c_v$$

θ = momentum thickness

ν = kinematic viscosity

ρ = density

ϕ = azimuthal coordinate

ω = angular frequency of the periodic perturbation

Overhead symbols

$\bar{Q}$ = physical quantities referring to the base flow

$$Q = (u, T, \rho, p)$$

Q' = physical quantities referring to finite-amplitude periodic perturbation

$$Q = (u, v, \rho, T, p)$$

$\hat{Q}$ = shape functions of physical quantities of periodic perturbation

$$Q = (u, v, \rho, T, p)$$

Subscripts

c = physical quantities of base flow along the axis

$$Q_c(x;\theta) = Q(r = 0, x;\theta), \qquad Q = (u, \rho, T)$$

p = quantities referring to the optimal excitation

s = shape functions of physical quantities of base flow

$$\bar{Q}_s(r;\theta) = \frac{\bar{Q}(x, r;\theta)}{\bar{Q}_c(x;\theta)}, \qquad Q = (u, T)$$

0 = physical quantities at the nozzle exit

$$Q_0(r;\theta_0) = Q(r, x = 0;\theta_0), \qquad Q = (u, A, \rho, p, T, \theta)$$

Nondimensional parameters

M = jet Mach number

$$M = \frac{u}{a}$$

Re = jet Reynolds number

$$Re = \frac{u_0 D}{\nu}$$

St = Strouhal number

$$St = \frac{fD}{u_0}$$

Radial integrals that are functions of x and parametrically depend on θ

E_B = kinetic energy flux of the base flow

$$E_B = 2\pi \int_0^\infty \left(\frac{1}{2}\bar{\rho}\bar{u}^3\right) r dr$$

E_P = kinetic energy flux of the perturbation

$$E_P = 2\pi \int_0^\infty \left[\frac{1}{2}\bar{\rho}\bar{u}\left(\overline{u'^2 + v'^2}\right)\right] r dr$$

E_T = thermal energy flux of the base flow

$$E_T = 2\pi \int_0^\infty \bar{\rho}\bar{u}\bar{T} r dr$$

F_B = mass flux of the base flow

$$F_B = 2\pi \int_0^\infty \bar{\rho}\bar{u} r dr$$

K = kinetic energy transfer rate from the base flow to the perturbation,

$$K = -2\pi \int_0^\infty \bar{\rho}\overline{u'v'}\frac{d\bar{u}}{dr} r dr$$

M_B = axial momentum of the base flow

$$M_B = 2\pi \int_0^\infty \bar{\rho}\bar{u}^2 r dr$$

W = power of the perturbed pressure on the perturbation

$$W = 2\pi \int_0^\infty \left(\overline{u' \frac{\partial p'}{\partial x} + v' \frac{\partial p'}{\partial r}}\right) r dr$$

Φ_B = viscous dissipation rate in the base flow

$$\Phi_B = \frac{2\pi}{Re_0} \int_0^\infty \left(\frac{d\bar{u}}{dr}\right)^2 r dr$$

Φ_P = viscous dissipation rate of the perturbed flow

$$\Phi_P = \frac{2\pi}{Re} \int_0^\infty \left\{ 2\left[\overline{\left(\frac{\partial v'}{\partial r}\right)^2} + \overline{\left(\frac{v'}{r}\right)^2} + \overline{\left(\frac{\partial u'}{\partial x}\right)^2}\right] + \overline{\left(\frac{\partial v'}{\partial x} + \frac{\partial u'}{\partial r}\right)^2} - \frac{2}{3}\overline{\left(\frac{\partial v'}{\partial r} + \frac{v'}{r} + \frac{\partial u'}{\partial x}\right)^2} \right\} r dr$$

Shape function integrals parametrically depending on θ

I_B = kinetic energy of the base flow

$$I_B = 2\pi \int_0^\infty \frac{1}{2} \bar{\rho}_s \bar{u}_s^3 r dr$$

I_K = kinetic energy transfer between the base flow and the periodic perturbation

$$I_K = -2\pi \int_0^\infty \bar{\rho}_s \, \hat{u}\hat{v} \frac{d\bar{u}_s}{dr} r dr$$

I_M = axial momentum of the base flow

$$I_M = 2\pi \int_0^\infty \bar{\rho}_s \bar{u}_s^2 r dr$$

I_P = kinetic energy of the periodic perturbation

$$I_P = 2\pi \int_0^\infty \bar{\rho}_s \bar{u}_s (\hat{u}^2 + \hat{v}^2)\, r dr$$

I_T = thermal energy of the base flow

$$I_T = 2\pi \int_0^\infty \frac{1}{2} \bar{u}_s r dr$$

I_W = power of the perturbed pressure on the periodic perturbation

$$I_W = 2\pi \int_0^\infty \left(\hat{u} \frac{\partial \hat{p}}{\partial x} + \hat{v} \frac{\partial \hat{p}}{\partial r} \right) r dr$$

$I_{\Phi B}$ = viscous dissipation of the base flow

$$I_{\Phi B} = \frac{2\pi}{Re_0} \int_0^\infty \left(\frac{d\bar{u}_s}{dr} \right)^2 r dr$$

$I_{\Phi P}$ = viscous dissipation of the periodic perturbation

$$I_{\Phi P} = \frac{2\pi}{Re_0} \int_0^\infty \left\{ 2 \left[\overline{\left(\frac{\partial \hat{v}}{\partial r} \right)^2} + \overline{\left(\frac{\hat{v}}{r} \right)^2} + \overline{\left(\frac{\partial \hat{u}}{\partial x} \right)^2} \right] + \overline{\left(\frac{\partial \hat{v}}{\partial x} + \frac{\partial \hat{u}}{\partial r} \right)^2} - \frac{2}{3} \overline{\left(\frac{\partial \hat{v}}{\partial r} + \frac{\hat{v}}{r} + \frac{\partial \hat{u}}{\partial x} \right)^2} \right\} r dr$$

Chapter VI Introduction

Circular jet with large-scale coherent structures plays an important role in various propulsion systems. A prominent example is that the large-scale coherent structure developed in the shear layer of a co-flow fuel jet can promote the near-field mixing [28, 29, 76] in hypersonic propulsion system such as scramjet, where the residence time of the base flow in the combustion chamber is so short that the combustion performance vitally relies on the rapid mixing of fuel and air [18, 25]. Although the mixing of a circular fuel jet with a co-flow air is often less effective than that of a transverse fuel injection, the smaller loss of total pressure in the former makes it a viable mixing approach at very high Mach numbers.

The mixing process in a high-speed jet is controlled by the spreading of the shear layer [22], surrounding the potential core where the axial flow velocity is almost uniform [57]. In the downstream of the jet, where the shear layer spreads in radial direction and entrains ambient fluids into the jet [78], the potential core becomes thinner and finally vanishes in the about five-nozzle-diameter downstream for incompressible jets [17, 30, 57]. In the further downstream of the potential core, the jet flow is fully developed so that its axial velocity profile is self-similar and that the further development of the jet flow is independent of the issuing condition at the nozzle orifice [65]. For compressible jets, the potential core can be prolonged with increasing the jet Mach number [56, 77] because the flow compressibility suppresses the spreading of the

shear layer [78]. In the recent studies of Samimy *et al*. [63, 64], the potential core can be six or seven times nozzle diameter for compressible jets with imposed periodic forcing.

Spreading of a shear layer can be facilitated by the formation and evolution of coherent structure [10, 49, 76], originating from the amplification [17, 26, 30, 31, 52] of the unstable perturbations from either random flow disturbance or purposely imposed external periodic excitation. The emergence and evolution of the large scale coherent structure, whose kinetic energy is supplied by the jet flow [49], will lead to significant entrainment of the ambient fluid into the shear layer. The coherent structure can be artificially generated by implementing external periodic perturbation on the jet flow at the nozzle exit with some forcing technique [58]. Hussain and Zaman [28, 30] investigated the passage frequency of the coherent structure, i.e., the axial periodicity, at a specified axial location (usually at the end of potential core). They discovered that the axial periodicity locked into the frequency of the forcing imposed at the nozzle exit [30], in contrast to the unforced situation where the axial periodicity was stochastic. Therefore, the periodic forcing to a jet can enhance the spreading of the shear layer in the near field.

The forced periodic perturbation at the nozzle exit is characterized by both frequency and amplitude. The previous experimental studies have discovered that the jet shear layer can undergo a maximum spreading [8, 10, 17, 30, 32] under a periodic

forcing of a fixed amplitude but with an optimal frequency. In contrast, the forcing amplitude tends to monotonically [8, 10, 17, 30, 32] influence the spreading of shear layer when the forcing frequency is fixed. The optimal forcing mode is not an equivalent to the extensively investigated jet-preferred mode: the former refers to an imposed periodic forcing by which the jet spreading is maximized, but the latter refers to that whose amplitude is maximized by the combined effects of linear amplification and nonlinear saturation[17]. The optimal Strouhal number for incompressible jets varies from 0.2 to 0.6 depending on the nozzle exit geometry [3, 78], the forcing amplitude [17, 22, 30] and the jet Reynolds number [50]. For compressible jets, Borisov and Gynkina [8, 22] investigated the effect of external periodic excitation on the mixing enhancement in the subsonic jets with Mach number ranging from 0.15 to 0.9, and found that the maximum spreading can be observed for Strouhal number between 0.25 and 0.3.

In spite of the extensive studies focusing on the incompressible jets, the compressible jets in a wide range of Mach number have not been sufficiently studied. In the present study, we theoretically analyzed the effects of periodic forcing on the spreading of compressible axisymmetric jets with the jet Mach number ranging from 0.1 to 3.0 by adopting the energy integral method. energy integral method was first proposed by Stuart [66] and subsequently applied by Liu [46] to free shear layers, by Morris [53] to the noise generation in a supersonic circular jet, and by Mankbadi [49]

to incompressible jets under periodic forcing. Comparing with the recently rising PSE (parabolized stability equation) approach [45, 48], which precisely considers the diverging effects of the base flow and the radial profile of the perturbation wave in the axial direction, energy integral method highlights the energy conversion between the main flow and the perturbation wave with a substantially lower computational demand.

In Chapter 7, we will present the mathematical formulation of the spreading of periodically-forced jet problem based energy integral method, which leads to a set of coupled ODEs containing a number of energy integrals, with solutions being calculated using numerical approach. In Chapter 8, the non-monotonic variation of the optimal forcing frequency with jet Mach number under various parametric conditions will be discussed in detail. In Chapter 9, a concluding remark is summarized for the whole part.

Chapter VII Mathematical Formulation

7.1 Energy integral equations

For a compressible, axisymmetric jet issuing from a circular exit into an unbounded quiescent environment of the same fluid, the cylindrical coordinate is established so that the jet exit is located at the origin of the symmetry axis, as shown in Figure 7.1. The jet flow properties at $x = 0$, such as the density, the static pressure, the static temperature, and the axial velocity, are used to nondimensionalize the conservation equations. With a periodic forcing imposed on the jet flow at the exit, the jet flow field can be decomposed into the mean and perturbation parts as

$$Q = \bar{Q} + Q' \tag{7.1}$$

where $Q = (u, v, \rho, p, T)$. In this study, we regard this finite-amplitude periodic perturbation as a coherent wave structure and consider its spatial evolution within the potential core of the mean jet flow [16, 52]. Earlier local spatial analyses [4, 52] showed that helical perturbations are spatially amplified in the downstream of potential core. It has also been substantiated by the recent global stability analysis of Garnaud *et al*. [21] that the growth of perturbations through the potential core is similar for various azimuthal wave numbers.

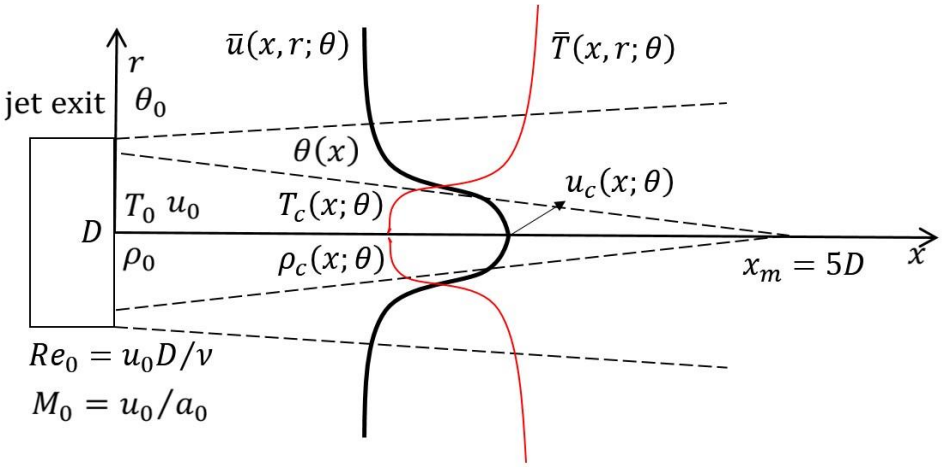

Figure 7.1 Schematic of the compressible axisymmetric jet.

It is noted that Q' can be further decomposed into the coherent part, which can be formed via phase average, and the incoherent parts, which describes the effect of turbulence and can be modeled by using an isotropic eddy viscosity [53]. Such a triple decomposition is however unnecessary in the present analysis because the incoherent fluctuation is insignificant in the potential core [30] compared with the coherent part. Furthermore, the energy integral equations to be presented shortly have the same mathematical forms as those based on the triple decomposition, except that the dynamic viscosity in the former is replaced by an eddy viscosity in the latter.

Following the study of Morris [53], we invoked the boundary-layer assumption to simply the momentum equation, integrated the equation with respect to the radial coordinate, neglected the covariance of density, temperature and axial velocity perturbations [53], and obtained the equation describing the axial development of the kinetic energy for the mean jet flow as

$$\frac{dE_B}{dx} = -K - \Phi_B \tag{7.2}$$

and the kinetic energy for the periodic perturbation

$$\frac{dE_P}{dx} = K + W - \Phi_P \tag{7.3}$$

To account for the non-negligible energy transfer from the kinetic energy to the thermal energy in the jet flows of high Mach numbers [47], we considered the conservation of total energy

$$\frac{d}{dx}[E_T + (\gamma - 1)M_0^2 E_B + (\gamma - 1)M_0^2 E_P] = 0 \tag{7.4}$$

which is absent in Morris's formulation for incompressible jets. In addition, we have the conservation of axial momentum of the base flow

$$\frac{dM_B}{dx} = 0 \tag{7.5}$$

Following Lesshafft and Heurre [44], we can write the equation of state as

$$\bar{p} = \frac{1}{\gamma M_0^2}\bar{\rho}\bar{T} \tag{7.6}$$

where the pressure is normalized by the dynamic pressure $\rho_0 u_0^2$. The integral forms of E_B, E_P, E_T, K, W, Φ_B, Φ_P, and M_B have been defined in the nomenclature, and thus will not be repeated in the following discussion. In the present formulation, the flow is assumed to be calorically perfect with the heat capacity ratio $\gamma = 1.4$.

7.2 Shape functions of base flow and perturbation

Equations (7.2)-(7.6) provide a formulation for calculating the energy conversion between the base flow and the periodic perturbation, given by that the radial distributions of the mean and perturbation components of the flow are described by shape functions [47]. We adopted the velocity shape function suggested by Michalke [52],

$$\bar{u}_s(r;\theta) = \frac{1}{2}\left\{1 + \tanh\left[\frac{1}{4\theta(x)}\left(\frac{1}{r} - r\right)\right]\right\} \tag{7.7}$$

which describes the radial profile of the mean jet flow velocity within the potential core ending at $\theta \approx 0.25$ [52]. The temperature shape function can be determined by the Crocco-Busemann relation [49, 52, 53], which is special solution of energy equation assuming unity Prandtl number. In the present problem, the relation implies the uniformity of total sensible enthalpy in the radial direction and is written by

$$\bar{T}_s(r;\theta) = 1 + \frac{1}{2}(\gamma - 1)\, M_c(x)^2[1 - \bar{u}_s^2(r;\theta)] \tag{7.8}$$

The assumption of constant mean pressure throughout the entire flow field renders that the shape function of density is simply the reciprocal of temperature as

$$\bar{\rho}_s(r;\theta) = \frac{1}{\bar{T}_s(r;\theta)} \tag{7.9}$$

Cohen and Wygnanski [16] showed that the profile of perturbation can be well approximated by that of linear instability waves within the potential core for an

incompressible circular jet. This was further substantiated by Suzuki and Colonius [68] for compressible circular jets. Consequently, we followed these results by assuming that the axisymmetric periodic perturbation in the potential core has the profile of linear instability modes:

$$u' = \frac{1}{2}[A(x)\hat{u}(r;\theta)\exp(i\alpha_r x - i\omega t) + c.c.] \tag{7.10}$$

$$v' = \frac{1}{2}[A(x)\hat{v}(r;\theta)\exp(i\alpha_r x - i\omega t) + c.c.] \tag{7.11}$$

$$p' = \frac{1}{2}\left(\frac{1}{\gamma M_0^2}\right)[A(x)\hat{p}(r;\theta)\exp(i\alpha_r x - i\omega t) + c.c.] \tag{7.12}$$

where $c.c.$ is the abbreviation for a complex conjugate. The temperature and density perturbations are not required because they do not appear explicitly in the governing ODEs to be presented shortly. It is noted that inviscid eigenmodes of linear instability waves were adopted in the present analysis because Morris [54] showed that the influence of viscosity on the growth rate of the linear instability waves is insignificant at high Reynolds numbers. The linear stability analysis of inviscid compressible circular jets has been comprehensively discussed by Michalke [52]. Some important relations used in the present analysis are concisely summarized in the Appendix F.

7.3 ODEs for jet response system

Substituting the shape functions of both base flow and periodic perturbations, i.e. Equations (7.7)-(7.12), into Equations (7.2)-(7.6), we have

$$\frac{d}{dx}[\bar{\rho}_c \bar{u}_c^3 I_B] = -\bar{\rho}_c \bar{u}_c A^2 I_K - \bar{u}_c^2 I_{\Phi B} \tag{7.13}$$

$$\frac{d}{dx}[\bar{\rho}_c \bar{u}_c A^2 I_P] = -A^2 I_{\Phi P} + A^2 I_W + \bar{\rho}_c \bar{u}_c A^2 I_K \tag{7.14}$$

$$\frac{d}{dx}[\bar{u}_c I_T + (\gamma - 1) M_0^2 \, \bar{\rho}_c \bar{u}_c^3 I_B + (\gamma - 1) M_0^2 \bar{\rho}_c \bar{u}_c A^2 I_P] = 0 \tag{7.15}$$

$$\bar{\rho}_c \bar{u}_c^2 I_M = \int_0^\infty \bar{\rho}_0 \bar{u}_0^2 dr \tag{7.16}$$

$$\bar{\rho}_c = 1/\bar{T}_c \tag{7.17}$$

which constitutes an ODE system of initial value problem for five unknown variables, $\bar{u}_c(x)$, $\bar{\rho}_c(x)$, $\bar{T}_c(x)$, $A(x)$, and $\theta(x)$. The integral forms of I_B, I_P, I_T, I_K, I_W, $I_{\Phi B}$, $I_{\Phi P}$, and I_M have been defined in the nomenclature, and thus will not be repeated in the following discussion.

The ODE system contains four controlling parameters defined at the jet exit, namely M_0, Re_0, θ_0, and A_0 of the shear layer. In the present energy analysis, the influence of the amplitude of perturbation can be considered as an input of perturbation energy to the base flow [63]. Consequently, we shall replace A_0 in the following discussions by the ratio of the kinetic energy of perturbation to that of the base flow at the exit,

$$R_K = \frac{E_P(0)}{E_B(0)} = \frac{A_0^2 I_P(\theta_0)}{u_0^2 I_B(\theta_0)} \tag{7.18}$$

from which it is seen that R_K is proportional to A_0^2.

The computational domain spans from the jet exit to the downstream location of five times diameters. The domain-dependence of the results will be discussed in the following section. The calculation domain is discretized into 50 uniform grid cells, within which the ODE system is solved by using the 4th-order Runge-Kutta algorithm and the integrals are evaluated by using the Simpson quadrature algorithm. Because all the shape function integrals depend on $\theta(x)$, the ODE system is solved iteratively in each cell until the largest relative errors are less than 10^{-4}, which is defined as the criterion for convergence. Moreover, a linear stability analysis should be performed in every iteration in order to obtain the complex wave number α and the eigenmode of linear instability wave which serve as the shape functions for periodic perturbations. It takes about 100 seconds of a single CPU to solve the ODE system by using MATLAB.

7.4 Axial development of the perturbed jet

We first examine the axial development of the perturbed jet under a typical flow condition with $M_0 = 1.5$, $Re_0 = 5 \times 10^4$, $\theta_0 = 0.025$ and $R_K = 0.01$, for various Strouhal numbers. It is shown in Figure 7.2(a) that $\bar{u}_c(x)$ decreases monotonically along the axial direction because the continuous entrainment of surrounding fluid into

the base flow slows down the base flow. The insignificant decrease of $\bar{u}_c$ (less than 10%), even in the presence of periodic excitation, accords with the definition of potential core [57]. It is interesting to observe that the minimum value of $\bar{u}_c(x)$ is attained at $x = 5$, namely, the downstream boundary of the potential core, and that $\bar{u}_c(x = 5)$ decreases and then increases with St, implying a non-monotonic influence of periodic forcing on the jet development. To further understand this observation, we plotted in Figure 7.2(b) the mass flux of the base flow, $F_B(x)$, and found that it increases monotonically with x and reaches a maximum value at $x = 5$ owing to the flow entrainment. The non-monotonic variation of $F_B(x = 5)$ with St is responsible for that of $\bar{u}_c(x = 5)$ because the jet momentum, which can be rewritten as $F_B(x)\bar{u}_c(x)$, remains constant at any axial location according to Equation (7.5). In addition, a critical value of $St = 0.22$ can be identified to correspond to the maximum decay of axial velocity, or equivalently, maximum mass flux within the potential core.

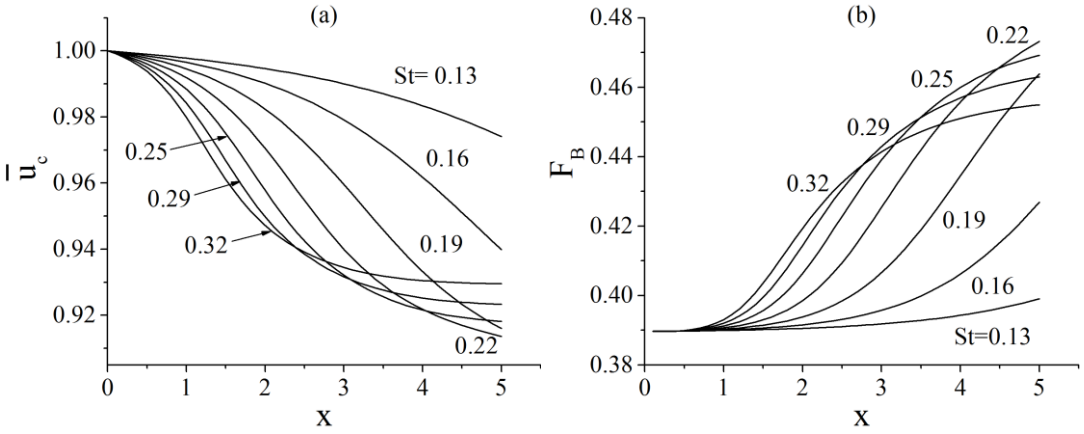

Figure 7.2 a) The axial variation of the centerline velocity; b) the mass flux of the base flow. The flow conditions are $M_0 = 1.5,\ R_K = 10^{-2}, Re_0 = 5 \times 10^4$, and $\theta_0 = 0.025$.

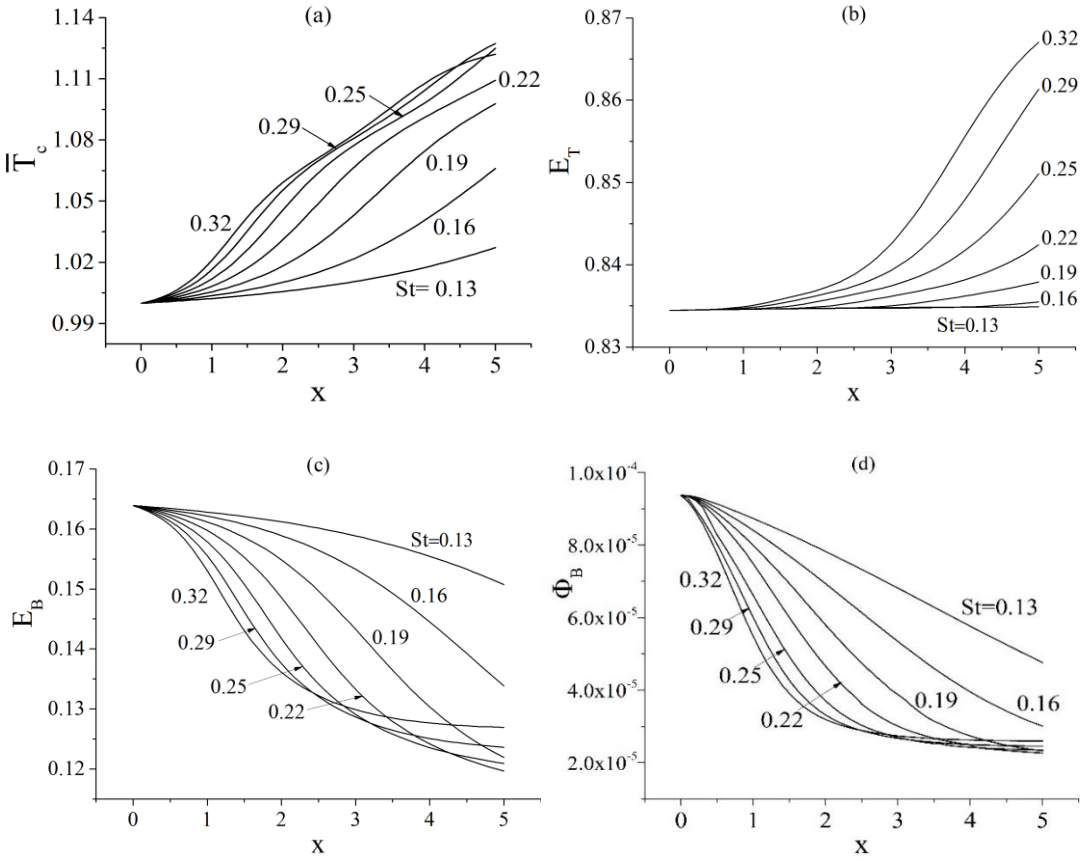

Figure 7.3 a) The axial variation of the centerline temperature; b) the thermal energy flux; c) the kinetic energy flux; d) The viscous dissipation of the base flow. The flow conditions are $M_0 = 1.5,\ R_K = 10^{-2}, Re_0 = 5 \times 10^4$, and $\theta_0 = 0.025$.

The significant axial increase of the centerline temperature $\bar{T}_c(x)$ is shown in Figure 7.3(a) and therefore substantiates the necessity of invoking the total energy conservation in the analysis. The maximum temperature increase within the potential core can be up to 12% under the typical condition as St increases to 0.32. Accordingly,

the thermal energy flux of the base flow, $E_T(x)$, monotonically increases with St as shown in Figure 7.3(b). The non-monotonic variation of $\bar{T}_c(x=5)$ with St can be attributed to that of the mass flux $F_B(x)$ because of the approximate relation $E_T(x) \sim F_B(x)\bar{T}_c(x)$. Furthermore, the decrease of the kinetic energy flux of the base flow, $E_B(x)$, as shown in Figure 7.3(c), demonstrates that the energy transfer from the base flow to other energy forms is a one-way process. The maximum decrease of $E_B(x)$ within the potential core occurs at $St = 0.22$, which is in accordance with the variation of $\bar{u}_c(x)$ discussed above. Finally, the monotonic decrease of the viscous dissipation rate of the base flow, as shown in Figure 7.3(d), is due to the decrease of the velocity gradient along the axial coordinate as the result of radial spreading of the jet. It is also seen that the viscous dissipation of the basic flow is negligibly small for $Re_0 = 5 \times 10^4$ and may be of some significance in energy budget for smaller Reynolds numbers.

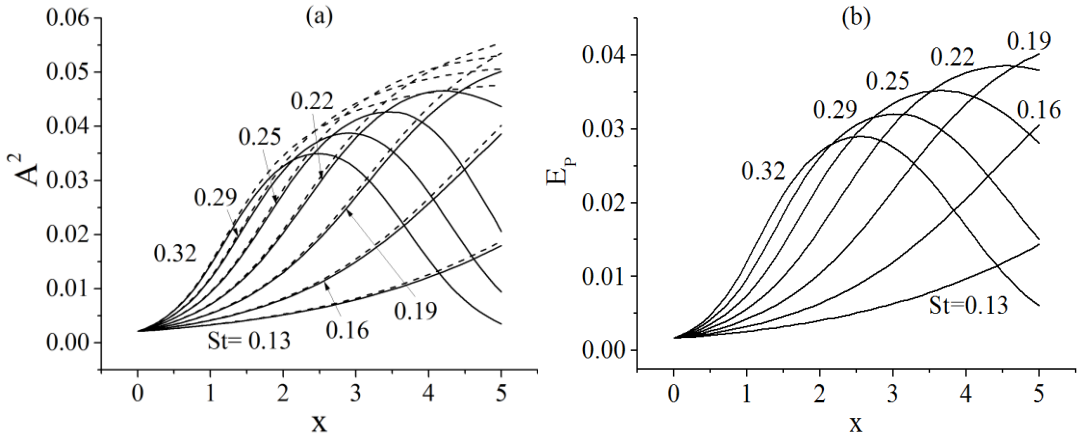

Figure 7.4 a) The axial variation of square perturbation amplitude (the inviscid limits are presented by dashed lines); b) the axial variation of the kinetic energy flux of the perturbation. The flow conditions are $M_0 = 1.5$, $R_K = 10^{-2}$, $Re_0 = 5 \times 10^4$, and $\theta_0 = 0.025$.

It is interesting to observe from Figure 7.4(a) that $A^2(x)$ increases monotonically with x at $St = 0.13, 0.16$ and 0.19, but it varies non-monotonically with x for $St \geq 0.22$. A similar trend can be observed for the kinetic energy flux in the periodic perturbation, $E_P(x)$, as shown in Figure 7.4(b). To understand these observations, we can rewrite Equation (7.14) as

$$\bar{\rho}_c(x)\bar{u}_c(x)I_P(\theta)\frac{d}{dx}A^2(x) = K - \Phi_P + W + G \tag{7.19}$$

where

$$G = -A^2(x)\frac{d}{dx}[\bar{\rho}_c(x)\bar{u}_c(x)I_P(\theta)] = -A^2(x)\frac{I_P(\theta)}{I_{FB}(\theta)}\frac{dF_B}{dx} \tag{7.20}$$

can be considered as the increase of the perturbation kinetic energy due to the axial increase of the mass flux.

Figure 7.5 shows the four source terms on the RHS of Equation (7.19), which determine the axial variation of the perturbation amplitude. It is seen that the magnitudes of G and W are much smaller than those of K and Φ_P throughout the computational domain, incidating that the latter two are dominant. As shown in Figure 7.5(a), the kinetic energy transfer rate K from the base flow to the perturbation is

always positive, serving as a source for the growth of the perturbation amplitude. The non-monotonic variation of K along the axial coordinate can be understood as follows. The increase of K is due to the increase of the magnitude of $\overline{u'v'}$ as the result of the energy conversion from the base flow to the perturbation. The downstream decrease of K is caused by the decrease of $d\bar{u}/dr$ as the result of the radial spreading of the jet flow[52]. Such a non-monotonic spatial variation of K is independent of the viscous dissipation, as substantiated by the fact that the same trend holds for the inviscid limits as shown in Figure 7.5(a). It is noted that the downstream decrease of K is not manifest for low-frequency perturbations, such as $St = 0.13$, because the markedly slow jet growth needs a longer axial distance to take effect.

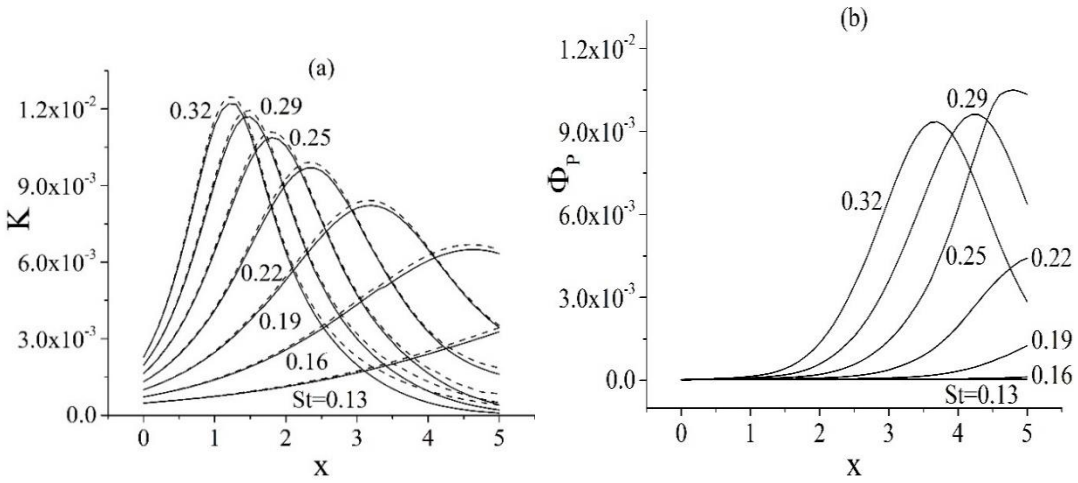

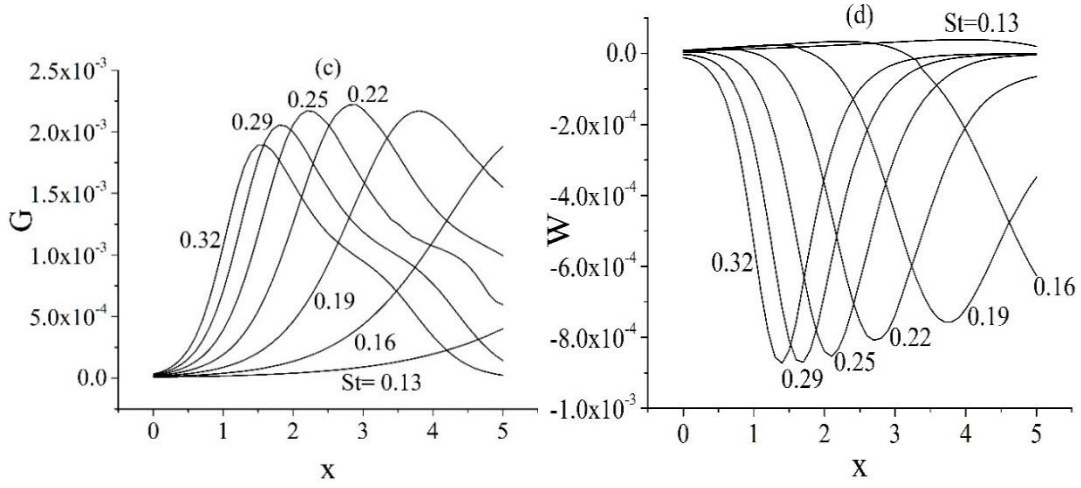

Figure 7.5 a) The kinetic energy transfer rate from the base flow to the perturbation (the inviscid limits are presented in dashed lines); b) the viscous dissipation rate in the perturbed flow; c) the growth of perturbation amplitude caused by the increase of mass flux; d) the power of the perturbation pressure. The flow conditions are $M_0 = 1.5$, $R_K = 10^{-2}$, $Re_0 = 5 \times 10^4$, and $\theta_0 = 0.025$.

The viscous dissipation Φ_P of the perturbed flow increases along the axial direction and exceeds K at a certain downstream location, accordingly causing the perturbation amplitude to decay. Compared with Φ_B that decreases with increasing Re_0, Φ_P also depends on the frequency and amplitude of the periodic perturbation. As a result, Φ_P may be significant even at high Re_0, especially for the periodic perturbations with high frequencies as shown in Figure 7.5(b). Consequently, the viscous dissipation increases with St, and the perturbation amplitude starts to decay at farther upstream location as St increases.

Figure 7.5(a) shows the monotonic increasing of $\theta(x)$ owing to the radial spreading of the shear layer. Again, $\theta(x)$, being linearly proportional to the shear layer thickness, reaches its maximum value at $x = 5$, which is below the threshold value of $\theta = 0.25$, verifying the applicability of the velocity profile in the considered axial domain. The maximum momentum thickness θ_m is of fundamental importance since it measures the spreading of the shear layer within the potential core. As shown in Figure 7.6(a), the non-monotonic variation of θ_m with St results in an optimal Strouhal number, $St_p = 0.22$, which is central to the present study.

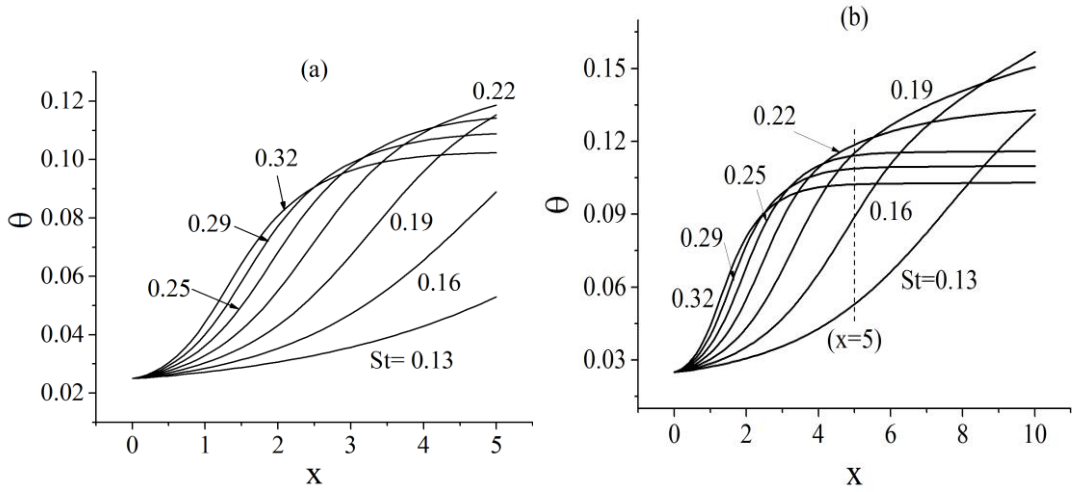

Figure 7.6 a) The axial variation of the momentum thickness of the base flow; b) The dependence of the shear layer growth on the length of the potential core. The flow conditions are $M_0 = 1.5$, $R_K = 10^{-2}$, $Re_0 = 5 \times 10^4$, and $\theta_0 = 0.025$.

We fully recognized that the value of St_p depends on the definition of θ_m[60]. In the previous studies on incompressible jet flows, θ_m was defined at four jet diameters downstream from the jet exit, i.e. $x = 4$. The recent study of Samimy *et al.* [63, 64]

shows that the potential core can be extended to $x = 6{\sim}7$ at higher Mach numbers. In the present study, the end of potential core is fixed at $x = 5$ to ensure $\theta_m \leq 0.25$ for all the Mach numbers of interest. Figure 7.6(b) shows the jet spreading in a potential core which is extended up to $x = 10$. It is seen that the most amplified perturbation depends on the streamwise location as we expected. Specifically, $St_p = 0.22, 0.19$ and 0.16 if θ_m is defined at $x = 5$, 7 and 10, respectively. The observation that jet-preferred mode favors lower frequency excitation for a longer potential core can be understood from the fact that higher frequency perturbations damp at farther upstream locations due to their larger viscous dissipation rates, as demonstrated in Figure 7.6(b). In the present problem, the existence of the non-monotonic variation of θ_m with respect to forcing St does not depend on the length of potential core. Moreover, understanding the dependence of St_p on the controlling parameters, particularly the jet Mach number, is of the primary concern in this study. Consequently, we shall use a fixed domain of consideration starting at $x = 0$ and ending $x = 5$ for the following parametric studies without loss of any generality.

7.5 Parametric dependence of θ_m

The optimal Strouhal number, St_p, can be illustratively identified as the peak point on the $\theta_m - St$ curves under various flow conditions. Several parameters have influence on the variation of θ_m with St, as will be discussed as follows.

First, it is seen in Figure 7.7(a) that the θ_m in low St regime increases with increasing the starting momentum thickness, θ_0, and the trend is opposite in high St regime. To understand this, we note that θ_0 can affect the variation of θ_m by changing the velocity shape function in addition to being the initial condition of θ_m. Specifically, increasing θ_0 reduces the velocity gradient, as shown in Equation (7.7), and therefore suppresses the jet growth by reducing the energy conversion from the base flow to the perturbation. As a result, the increase of θ_m in low St regime is mainly owing to the increase of θ_0 as the jet does not have significant growth by low-frequency excitation. The decrease of θ_m with increasing θ_0 in the high St regime is mainly caused by the suppression of θ_0 on the jet growth through changing the initial velocity gradient. Furthermore, the peaks of θ_m are found to be around $St = 0.22$ for various θ_0 considered and St_p only slightly changes with θ_0. Therefore, we can neglect the influence of θ_0 on St_p in the following discussion by using a fixed typical value of 0.025.

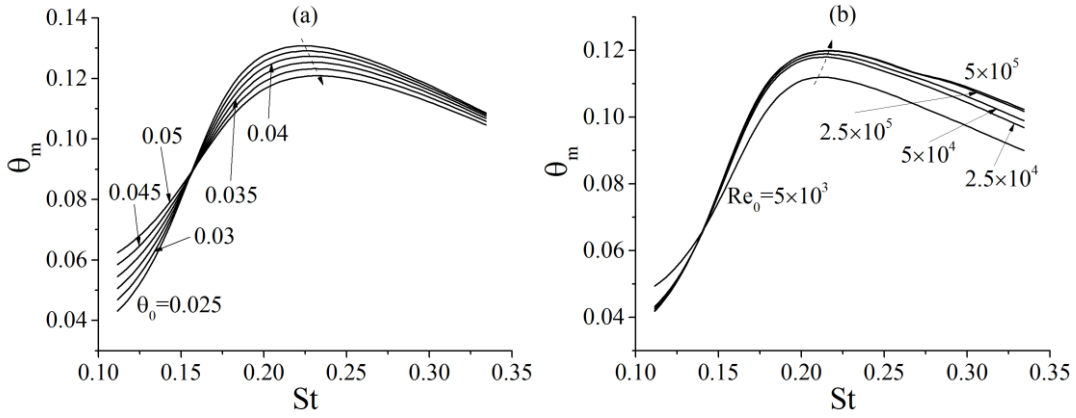

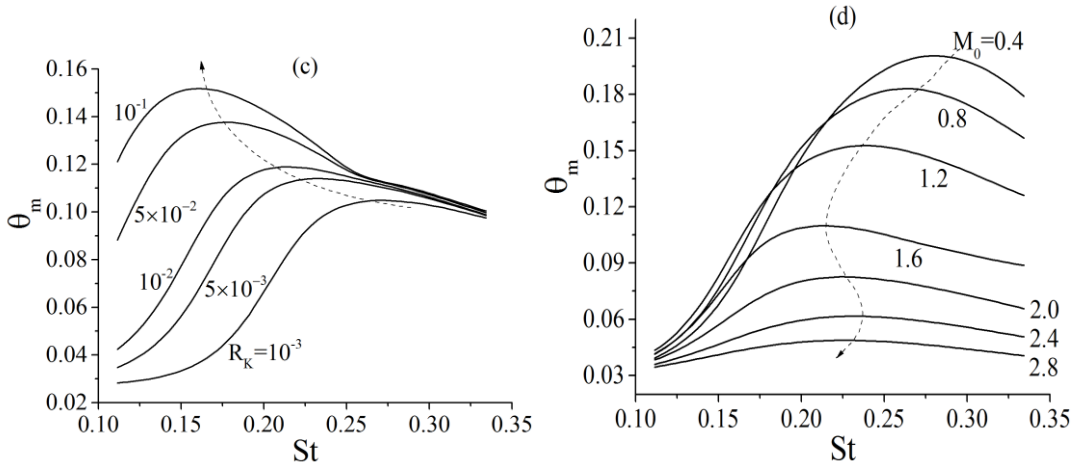

Figure 7.7 a) The Influence of M_0 on shear layer growth, and the flow conditions are s $Re_0 = 5 \times 10^4$, $R_K = 10^{-2}$ and $\theta_0 = 0.025$; b) the influence of Re_0 on shear layer growth, and the flow conditions are $M_0 = 1.5$, $R_K = 10^{-2}$, and $\theta_0 = 0.025$; c) the influence of R_K on shear layer growth, and the flow conditions are $M_0 = 1.5$, $Re = 5 \times 10^4$, and $\theta_0 = 0.025$; d) the influence of θ_0 on shear layer growth, and the flow conditions are $M_0 = 1.5$, $Re = 5 \times 10^4$ and $R_K = 10^{-2}$

Several observations can be made on the influence of Reynolds number Re_0 on St_p, as shown in Figure 7.7(b). First, it is seen that θ_m increases generally with increasing Re_0 from 5×10^3 to 5×10^5 due to the decreasing viscous dissipation in perturbations. Second, the two curves representing $Re_0 = 2.5 \times 10^5$ and $Re_0 = 5 \times 10^5$ are almost identical, implying that the influence of viscous dissipation on θ_m becomes asymptotically negligible as Re_0 increases. Third, St_p increases with Re_0 because the jet growth always prefers high-frequency perturbations for their stronger energy transfer from the base flow, as have shown in Figure 7.5(a), and the decreased viscous dissipation for high-frequency perturbations facilitate this trend. An interesting

observation is that θ_m increases with decreasing Re_0, say, to $Re_0 = 5 \times 10^3$, in the low$-St$ regime. This is because that the jet development at low$-St$ regime is mainly owing to the spreading of the base flow itself, as demonstrated in the preceding section. The base flow can grow even without the external excitation, as shown in Figure 7.8(a), although the growth rate is significantly smaller than that with external excitation. The viscous dissipation in the base flow becomes increasingly non-negligible with decreasing Re_0 and can be comparable with that in the low-frequency perturbation. The facilitation of the viscous dissipation on the base flow development is clearly seen in Figure 7.8(b).

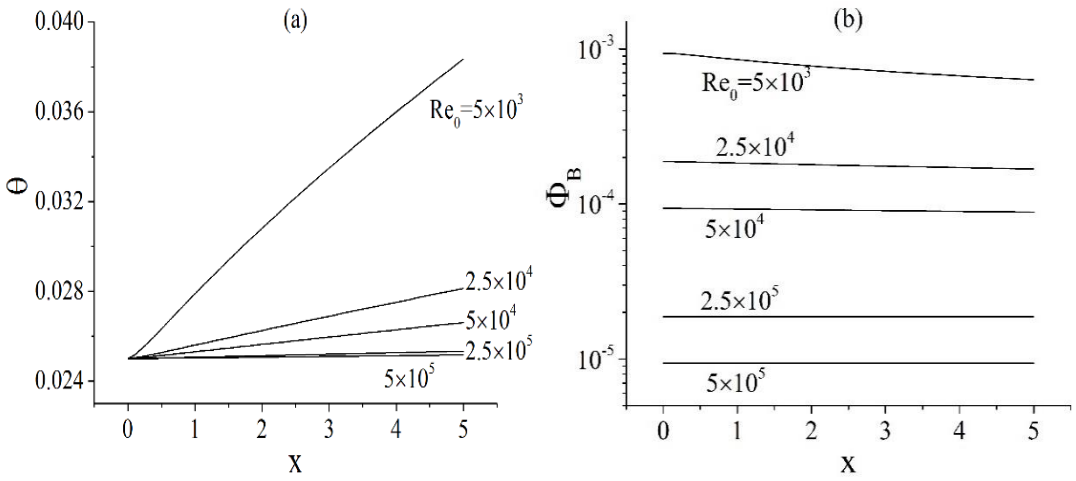

Figure 7.8 a) The shear layer growth; b) the viscous dissipation of the unperturbed base flow. The flow conditions are $M_0 = 1.5$ and $\theta_0 = 0.025$.

Figure 7.7(c) shows that the increase of θ_m with R_K is not uniform for all St, as such θ_m prefers low-frequency perturbations as increasing R_K, leading to the shift of St_p to the lower values. This can be understood by noting that both K and Φ_p are

linear proportional to R_K through the quadratic terms of perturbation. The increase of K with R_K explains the increase of θ_m over the entire spectrum of St of interest, while the significant suppression of Φ_p on high-frequency perturbation leads to the jet growth prefers low St.

The influence of M_0 on the jet development is shown in Figure 7.7(d). It is seen that θ_m decreases significantly with increasing M_0, owing to the increasing compressibility as discussed in the introduction. Interestingly, St_p shows a non-monotonic variation with increasing M_0 from 0.4 to 2.8. This interesting observation has not been reported in previous studies and will be discussed in detail in the remaining text.

Chapter VIII Non-monotonic Variation of St_p with M_0

8.1 Physical interpretation

The non-monotonic variation of St_p with increasing M_0 is shown in Figure 8.1. It is seen that the present theoretical prediction of the optimal Strouhal numbers agree well with the experimental results of Borisov and Gynkina [8, 22].

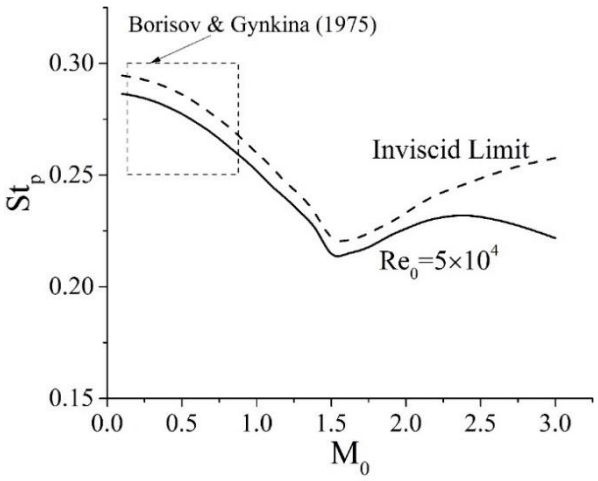

Figure 8.1 The non-monotonic variation of St_p with M_0. The flow conditions are $R_K = 0.01$ and $\theta_0 = 0.025$. The square enclosed by dashed lines represents the ranges of St_p and M_0 in the experiment of Borisov and Gynkina [8, 22].

In the inviscid limit, St_p decreases and then increase with increasing M_0, resulting in a turning point located around $M_0 = 1.5$. With the viscous dissipation effects being considered, the $St_p - M_0$ curve shifts to lower St_p as discussed in the preceding section. The comparison between the $St_p - M_0$ curves under inviscid and viscous situations suggests that the decrease of St_p in the high M_0 regime, which results in the second turning point located around $M_0 = 2.4$, should be attributed to the significant viscous dissipation, which however cannot be the cause for the first turning point.

To understand the first turning point of the $St_p - M_0$ curve, one should first note that θ_m is the result of the continuous growth of momentum thickness of shear layer $\theta(x)$ from the jet exit to the end of the potential core. Consequently, the non-

monotonic variation of St_p with M_0 should be attributed to the accumulative energy transfer from the base flow to the perturbation within the potential core. To verify this hypothesis, we defined the stream-wise integration of K by

$$\begin{aligned} K_{tot} &= \int_0^{x_m} K dx \\ &\approx -2\pi \int_0^{x_m} \bar{\rho}_c \bar{u}_c A^2 \alpha_i \int_0^{\infty} \frac{\bar{u}_s(r;\theta)}{\bar{\rho}_s(r;\theta)} \left| \frac{1}{\alpha \bar{u}_s - \omega} \right|^4 \\ &\times \left(\frac{d\bar{u}_s(r;\theta)}{dr} \right)^2 \left| \frac{d\hat{p}(r;\theta)}{dr} \right|^2 r dr dx \end{aligned} \tag{8.1}$$

To derive this equation, we have used the definition of K, (A5) and (A6), and neglected the second term $\alpha\hat{p}$ in the bracket of (A5) which is substantially smaller than the first term. As shown in Figure 8.2 (a) and (b), the variation of θ_m with St and M_0 is almost identical with that of K_{tot}, substantiating our hypothesis that K_{tot} is the dominant factor causing the first turning point of the $St_p - M_0$ curve, on which the viscous dissipation has negligible influence.

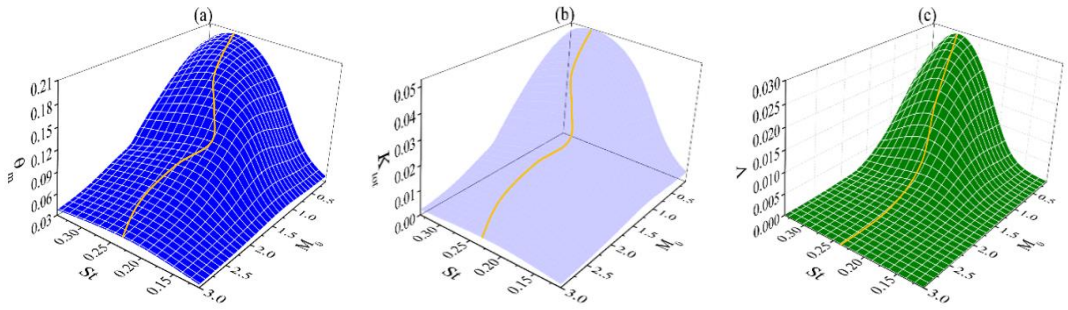

Figure 8.2 The variation of θ_m (a), K_{tot} (b), and Λ (c) with respect to St and M_0 under the flow conditions of $R_K = 10^{-2}$, $Re_0 = 5 \times 10^4$. The maxima θ_m, K_{tot}, and Λ corresponding to fixed Mach numbers are indicated by the highlighted solid line.

To further unveil the role of K_{tot}, we first noted that $\bar{\rho}_c$, $\bar{u}_c$ and A^2 are slow variables with respect to x according to the results shown in the preceding section. The other flow variables such as $\bar{u}_s(r;\theta)$, $\bar{\rho}_s(r;\theta)$ and $\hat{p}(r;\theta)$ are weak functions of x through the low-varying $\theta(x)$. In addition, $\alpha\bar{u}_s - \omega = \omega(\bar{u}_s/u_p - 1)$ is also slow-varying since the frequency ω of interest varies in a relatively narrow range and the phase velocity u_p therefore remains approximately constant in the present problem[52]. Consequently, we further assume that the axial variation of K_{tot} is controlled by the α_i, the imaginary part of the complex wave number α and hence have

$$K_{tot} \sim -\int_0^{x_m} \alpha_i dx = \Lambda \tag{8.2}$$

This assumption is verified by observing that Λ has the same order of magnitude with K_{tot} and that the variation of Λ with St and M_0 is almost identical to that of K_{tot}, as shown in Figure 8.2(c).

As the local growth rate of perturbation per unit amplitude, $-\alpha_i$ measures the capacity of periodic perturbation in receiving the kinetic energy from the base flow. Consequently, Λ measures the cumulative effect of the energy conversion in the

potential core. As shown in Figure 8.2(c), Λ of high St decreases much more rapidly with increasing M_0 than that of low St, implying the increased compressibility suppresses higher-frequency perturbations more substantial than the lower-frequency ones. This observation is in accordance with the previous result on the linear instability analysis of compressible jets that the wave number is not sensitive to the variation of M_0 in low St regime [31, 52]. Owing to the non-uniform suppression, the jet spreading prefers low-frequency modes and hence St_p decreases with increasing M_0 from zero to the first turning point around $M_0 = 1.5$. As further increasing M_0, St_p increases again because all the perturbations are substantially suppressed by compressibility and therefore the jet spreading prefers higher-frequency perturbations due to their larger growth rates, as discussed in the preceding section.

8.2 Influence of Reynolds number on optimal frequency

In Section 8.1, we have demonstrated that the second turning point on the $St_p - M_0$ curve can be attributed to the viscous dissipation, as shown in Figure 8.1 that such a turning point is absent on the curve corresponding to the inviscid limits. To further investigate the influence of viscosity on our results, we first show the $St_p - M_0$ curves for various Re_0, which signifies the viscous dissipation in the perturbed jet flow.

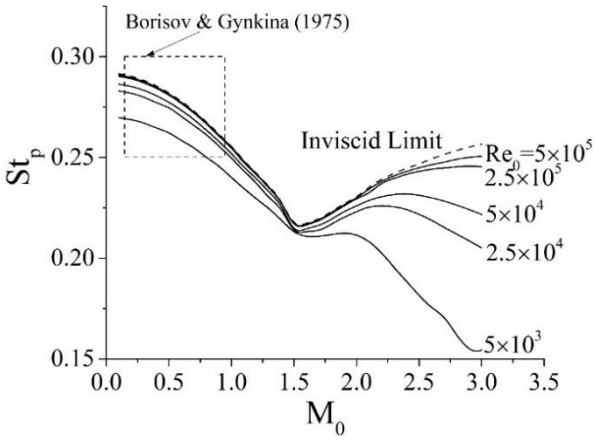

Figure 8.3 The influence of Re_0 on the variation of St_p with M_0. $R_K = 0.01$ for the all curves. The square enclosed by dashed lines represents the range of optimal Strouhal numbers in the experimental investigation of Borisov and Gynkina[8, 22].

As seen in Figure 8.3, the decrease of Re_0 and hence the increase of viscous dissipation does not cause qualitative changes to the $St_p - M_0$ curves at relatively low M_0. This implies the decrease and then increase of St_p with M_0, yielding the first turning point, is not attributed to the viscous dissipation as we have discussed in Section 4.4.1. Furthermore, the viscous dissipation has significant influence on the $St_p - M_0$ curves at relatively high M_0, as such it causes St_p to decrease again as Re_0 decreases to below 5×10^4, yielding the second turning point. The suppression of the viscous dissipation on the high-frequency perturbations is so strong that St_p almost monotonically decreases with M_0 as Re_0 decreases to 5×10^3, resulting in the absence of the two turning points.

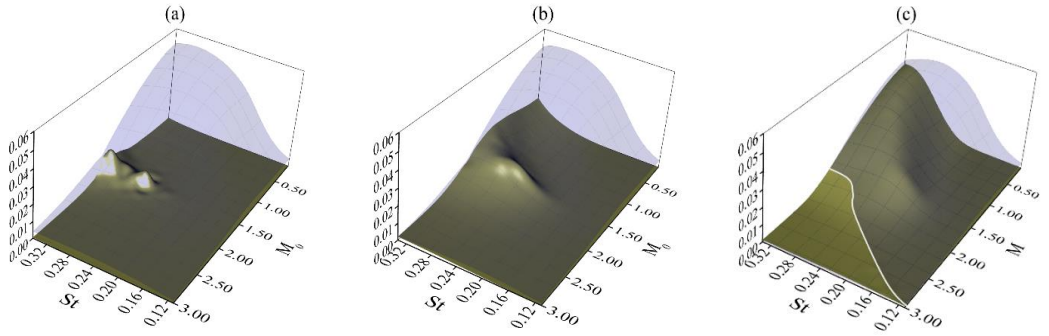

Figure 8.4 The distribution of K_{tot} (transparent blue surface) and Φ_{tot} (yellow surface) in the $St - M_0$ space. The conditions are given as a) $Re_0 = 5 \times 10^5$, $R_K = 10^{-2}$; (b) $Re_0 = 5 \times 10^4$, $R_K = 10^{-2}$; (c) $Re_0 = 5 \times 10^3$, $R_K = 10^{-2}$. The intersecting line of K_{tot} and Φ_{tot} is highlighted in (c).

The competition between the energy transfer and the viscous dissipation of the periodic perturbation on affecting the jet development is illustrated in Figure 8.4, where K_{tot} and the stream-wise integration of the viscous dissipation in perturbation, defined by

$$\Phi_{tot} = \int_0^{x_m} \Phi_P \, dx \tag{8.3}$$

are plotted as functions of the St and M_0 for three typical values of Re_0. The viscous dissipation in the base flow Φ_B is negligible since it is always at least one order of magnitude smaller than Φ_P. For the relatively high $Re_0 = 5 \times 10^5$, the K_{tot} surface is always above the Φ_{tot} surface over the entire $St - M_0$ domain of interest, indicating K_{tot} is the dominant factor in determining the non-monotonic variation of St_p. This is qualitatively identical to that of the inviscid limit, as shown in Figure 8.3.

For an intermediate $Re_0 = 5 \times 10^4$, Φ_{tot} becomes comparable with K_{tot} around $M_0 = 2.0$, resulting the emergence of the second turning point. For sufficiently low $Re_0 = 5 \times 10^3$, Φ_{tot} is comparable with K_{tot} in the entire $St - M_0$ domain and exceeds K_{tot} in the high-St and high M_0 regime. As a result, St_p decreases monotonically with increasing M_0 in the entire M_0 range of interest.

8.3 Influence of forcing amplitude on optimal frequency

The input kinetic energy R_K, which is proportional to the square of initial amplitude, A_0^2, of the periodic perturbation and measures the capability of the perturbation in changing the base flow, also plays an important role in determining St_p, as both K and Φ_P are linear functions of the square of perturbation amplitude A^2. It is shown in Figure 8.5 that the $St_P - M_0$ curves moves to smaller St_P as increasing R_K. This is because the development of all the perturbations can be promoted by the increase of K, but the increase of Φ_P suppresses the high-frequency perturbations more significantly than the low-frequency ones, rendering the jet development prefers lower-frequency perturbations as have been discussed in Section 7.5.

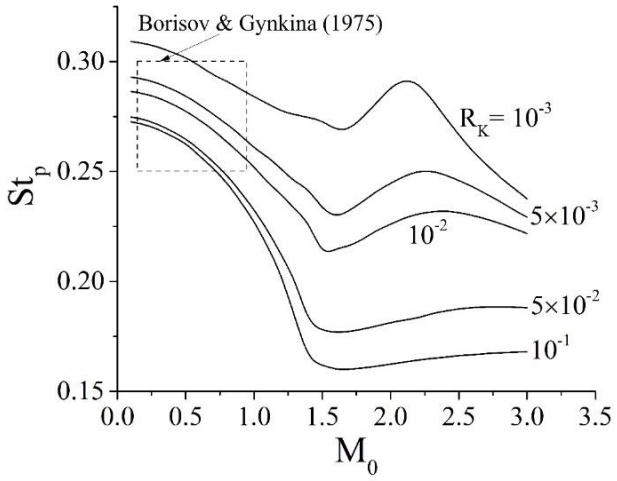

Figure 8.5 The influence of kinetic energy ratio R_K on the distribution of St_p to M_0, the Reynolds number is fixed as $Re = 5 \times 10^4$ for all curves. The square enclosed by dashed lines represents the range of optimal Strouhal numbers in the experimental investigation of Borisov and Gynkina[8, 22].

It is further seen that the variation of St_P with M_0 shows the non-monotonic behavior and has two turning points for relatively small R_K, such as 1×10^{-3} and 1×10^{-2}, but the second turning point is absent for larger R_K, such as 1×10^{-1}. This again can be understood by examining the variations of K_{tot} and Φ_{tot} with St and M_0 for different R_K, as shown in Figure 8.6. For relatively small $R_K = 1 \times 10^{-3}$, the surface representing K_{tot} is always above that of Φ_{tot}, implying the non-monotonic variation of St_P with M_0 is dominantly controlled by K_{tot}, which has been discussed in the Section 4.4.1. By the same token, the same non-monotonic behavior of the $St_P - M_0$ curve corresponding to $R_K = 1 \times 10^{-2}$ is still present although the second turning point is not as prominent as that for smaller R_K. As further increasing R_K to 1×10^{-1}, the Φ_{tot} surface is above the K_{tot} surface in the high St regime for

relatively large M_0. As the result, only those low-frequency perturbations can develop and St_P slightly increases with M_0, as shown in Figure 8.6.

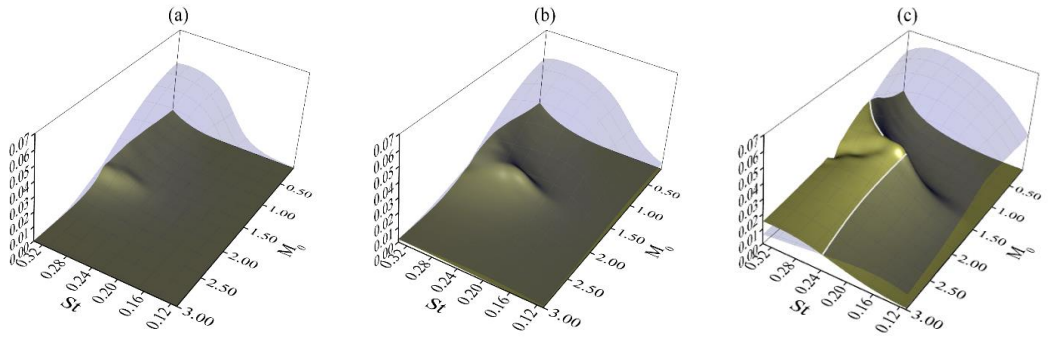

Figure 8.6 The distribution of K_{tot} (transparent blue surface) and Φ_{tot} (solid yellow surface) in the $St - M_0$ space. The flow conditions are given as a) $R_K = 10^{-3}$, $Re_0 = 5 \times 10^4$; b) $R_K = 10^{-2}$, $Re_0 = 5 \times 10^4$; c) $R_K = 10^{-1}$, $Re_0 = 5 \times 10^4$. The intersecting line of K_{tot} and Φ_{tot} is highlighted in (c).

8.4 Influence of potential core length of optimal frequency

Although the influence of the length of potential core on the jet development has been discussed in Section 7.4 and a fixed potential core between $x = 0$ and $x = 5$ was adopted throughout the above discussion, it is of interest to examine again its influence on the $St_P - M_0$ curves, as shown in Figure 8.7. It is seen that increasing the length of potential core will cause the $St_P - M_0$ curve moves downwards in St_P because the low-frequency perturbations subject to relatively smaller viscous dissipation rate can grow up eventually, given a sufficiently long potential core. This

result is in consistent with the axial variation of the momentum thickness shown in Figure 7.6(b). However, the present result on the non-monotonic variation of St_P with M_0 should hold in general since the shape the $St_P - M_0$ curve is not qualitatively affected by the length of the potential core, as seen in Figure 8.7.

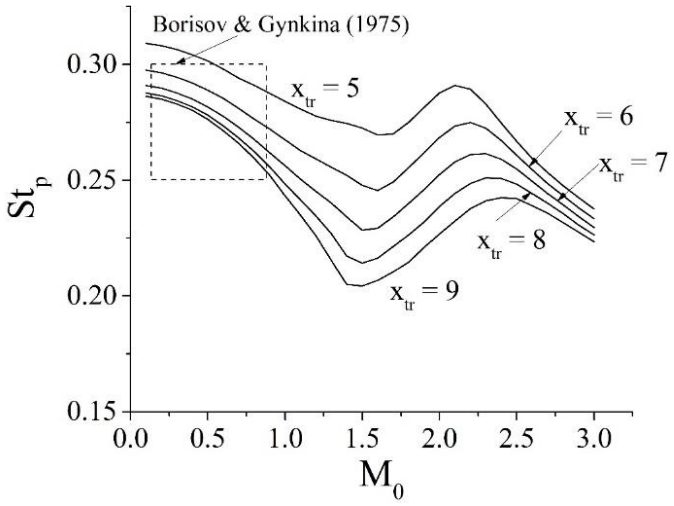

Figure 8.7 The dependence of St_p on the length of the potential core, and the flow conditions are $R_K = 10^{-3}$, $Re_0 = 5 \times 10^4$, and $\theta_0 = 0.025$. The square enclosed by dashed lines represents the range of optimal Strouhal numbers in the experimental investigation of Borisov and Gynkina[8, 22].

Chapter IX Concluding Remarks

The optimal Strouhal number of compressible circular jets undergoing periodic, axisymmetric perturbations of real frequency at the jet exit was analytically studied by using the energy integral method, in which the jet response system can be described by a set of coupled ODEs governing the amplitude of perturbation, the momentum thickness, the centerline velocity and density (or temperature) of the mean jet flow.

The most interesting and physically significant result is that the optimal Strouhal number, St_p, corresponding to which the momentum thickness has the largest growth at end of the potential core of the jet flow, was found to vary non-monotonically with the jet Mach number M_0 in the range of 0~3. In the relatively low-M_0 regime, the suppression of the flow compressibility on the growth of shear layer is stronger for high-frequency forced perturbation than for low-frequency, resulting in the decrease of St_p with increasing M_0. The suppression becomes "saturated" to all the perturbations in the intermediate-M_0 regime and therefore St_p starts to increase with M_0, owing to the emergence of compressibility suppressing effect on the growth of low frequency perturbations. In the relatively high-M_0 regime, the decrease of St_p is mainly attributed to the viscous dissipation, which damps the high-frequency perturbations more significantly than low-frequency ones.

The present analysis further showed that the starting momentum thickness of the jet flow has negligible influence on the non-monotonic variation of St_p with M_0, but

the Reynolds number, Re_0, and the input perturbation energy (or starting amplitude of perturbation), R_K, can modify the $St_p - M_0$ variation significantly. Specifically, increasing Re_0 hence decreasing viscous dissipation not only results in smaller St_p but also gradually weakens the non-monotonicity of the $St_p - M_0$ curves. Increasing R_K promotes the growth of all the perturbations however the simultaneously enhanced viscous dissipation suppresses the growth of high-frequency perturbations. As a result, St_p generally decreases with increasing R_K. Although the present analysis agrees well with available albeit limited experimental results, the observed non-monotonic variation of St_p with M_0 requires further experimental validation.

Future Work

For circulation-controlled firewhirls, we suggest analyzing the firewhirls in confined environment, i.e., being enclosed by side walls, especially when the wall-to-pan size ratio becomes insufficient large. Moreover, a small wall-to-pan size ratio results in more heat loss from the flame, which in turn affects the flame characteristics, e.g., temperature and contour, therefore, the considerations of finite-rate flame chemistry and heat loss mechanism, e.g., radiation, become necessary. Besides, the confined environments also restricts the application of Burgers and even the generalized-power law vortex must be reexamined, and the appropriate vortex model needs to be developed.

For spreading of periodically-forced jet, we expect to analyze the effect forcing with multiple frequencies, and investigate the interactions between various perturbation modes, and their overall effects on mean jet flow. Besides, a more physically accurate, triple-decomposition can be adopted in future study to take turbulence into consideration.

Appendix A

The non-dimensional governing equation for the coupling function β_F in physical coordinates can be expressed as

$$\tilde{\rho}\tilde{u}\frac{\partial \beta_F}{\partial \tilde{x}} + \tilde{\rho}\tilde{v}\frac{\partial \beta_F}{\partial \tilde{r}} = \frac{1}{Pe}\frac{\partial}{\partial \tilde{x}}\left(\tilde{\rho}\widetilde{D}_F\frac{\partial \beta_F}{\partial \tilde{x}}\right) + \frac{1}{Pe}\frac{1}{\tilde{r}}\frac{\partial}{\partial \tilde{r}}\left(\tilde{\rho}\widetilde{D}_F\tilde{r}\frac{\partial \beta_F}{\partial \tilde{r}}\right) \tag{A1}$$

We applied a density-mass-diffusivity-weighted coordinate transformation (3.9) to Equation (A1) and obtained the following spatial derivatives

$$\tilde{\rho}\tilde{u}\frac{\partial}{\partial \tilde{x}} = \frac{1}{Pe}\tilde{\rho}^3\widetilde{D}_F\tilde{u}\left(2\frac{\partial}{\partial \xi} + 2h\frac{\partial}{\partial \eta}\right) \tag{A2}$$

$$\tilde{\rho}\tilde{v}\frac{\partial}{\partial \tilde{r}} = \frac{1}{Pe}\tilde{\rho}^3\widetilde{D}_F\tilde{v}\left(2g\frac{\partial}{\partial \xi} + \frac{Pe}{\tilde{\rho}\widetilde{D}_F}\frac{\partial}{\partial \eta}\right) \tag{A3}$$

$$\begin{aligned}\frac{1}{Pe}\frac{\partial}{\partial \tilde{x}}&\left(\tilde{\rho}\widetilde{D}_F\frac{\partial}{\partial \tilde{x}}\right)\\ &= \frac{\tilde{\rho}^3\widetilde{D}_F}{Pe}\frac{4}{Pe^2\tilde{\rho}}\left[\frac{\partial}{\partial \xi}\left(\tilde{\rho}^3\widetilde{D}_F^2\frac{\partial}{\partial \xi}\right) + \frac{\partial}{\partial \xi}\left(\tilde{\rho}^3\widetilde{D}_F^2h\frac{\partial}{\partial \eta}\right)\right.\\ &\left. + h\frac{\partial}{\partial \eta}\left(\tilde{\rho}^3\widetilde{D}_F^2\frac{\partial}{\partial \xi}\right) + h\frac{\partial}{\partial \eta}\left(\tilde{\rho}^3\widetilde{D}_F^2h\frac{\partial}{\partial \eta}\right)\right]\end{aligned} \tag{A4}$$

$$\begin{aligned}\frac{1}{Pe}\frac{1}{\tilde{r}}\frac{\partial}{\partial \tilde{r}}&\left(\tilde{\rho}\widetilde{D}_F\tilde{r}\frac{\partial}{\partial \tilde{r}}\right)\\ &= \frac{\tilde{\rho}^3\widetilde{D}_F}{Pe}\left[\frac{4g}{Pe^2\tilde{\rho}\tilde{r}}\frac{\partial}{\partial \xi}\left(\tilde{\rho}^3\widetilde{D}_F^2\tilde{r}g\frac{\partial}{\partial \xi}\right)\right.\\ &+ \frac{2g}{Pe\tilde{\rho}\tilde{r}}\frac{\partial}{\partial \xi}\left(\tilde{\rho}^2\widetilde{D}_F\tilde{r}\frac{\partial}{\partial \eta}\right) + \frac{2}{Pe\tilde{\rho}^2\widetilde{D}_F\tilde{r}}\frac{\partial}{\partial \eta}\left(\tilde{\rho}^3\widetilde{D}_F^2\tilde{r}g\frac{\partial}{\partial \xi}\right)\\ &\left. + \frac{1}{\tilde{\rho}^2\widetilde{D}_F\tilde{r}}\frac{\partial}{\partial \eta}\left(\tilde{\rho}^2\widetilde{D}_F\tilde{r}\frac{\partial}{\partial \eta}\right)\right]\end{aligned} \tag{A5}$$

where

$$h(\tilde{x},\tilde{r}) = \frac{Pe}{2\tilde{\rho}^2\widetilde{D}_F}\int_0^{\tilde{r}} \frac{\partial\tilde{\rho}}{\partial\tilde{x}}dr' \tag{A6}$$

and

$$g(\tilde{x},\tilde{r}) = \frac{1}{\tilde{\rho}^2\widetilde{D}_F}\int_0^{\tilde{x}} \frac{\partial}{\partial\tilde{r}}\left(\tilde{\rho}^2\widetilde{D}_F\right)dx' \tag{A7}$$

Substituting Equations (A2)-(A5) into Equation (A1), cancelling out the common term $\tilde{\rho}^3\widetilde{D}_F/Pe$, and denoting

$$\hat{u} = 2\tilde{u} + 2g\tilde{v} \tag{A8}$$

and

$$\hat{v} = 2h\tilde{u} + \frac{Pe\tilde{v}}{\tilde{\rho}\widetilde{D}_F} \tag{A9}$$

we have Equation (3.10):

$$\begin{aligned}\hat{u}\frac{\partial\beta_F}{\partial\xi} + \hat{v}\frac{\partial\beta_F}{\partial\eta} = {} & \frac{4}{Pe^2}\frac{1}{\tilde{\rho}}\left(\frac{\partial}{\partial\xi} + h\frac{\partial}{\partial\eta}\right)\left[\tilde{\rho}^3\widetilde{D}_F^2\left(\frac{\partial\beta_F}{\partial\xi} + h\frac{\partial\beta_F}{\partial\eta}\right)\right] \\ & + \left(\frac{2}{Pe}\frac{g}{\tilde{\rho}\tilde{r}}\frac{\partial}{\partial\xi} + \frac{1}{\tilde{\rho}^2\widetilde{D}_F\tilde{r}}\frac{\partial}{\partial\eta}\right)\left(\frac{2\tilde{\rho}^3\widetilde{D}_F^2 g\tilde{r}}{Pe}\frac{\partial\beta_F}{\partial\xi}\right. \\ & \left. + \tilde{\rho}^2\widetilde{D}_F\tilde{r}\frac{\partial\beta_F}{\partial\eta}\right)\end{aligned} \tag{A10}$$

The derivation of the transport equation for the coupling function β_O is almost the same, except all the diffusion terms on the RHS must be divided by the constant α_D, giving Equation (3.11).

Appendix B

According to Equations (3.12) and (3.13) the velocity components in physical coordinates can be transformed to $\tilde{u}$ and $\tilde{v}$ in the $\xi - \eta$ coordinates:

$$\tilde{u} = \frac{\hat{u}Pe/\left(2\tilde{\rho}\widetilde{D}_F\right) - g\hat{v}}{Pe/\left(2\tilde{\rho}\widetilde{D}_F\right) - gh} \tag{B1}$$

$$\tilde{v} = -\frac{\hat{u}h(\tilde{x},\tilde{r}) - \hat{v}}{Pe/\left(2\tilde{\rho}\widetilde{D}_F\right) - gh} \tag{B2}$$

In the power law vortex model, $\hat{u}$ and $\hat{v}$ are expressed by Equations (3.18) and (3.19) generated from the piecewise stream function (3.17). Substituting Equations (3.18) and (3.19) into Equations (B1) and (B2), we obtain the velocity components in physical coordinates:

$$\begin{aligned}\tilde{u} = \Bigg[&\frac{\alpha_{v1}Pe}{2\tilde{\rho}\widetilde{D}_F} s \left(\frac{2}{Pe}\int_0^{\tilde{x}} \tilde{\rho}^2\widetilde{D}_F dx'\right)\left(\int_0^{\tilde{r}} \tilde{\rho}dr'\right)^{\alpha_{v1}-2} \\ &+ g\frac{ds}{d\tilde{x}}\left(\frac{2}{Pe}\int_0^{\tilde{x}} \tilde{\rho}^2\widetilde{D}_F dx'\right)\left(\int_0^{\tilde{r}} \tilde{\rho}dr'\right)^{\alpha_{v1}-1}\Bigg] \\ &\times \left(\frac{Pe}{2\tilde{\rho}\widetilde{D}_F} - gh\right)^{-1}, \qquad \tilde{r} < \tilde{r}_c\end{aligned} \tag{B3}$$

$$\tilde{u} = \left(\int_0^{\tilde{r}_c} \tilde{\rho} dr'\right)^{\alpha_{v1}-\alpha_{v2}} \left[\frac{\alpha_{v2} Pe}{2\tilde{\rho}\widetilde{D}_F} s\left(\frac{2}{Pe}\int_0^{\tilde{x}} \tilde{\rho}^2 \widetilde{D}_F dx'\right)\left(\int_0^{\tilde{r}} \tilde{\rho} dr'\right)^{\alpha_{v2}-2}\right.$$
$$\left. + g\frac{ds}{d\tilde{x}}\left(\frac{2}{Pe}\int_0^{\tilde{x}} \tilde{\rho}^2 \widetilde{D}_F dx'\right)\left(\int_0^{\tilde{r}} \tilde{\rho} dr'\right)^{\alpha_{v2}-1}\right] \qquad \text{(B4)}$$
$$\times \left(\frac{Pe}{2\tilde{\rho}\widetilde{D}_F} - gh\right)^{-1}, \qquad \tilde{r} \geq \tilde{r}_c$$

$$\tilde{v} = \left[\alpha_{v1} hs\left(\frac{2}{Pe}\int_0^{\tilde{x}} \tilde{\rho}^2 \widetilde{D}_F dx'\right)\left(\int_0^{\tilde{r}} \tilde{\rho} dr'\right)^{\alpha_{v1}-2}\right.$$
$$\left. + \frac{ds}{d\tilde{x}}\left(\frac{2}{Pe}\int_0^{\tilde{x}} \tilde{\rho}^2 \widetilde{D}_F dx'\right)\left(\int_0^{\tilde{r}} \tilde{\rho} dr'\right)^{\alpha_{v1}-1}\right] \qquad \text{(B5)}$$
$$\times \left(hg - \frac{Pe}{2\tilde{\rho}\widetilde{D}_F}\right)^{-1}, \qquad \tilde{r} < \tilde{r}_c$$

$$\tilde{v} = \left(\int_0^{\tilde{r}_c} \tilde{\rho} dr'\right)^{\alpha_{v1}-\alpha_{v2}} \left[\alpha_{v2} hs\left(\frac{2}{Pe}\int_0^{\tilde{x}} \tilde{\rho}^2 \widetilde{D}_F dx'\right)\left(\int_0^{\tilde{r}} \tilde{\rho} dr'\right)^{\alpha_{v2}-2}\right.$$
$$\left. + \frac{ds}{d\tilde{x}}\left(\frac{2}{Pe}\int_0^{\tilde{x}} \tilde{\rho}^2 \widetilde{D}_F dx'\right)\left(\int_0^{\tilde{r}} \tilde{\rho} dr'\right)^{\alpha_{v2}-1}\right] \qquad \text{(B6)}$$
$$\times \left(hg - \frac{Pe}{2\tilde{\rho}\widetilde{D}_F}\right)^{-1}, \qquad \tilde{r} \geq \tilde{r}_c$$

It is extremely complex to directly check the consistence of (B3)-(B6) with the continuity equation. We can however readily check it for degenerate situations. Under the situation of constant density and mass diffusivity and for $\alpha_{v1} = \alpha_{v2} = 2$, the velocity components (B3) to (B6) can be written by

$$\tilde{u} = 2s\left(\frac{2\tilde{\rho}^2\widetilde{D}_F\tilde{x}}{Pe}\right) \tag{B7}$$

$$\tilde{v} = -\frac{2\tilde{\rho}^2\widetilde{D}_F}{Pe}\frac{d}{d\tilde{x}}\left[s\left(\frac{2\tilde{\rho}^2\widetilde{D}_F\tilde{x}}{Pe}\right)\right]\tilde{r} \tag{B8}$$

which accords with the Burgers vortex with constant physical properties except that the axial coordinate is stretched by a factor of $2\tilde{\rho}^2\widetilde{D}_F/Pe$ according to the coordinate transformation (3.7). Substituting Equations (B7) and (B8) into the continuity equation with constant density

$$\frac{\partial(\tilde{u}\tilde{r})}{\partial\tilde{x}} + \frac{\partial(\tilde{v}\tilde{r})}{\partial\tilde{r}} = 0 \tag{B9}$$

we can find that the equation holds exactly.

Under the situation of constant density and mass diffusivity but for $\alpha_{v1} = 2$, the flow velocities inside the vortex core are identical to Equations (B7) and (B8), and those outside the vortex core are given by

$$\tilde{u} = \alpha_{v2}s\left(\frac{2\tilde{\rho}^2\widetilde{D}_F\tilde{x}}{Pe}\right)\left(\frac{1}{\tilde{r}_c}\right)^{\alpha_{v2}-2}\tilde{r}^{\alpha_{v2}-2}, \qquad \tilde{r} \geq \tilde{r}_c \tag{B10}$$

$$\tilde{v} = -\frac{2\tilde{\rho}^2\widetilde{D}_F}{Pe}\left(\frac{1}{\tilde{r}_c}\right)^{\alpha_{v2}-2}\frac{d}{d\tilde{x}}\left[s\left(\frac{2\tilde{\rho}^2\widetilde{D}_F\tilde{x}}{Pe}\right)\right]\tilde{r}^{\alpha_{v2}-1}, \qquad \tilde{r} \geq \tilde{r}_c \tag{B11}$$

(B10) and (B11), together with (B7) and (B8), can be regarded as a generalized, nondimensional form of the strong vortex with constant density, which was formulated

by Klimenko [34, 35]. The consistency of these velocity components with Equation (B9) can be readily verified.

Under the situation of slow variation of $\tilde{\rho}^2\widetilde{D}_F$ in radial direction, i.e.,

$$\int_0^{\tilde{x}} \frac{\partial}{\partial \tilde{r}}\left(\tilde{\rho}^2\widetilde{D}_F\right)dx' \approx 0 \tag{B12}$$

and slow variation of $\tilde{\rho}$ in axial direction, i.e.,

$$\int_0^{\tilde{r}} \frac{\partial \tilde{\rho}}{\partial \tilde{x}}dr' \approx 0 \tag{B13}$$

and for $\alpha_{v1} = \alpha_{v2} = 2$, we have

$$\tilde{u} = 2s\left(\frac{2}{Pe}\int_0^{\tilde{x}} \tilde{\rho}^2\widetilde{D}_F dx'\right) \tag{B14}$$

$$\tilde{v} = -\frac{2\tilde{\rho}\widetilde{D}_F}{Pe}\left[\frac{d}{d\tilde{x}}s\left(\frac{2}{Pe}\int_0^{\tilde{x}} \tilde{\rho}^2\widetilde{D}_F dx'\right)\left(\int_0^{\tilde{r}} \tilde{\rho}dr'\right)\right] \tag{B15}$$

which can be regarded as the generalization of the variable-density Burgers vortex model proposed by Yu and Zhang [75] without assuming that the $s(\xi)$ is a linear function of ξ. Because of the variable physical property effects included in Equations (B14) and (B15) in the forms of integration, we have to invoke the additional assumption of constant Chapman-Rubesin-like parameter to satisfy the continuity equation with variable density.

$$\frac{\partial(\tilde{\rho}\tilde{u}\tilde{r})}{\partial\tilde{x}} + \frac{\partial(\tilde{\rho}\tilde{v}\tilde{r})}{\partial\tilde{r}} = 0 \qquad \text{(B16)}$$

Appendix C

To estimate the value of c_F and c_O at the flame height location, we note that they must have the same order of magnitude due to their similar role in the matching solutions. Thus, we can approximately regard them as $c_F \sim c_O \sim c$, which is evaluated explicitly at the flame height location by replacing c_F and c_O by c in Eq. (3.34), yielding

$$c = \frac{4\chi_h \tilde{Y}_{O\infty} + \alpha_D\left(\tilde{T}_0 - \tilde{T}_\infty - \tilde{Y}_{O\infty}\right) - \left(\tilde{Y}_{F0} + \tilde{T}_0 - \tilde{T}_\infty\right)}{(\alpha_D - 1)\left(2\tilde{T}_0 - 2\tilde{T}_\infty - \tilde{Y}_{O\infty} + \tilde{Y}_{F0}\right)} \tag{C1}$$

Since the values of $\tilde{T}_0$ and $\tilde{T}_\infty$, i.e., the temperatures being scaled by q_c/c_p, are much smaller than $\tilde{Y}_{F0}$ and $\tilde{Y}_{O\infty}$, the quantity c can be very well approximated by

$$c \approx \frac{1 - 4\chi_h Z_{st} - (1 - \alpha_D)Z_{st}}{(1 - \alpha_D)(1 - 2Z_{st})} \tag{C2}$$

Recalling that the stoichiometric mixture fraction Z_{st} is a small quantity, α_D is of order of unity, and the combination $4\chi_h Z_{st}$ is of order of unity as well, the quantity c should also be of order unity, i.e.,

$$c \sim O(1) \tag{C3}$$

Appendix D

Applying the differential operator (4.29) to the Green's function (4.36), it gives

$$\begin{aligned}\hat{L}_{\chi,\zeta}G(\chi,\chi',\zeta,\zeta') &= \frac{\partial}{\partial\chi}G(\chi,\chi',\zeta,\zeta') - \frac{1}{\zeta}\frac{\partial}{\partial\zeta}\left(\zeta\frac{\partial}{\partial\zeta}\right)G(\chi,\chi',\zeta,\zeta') \\ &= \delta(\chi-\chi')\int_0^\infty \omega J_0(\omega\zeta')J_0(\omega\zeta)\exp[-\omega^2(\chi-\chi')]d\omega \\ &- H(\chi-\chi')\int_0^\infty \omega^3 J_0(\omega\zeta')J_0(\omega\zeta)\exp[-\omega^2(\chi-\chi')]d\omega \\ &- H(\chi \\ &- \chi')\int_0^\infty \omega J_0(\omega\zeta')\frac{1}{\zeta}\frac{d}{d\zeta}\left[\zeta\frac{d}{d\zeta}J_0(\omega\zeta)\right]\exp[-\omega^2(\chi \\ &- \chi')]d\omega\end{aligned} \tag{D1}$$

Using the property of Bessel function the differential with respect to ζ in the third term on the RHS of equation (D1) becomes

$$\begin{aligned}\frac{1}{\zeta}\frac{d}{d\zeta}\left[\zeta\frac{d}{d\zeta}J_0(\omega\zeta)\right] &= -\frac{1}{\zeta}\frac{d}{d\zeta}[\omega\zeta J_1(\omega\zeta)] \\ &= -\omega^2\frac{1}{\omega\zeta}\frac{d}{d\omega\zeta}[\omega\zeta J_1(\omega\zeta)] = -\omega^2 J_0(\omega\zeta)\end{aligned} \tag{D2}$$

Substitution of (D2) in equation (D1) leads to the cancellation of the second and third term on its RHS, giving

$$\begin{aligned}&\hat{L}_{\chi,\zeta}G(\chi,\chi',\zeta,\zeta') \\ &= \delta(\chi-\chi')\int_0^\infty \omega J_0(\omega\zeta')J_0(\omega\zeta)\exp[-\omega^2(\chi-\chi')]d\omega\end{aligned} \tag{D3}$$

in which the delta function of χ and χ' has been constructed. To investigate the behavior of ζ and ζ' we consider a particular situation of $\chi = \chi'$, in which the integral on the RHS of equation (D3) reduces to[23]

$$\int_0^\infty \omega J_0(\omega\zeta')J_0(\omega\zeta)d\omega = \frac{1}{\zeta'}\delta(\zeta' - \zeta) \tag{D4}$$

where the integral representation of delta function in terms of Bessel functions has been applied[1]. Since the integral element in cylindrical coordinate is $\zeta' d\zeta' d\chi$, by which the $1/\zeta'$ would be canceled, giving the conventional double integration with respect to $\delta(\chi - \chi')$ and $\delta(\zeta - \zeta')$, resulting in unity. Therefore, we have verified that the Green's function $G(\chi, \chi', \zeta, \zeta')$ satisfies equation (4.30).

Appendix E

According to flame sheet formulation, the leading order coupling function β_S^0 is equal to either the leading order Lewis-number-weighted mass fractions of fuel, $\tilde{Y}_F^0/Le_F$ or that of oxidizer with negative sign, $-\tilde{Y}_O^0/Le_O$, respectively in the fuel and oxidizer regions. Consequently, the derivatives in the first order solutions of coupling functions, equations (4.34) and (4.35), can be evaluated as

$$\begin{aligned}\frac{\partial}{\partial\chi'}\tilde{Y}_F^0(\chi', \zeta') = &-Le_F\left(\tilde{Y}_{F0} + \frac{Le_F}{Le_O}\tilde{Y}_{O,\infty}\right) \\ &\times \int_0^\infty \varpi^2 J_0(\varpi\zeta')J_1(\varpi)\exp(-Le_F\varpi^2\chi')d\varpi\end{aligned} \tag{E1}$$

which is nonzero in the volume inside the flame specified by

$$\int_{V_F} (\cdot)\, dV_F = \int_0^{\chi_f} \int_0^{\zeta_f} (\cdot)\zeta' d\zeta' d\chi' \tag{E2}$$

and

$$\begin{aligned} \frac{\partial}{\partial \chi'} \tilde{Y}_O^0(\chi', \zeta') = Le_F \left(\frac{Le_O}{Le_F} \tilde{Y}_{F0} + \tilde{Y}_{O,\infty} \right) \\ \times \int_0^{\infty} \varpi^2 J_0(\varpi \zeta') J_1(\varpi) \exp(-Le_F \varpi^2 \chi') d\varpi \end{aligned} \tag{E3}$$

which is nonzero in the volume outside the flame specified by

$$\int_{V_O} (\cdot)\, dV_O = \int_0^{\chi_f} \int_{\zeta_f}^{\infty} (\cdot)\zeta' d\zeta' d\chi' + \int_{\chi_f}^{\infty} \int_0^{\infty} (\cdot)\zeta' d\zeta' d\chi' \tag{E4}$$

Substitution of the Green's function (4.36) with derivatives of fuel and oxidizer mass fractions evaluated by (E2) and (E4) into first order species-species coupling functions (4.34) and (4.35), noting the nonzero domains of (E2) and (E4), we obtain first order correction of the modified coupling functions

$$\beta_S^1 = \left(\frac{\tilde{Y}_{F0}}{Le_F} + \frac{\tilde{Y}_{O,\infty}}{Le_O} \right) \left[Le_F^2 I_1 + Le_F Le_O \frac{l_O}{l_F} (I_2 + I_3) \right] \tag{E5}$$

$$\beta_T^1 = Le_F^2 \left(\frac{\tilde{Y}_{F0}}{Le_F} + \frac{\tilde{Y}_{O,\infty}}{Le_O} \right) I_1 \tag{E6}$$

where each $I_i, i = 1,2,3$ represents a four-fold integrals defined as

$$I_1 = \int_0^{\chi_f} \int_0^{\zeta_f} H(\chi - \chi') \int_0^{\infty} \omega J_0(\omega\zeta') J_0(\omega\zeta) \exp[-Le_F\omega^2(\chi - \chi')]\, d\omega \times \int_0^{\infty} \varpi^2 J_0(\varpi\zeta') J_1(\varpi) \exp(-Le_F\varpi^2\chi') d\varpi\, \zeta' d\zeta' d\chi' \tag{E7}$$

$$I_2 = \int_0^{\chi_f} \int_{\zeta_f}^{\infty} H(\chi - \chi') \int_0^{\infty} \omega J_0(\omega\zeta') J_0(\omega\zeta) \exp[-Le_F\omega^2(\chi - \chi')] d\omega \times \int_0^{\infty} \varpi^2 J_0(\varpi\zeta') J_1(\varpi) \exp(-Le_F\varpi^2\chi') d\varpi\, \zeta' d\zeta' d\chi' \tag{E8}$$

$$I_3 = \int_{\chi_f}^{\infty} \int_0^{\infty} H(\chi - \chi') \int_0^{\infty} \omega J_0(\omega\zeta') J_0(\omega\zeta) \exp[-Le_F\omega^2(\chi - \chi')] d\omega \times \int_0^{\infty} \varpi^2 J_0(\varpi\zeta') J_1(\varpi) \exp(-Le_F\varpi^2\chi') d\varpi\, \zeta' d\zeta' d\chi' \tag{E9}$$

Utilizing the interchangeability of integration sequence, each of the four-fold integrals can be approximately evaluated, giving the perturbation solutions (4.37) and (4.38), being accurate to the order of $O(l_F)$ or $O(l_O)$.

Appendix F

(Variables are defined according to the nomenclature in Part II)

In a linear stability analysis, an arbitrary perturbation is decomposed into the superposition of Fourier modes as

$$q' = \sum_{\omega,\alpha} \hat{q}(r) \exp(i\alpha x - i\omega t) \tag{F1}$$

Substituting (F1) into the linearized continuity equation, Euler equation and energy conservation equation, one can obtain the Rayleigh equation for the perturbation pressure

$$\frac{d^2\hat{p}}{dr^2} + \left(\frac{1}{r} - \frac{1}{\Omega}\frac{d\Omega}{dr}\right)\frac{d\hat{p}}{dr} - \alpha^2(1 - M^2\Omega)\hat{p} = 0 \tag{F2}$$

where

$$\Omega = \frac{(\bar{u}_s - \omega/\alpha)^2}{\bar{T}_s}$$

The boundary condition at $r = 0$ is given by

$$\frac{d\hat{p}}{dr} = 0 \tag{F3}$$

and at $r = \infty$ by

$$\hat{p} \to 0 \tag{F4}$$

(F2) together with the boundary conditions (F3) and (F4) constitute an eigenvalue problem, which can be solved numerically, e.g. by using the shooting method. The eigenvalue is the complex wave number of the perturbation

$$\alpha = \alpha_r + i\alpha_i$$

whose imaginary part determines the local growth rate of the perturbation, and the eigenfunction is the radial profile of perturbation pressure $\hat{p}$. The perturbation velocities $\hat{u}$ and $\hat{v}$ of the same Fourier mode can be expressed in terms of $\hat{p}$ by

$$\hat{u} = -\frac{1}{\bar{\rho}_s(\bar{u}_s\alpha - \omega)}\left(\frac{d\bar{u}_s}{dr}\frac{d\hat{p}}{dr}\frac{1}{\bar{u}_s\alpha - \omega} + \alpha\hat{p}\right) \tag{F5}$$

$$\hat{v} = \frac{i}{\bar{\rho}_s(\bar{u}_s\alpha - \omega)}\frac{d\hat{p}}{dr} \tag{F6}$$

at the both boundaries of $r = 0$ and $r = \infty$, one has the relation

$$\frac{1}{\Omega}\frac{d\Omega}{dr} \to 0 \tag{F7}$$

so that the Rayleigh can be asymptotically approximated by the modified Bessel equation

$$\frac{d^2\hat{p}}{dr^2} + \frac{1}{r}\frac{d\hat{p}}{dr} - \alpha^2(1 - M^2\Omega)\hat{p} = 0 \tag{F8}$$

The asymptotic solutions of (A8) are

$$\hat{p}(r \to 0) \sim C_1 I_0\left(\alpha\sqrt{1 - M^2\Omega(0)}r\right) \tag{A9}$$

and

$$\hat{p}(r \to \infty) \sim C_2 K_0 \left(\alpha \sqrt{1 - M^2 \Omega(\infty)} r \right) \tag{F10}$$

where I_0 and K_0 are modified Bessel function of first and second kind with zeroth order respectively.

References

1. *NIST Handbook of Mathematical Functions*. 2010: National Institute of Standards and Technology, Cambridge University Press.

2. Anderson, J.D., *Hypersonic and high temperature gas dynamics*. 2000: Aiaa.

3. AshforthFrost, S. and K. Jambunathan, *Effect of nozzle geometry and semi-confinement on the potential core of a turbulent axisymmetric free jet.* International Communications in Heat and Mass Transfer, 1996. **23**(2): p. 155-162.

4. Batchelor, G. and A. Gill, *Analysis of the stability of axisymmetric jets.* Journal of Fluid Mechanics, 1962. **14**(04): p. 529-551.

5. Battaglia, F., et al., *Simulating fire whirls.* Combustion Theory and Modelling, 2000. **4**(2): p. 123-138.

6. Battaglia, F., R.G. Rehm, and H.R. Baum, *The fluid mechanics of fire whirls: An inviscid model.* Physics of Fluids, 2000. **12**(11): p. 2859-2867.

7. Bertin, J.J., *Hypersonic aerothermodynamics*. 1994: AIAA.

8. BORISOV, I. and N. Gynkina, *Acoustic excitation of high-velocity jets.* Soviet Physics-Acoustics, 1975. **21**(3): p. 230-233.

9. Burgers, J.M., *A mathematical model illustrating the theory of turbulence.* Adv. in Appl. Mech., 1948. **1**: p. 171-199.

10. Capone, A., A. Soldati, and G.P. Romano, *Mixing and entrainment in the near field of turbulent round jets.* Experiments in Fluids, 2013. **54**(1).

11. Chuah, K.H. and G. Kushida, *The prediction of flame heights and flame shapes of small fire whirls.* Proceedings of the Combustion Institute, 2007. **31**: p. 2599-2606.

12. Chuah, K.H., K. Kuwana, and K. Saito, *Modeling a fire whirl generated over a 5-cm-diameter methanol pool fire.* Combustion and Flame, 2009. **156**(9): p. 1828-1833.

13. Chuah, K.H., et al., *Inclined fire whirls.* Proceedings of the Combustion Institute, 2011. **33**: p. 2417-2424.

14. Chung, P.M., *Chemically reacting nonequilibrium boundary layers.* Advances in heat transfer, 1965. **2**(1): p. 109-270.

15. Chung, S.H. and C.K. Law, *Burke-Schumann Flame with Streamwise and Preferential Diffusion.* Combustion Science and Technology, 1984. **37**(1-2): p. 21-46.

16. Cohen, J. and I. Wygnanski, *The Evolution of Instabilities in the Axisymmetrical Jet .1. The Linear Growth of Disturbances near the Nozzle.* Journal of Fluid Mechanics, 1987. **176**: p. 191-219.

17. Crow, S.C. and F. Champagne, *Orderly structure in jet turbulence.* Journal of Fluid Mechanics, 1971. **48**(03): p. 547-591.

18. Curran, E. and S. Murthy, *Scramjet propulsion*. Vol. 189. 2000: AIAA.

19. Cussler, E.L., *Diffusion: mass transfer in fluid systems*. 2009: Cambridge University Press.

20. Emmons, H.W.Y., Shuh-Jing. *The fire whirl*. in *Symposium (International) on Combustion*. 1967.

21. Garnaud, X., et al., *The preferred mode of incompressible jets: linear frequency response analysis.* Journal of Fluid Mechanics, 2013. **716**: p. 189-202.

22. Gutmark, E., K. Schadow, and K. Yu, *Mixing enhancement in supersonic free shear flows.* Annual Review of Fluid Mechanics, 1995. **27**(1): p. 375-417.

23. Hassani, S., *Mathematical Physics: A Modern Introduction to Its Foundations*. 2 ed. 2013: Springer International Publishing. XXXI, 1205.

24. Hayashi, Y., et al., *Influence of Vortex Parameters on the Flame Height of a Weak Fire Whirl via Heat Feedback Mechanism.* Journal of Chemical Engineering of Japan, 2013. **46**(10): p. 689-694.

25. Heiser, W.H. and D.T. Pratt, *Hypersonic airbreathing propulsion*. 1994: AIAA.

26. Ho, C.M. and P. Huerre, *Perturbed Free Shear Layers.* Annual Review of Fluid Mechanics, 1984. **16**: p. 365-424.

27. Hu, L.H., et al., *Evolution of heat feedback in medium pool fires with cross air flow and scaling of mass burning flux by a stagnant layer theory solution.* Proceedings of the Combustion Institute, 2015. **35**: p. 2511-2518.

28. Hussain, A. and K. Zaman, *Vortex pairing in a circular jet under controlled excitation. Part 2. Coherent structure dynamics.* Journal of Fluid Mechanics, 1980. **101**(03): p. 493-544.

29. Hussain, A.K.M.F., *Coherent Structures and Turbulence*. Journal of Fluid Mechanics, 1986. **173**: p. 303-356.

30. Hussain, A.K.M.F. and K.B.M.Q. Zaman, *The Preferred Mode of the Axisymmetric Jet.* Journal of Fluid Mechanics, 1981. **110**(Sep): p. 39-71.

31. Jackson, T.L. and C.E. Grosch, *Inviscid Spatial Stability of a Compressible Mixing Layer.* Journal of Fluid Mechanics, 1989. **208**: p. 609-637.

32. Kamran, M.A. and J.J. McGuirk, *Unsteady Predictions of Mixing Enhancement with Steady and Pulsed Control Jets.* Aiaa Journal, 2015. **53**(5): p. 1262-1276.

33. Klimenko, A.Y., *Moderately strong vorticity in a bathtub-type flow*. Theoretical and Computational Fluid Dynamics, 2001. **14**(4): p. 243-257.

34. Klimenko, A.Y., *Strong swirl approximation and intensive vortices in the atmosphere.* Journal of Fluid Mechanics, 2014. **738**: p. 268-298.

35. Klimenko, A.Y. and F.A. Williams, *On the flame length in firewhirls with strong vorticity.* Combustion and Flame, 2013. **160**(2): p. 335-339.

36. Kuwana, K., et al., *The burning rate's effect on the flame length of weak fire whirls.* Proceedings of the Combustion Institute, 2011. **33**: p. 2425-2432.

37. Kuwana, K., et al., *Scale-model experiments of moving fire whirl over a line fire.* Proceedings of the Combustion Institute, 2013. **34**: p. 2625-2631.

38. Kuwana, K., et al., *Can we predict the occurrence of extreme fire whirls?* AIAA Journal, 2007. **45**(1): p. 16-19.

39. Kuwana, K., et al., *Scaling fire whirls.* Fire Safety Journal, 2008. **43**(4): p. 252-257.

40. Law, C.K., *Combustion Physics*. 2006: Cambridge University Press.

41. Lei, J., N. Liu, and K. Satoh, *Buoyant pool fires under imposed circulations before the formation of fire whirls.* Proceedings of the Combustion Institute, 2015. **35**: p. 2503-2510.

42. Lei, J., et al., *Temperature, velocity and air entrainment of fire whirl plume: A comprehensive experimental investigation.* Combustion and Flame, 2015. **162**(3): p. 745-758.

43. Lei, J.A., et al., *Experimental research on combustion dynamics of medium-scale fire whirl.* Proceedings of the Combustion Institute, 2011. **33**: p. 2407-2415.

44. Lesshafft, L. and P. Huerre, *Linear impulse response in hot round jets.* Physics of Fluids, 2007. **19**(2).

45. Li, F. and M.R. Malik, *On the nature of PSE approximation.* Theoretical and Computational Fluid Dynamics, 1996. **8**(4): p. 253-273.

46. Liu, J., *Nonlinear development of an instability wave in a turbulent wake.* Physics of Fluids (1958-1988), 1971. **14**(11): p. 2251-2257.

47. Liu, J. and L. Lees, *Finite-Amplitude Instability of the Compressible Laminar Wake. Strongly Amplified Disturbances.* Physics of Fluids, 1970. **13**(12): p. 2932-2938.

48. Malik, M.R. and C.L. Chang, *Nonparallel and nonlinear stability of supersonic jet flow.* Computers & Fluids, 2000. **29**(3): p. 327-365.

49. Mankbadi, R.R., *The Mechanism of Mixing Enhancement and Suppression in a Circular Jet under Excitation Conditions.* Physics of Fluids, 1985. **28**(7): p. 2062-2074.

50. Mastorakos, E., M. Shibasaki, and K. Hishida, *Mixing enhancement in axisymmetric turbulent isothermal and buoyant jets.* Experiments in Fluids, 1996. **20**(4): p. 279-290.

51. Matting, F.W., *General solution of the laminar compressible boundary layer in the stagnation region of blunt bodies in axisymmetric flow.* 1964.

52. Michalke, A., *Survey on jet instability theory.* Progress in Aerospace Sciences, 1984. **21**: p. 159-199.

53. Morris, P., *Flow characteristics of the large scale wave-like structure of a supersonic round jet.* Journal of Sound and Vibration, 1977. **53**(2): p. 223-244.

54. Morris, P.J., *Viscous Stability of Compressible Axisymmetric Jets.* Aiaa Journal, 1983. **21**(4): p. 481-482.

55. Nayfeh, A.H., *Introduction to perturbation techniques*. 2011: John Wiley & Sons.

56. Nichols, J.W. and S.K. Lele, *Global modes and transient response of a cold supersonic jet.* Journal of Fluid Mechanics, 2011. **669**: p. 225-241.

57. Or, C.M., K.M. Lam, and P. Liu, *Potential core lengths of round jets in stagnant and moving environments.* Journal of Hydro-Environment Research, 2011. **5**(2): p. 81-91.

58. Pack, L.G. and A. Seifert, *Periodic excitation for jet vectoring and enhanced spreading.* Journal of Aircraft, 2001. **38**(3): p. 486-495.

59. Peters, N., *Turbulent combustion*. 2000: Cambridge University Press.

60. Petersen, R.A. and M.M. Samet, *On the Preferred Mode of Jet Instability.* Journal of Fluid Mechanics, 1988. **194**: p. 153-173.

61. Roper, F., *The prediction of laminar jet diffusion flame sizes: Part I. Theoretical model.* Combustion and Flame, 1977. **29**: p. 219-226.

62. Saffman, P.G., *Vortex dynamics*. 1992: Cambridge university press.

63. Samimy, M., et al., *Active control of high-speed and high-Reynolds-number jets using plasma actuators.* Journal of Fluid Mechanics, 2007. **578**: p. 305-330.

64. Samimy, M., et al., *Acoustic and flow fields of an excited high Reynolds number axisymmetric supersonic jet.* Journal of Fluid Mechanics, 2010. **656**: p. 507-529.

65. Schlichting, H., K. Gersten, and K. Gersten, *Boundary-layer theory*. 2000: Springer Science & Business Media.

66. Stuart, J., *On the non-linear mechanics of hydrodynamic stability.* Journal of Fluid Mechanics, 1958. **4**(01): p. 1-21.

67. Sunderland, P.B., et al., *Lengths of laminar jet diffusion flames under elevated gravity.* Combustion and Flame, 2008. **152**(1): p. 60-68.

68. Suzuki, T. and T. Colonius, *Instability waves in a subsonic round jet detected using a near-field phased microphone array.* Journal of Fluid Mechanics, 2006. **565**: p. 197-226.

69. Williams, F.A., *Combustion Theory* 2ed. 1985: The Benjamin/Cummings.

70. Williams, F.A., *Urban and Wildland Fire Phenomenology.* Progress in Energy and Combustion Science, 1982. **8**(4): p. 317-354.

71. Xiao, H., M.J. Gollner, and E.S. Oran, *From fire whirls to blue whirls and combustion with reduced pollution.* Proceedings of the National Academy of Sciences, 2016. **113**(34): p. 9457-9462.

72. Yetter, R.A., I. Glassman, and H.C. Gabler, *Asymmetric whirl combustion: a new low NO x approach.* Proceedings of the combustion institute, 2000. **28**(1): p. 1265-1272.

73. Yih, C.-S., *Dynamics of nonhomogeneous fluids*. Vol. 306. 1965: Macmillan New York.

74. Yu, D. and P. Zhang, *On flame height of circulation-controlled firewhirls with variable physical properties and in power-law vortices: A mass-diffusivity-ratio model correction.* Combustion and Flame, 2017. **182**: p. 36-47.

75. Yu, D. and P. Zhang, *On the flame heigth of circulation-controlled firewhirls with variable density.* Proceedings of the Combustion Institute, 2017. **36** p. 3097-3104.

76. Yu, K.H. and K.C. Schadow, *Role of large coherent structures in turbulent compressible mixing.* Experimental Thermal and Fluid Science, 1997. **14**(1): p. 75-84.

77. Zaman, K.B.M.Q., *Asymptotic spreading rate of initially compressible jets - experiment and analysis.* Physics of Fluids, 1998. **10**(10): p. 2652-2660.

78. Zaman, K.B.M.Q., *Spreading characteristics of compressible jets from nozzles of various geometries.* Journal of Fluid Mechanics, 1999. **383**: p. 197-228.

79. Zhou, R. and Z.N. Wu, *Fire whirls due to surrounding flame sources and the influence of the rotation speed on the flame height.* Journal of Fluid Mechanics, 2007. **583**: p. 313-345.